Dissertation

submitted to the
Combined Faculties for the Natural Sciences and for Mathematics
of the Ruperto-Carola University of Heidelberg, Germany
for the degree of
Doctor of Natural Sciences

presented by
Dipl.-Phys. Martina Schürmann
born in Herford, Germany

Oral examination: October 31st, 2007

Digital In-Line Holographic Microscopy with Various Wavelengths and Point Sources Applied to Static and Fluidic Specimens

This dissertation was carried out at the
Institute of Physical Chemistry

Referees
Priv. Doz. Dr. Michael Himmelhaus

and

Prof. Dr. Dr. Christoph Cremer
Kirchhoff-Institute of Physics

Zusammenfassung: Holographie ist eine linsenfreie dreidimensionale Darstellungstechnik, die bei Verwendung von sphärischen Wellen die Erstellung vergrößerter Abbildungen ermöglicht. Da die Methode im Gegensatz zur herkömmlichen Mikroskopie linsenfrei arbeitet, hängt die erreichbare Auflösung allein von der Wellenlänge des verwendeten Lichtes und dem räumlichen Detektionswinkel ab. Somit ist die Verwendung kurzer Wellenlängen von Vorteil. In dieser Arbeit konnten Polystyrolkugeln der Größen 5.9, 2.9, 0.752, 0.500 und 0.356 µm hochaufgelöst abgebildet werden. Des Weiteren wurden Fibroblasten von etwa 100 µm Ausdehnung und Lithographiestrukturen in verschiedenen Formen und Größen aufgenommen. Durch den Einsatz einer Ölkammer mit einem höheren Brechungsindex wurde eine signifikante Steigerung der numerischen Apertur und damit der erreichbaren Auflösung erzielt. Es konnte gezeigt werden, dass mittels gepulster UV- und Synchrotron-VUV-Strahlung digitale In-line Holographie in Submikrometerauflösung möglich ist. Erste Experimente zur Erweiterung der Methode in die vierte Dimension beinhalteten die Verfolgung von Tracerpartikeln wie Mikrokugeln und Öltropfen in Flusskanälen. Neben der Verwendung von Lochblenden wurde auch die Eignung von Lichtleiterspitzen als Punktquellen untersucht. Derartige Punktquellen können aufgrund ihrer hohen Flexibilität auch in komplizierten Aufbauten eingesetzt werden und sind für biologische Fragestellungen durch ihre in situ-Tauglichkeit besonders interessant.

Abstract: Holography is a lensless imaging technique with intrinsic three-dimensional properties. Employing spherical waves enables the acquisition of magnified images. As the method in contrast to conventional microscopy does not require lenses, the achievable resolution only depends on the illumination wavelength and the solid detection angle. Approaching short wavelengths is thus advisable. In this thesis, 5.9, 2.9, 0.752, 0.500 and 0.356 µm polystyrene beads could be resolved. Furthermore, fibroblast cells with a diameter of about 100 µm and lithographic structures with random forms and shapes were imaged. By introducing an oil chamber with a higher refractive index into the setup, a significant increase of the numerical aperture and thus the achievable resolution was obtained. Nanosecond UV and synchrotron picosecond VUV radiation were proven to provide coherent illumination for in-line holographic microscopy measurements, enabling submicron resolution. First experiments in extending the method towards the fourth dimension included the tracking of tracer particles such as microspheres and oil droplets in flow channels. In addition to the commonly used pinholes, optical fibers were tested with respect to their suitability as alternative point sources. Due to their flexibility these sources could be used in complicated measurement geometries. Furthermore, their ability to be applied in situ makes them interesting for biological studies.

Contents

Introduction

... dass ich erkenne, was die Welt im Innersten zusammenhält.

Faust. Der Tragödie erster Teil
Johann Wolfgang von Goethe

Gaining insight into the nature of things is one of mankind's oldest dreams. The conservation of that insight in order to share the knowledge and pass it on, another.

A conventional picture presents objects quite imperfectly. Projected on a screen it displays a two-dimensional image of a three-dimensional world that is only interpretable by experience. Images derived from holograms, by contrast, can be truly three-dimensional and thus theoretically exact replica of the original. After Greek etymology, the term holography means complete recording. This refers to the special property of holography that distinguishes it from photography: the recording of the amplitude as well as the phase of the light waves scattered by an object and the resulting ability to image that object three-dimensionally.

Holography in principle is possible with both plane and spherical waves. When using spherical illumination the radial propagation of the wavefront induces a magnifying effect that enables the technique to be used as a microscopic method. Unlike conventional microscopy, holography is a lensless technique. Thus, the achievable resolution is only limited by the wavelength of the illumination and the detection angle. Employing short wavelengths therefore enables high-resolution imaging of small objects.

Information on the structure of matter encompasses length scales ranging

1

from millimeter to atomic dimensions. The submicron regime is especially interesting as it is the domain on which the quantum nature of matter becomes relevant. In biology, it is the regime of the principal constituents of life, such as nucleic acids, proteins and lipids. Protein structure determination for example is one of the most challenging areas of research today. In order to access these length scales, short wavelengths have to be applied for illumination. Due to its large penetration depth and high phase contrast induced by biological objects, photon-based holography seems to be an ideal probe to obtain information on the structure of biomatter. A reduction of the wavelength into the UV, VUV or soft X-ray range and especially in the water window between 2 and 5 nm as frequently used in X-ray microscopy of biological specimens promises high-resolution holographic images. Especially in the light of future implementation of free-electron X-ray lasers (XFELs) providing high spatial coherence and photon flux, obtaining three-dimensional images of the structure of matter in the nanometer regime is one of the most compelling aspects of the method.

For X-rays, the optical density of matter is close to that of air or vacuum. Thus, few devices can be used for their manipulation. A setup free of mirrors or lenses to guide and redirect the beam is therefore desirable. Holography in an in-line geometry as originally proposed by Dennis Gabor to overcome the limitations introduced by spherical abberation of lenses only requires a coherent source, a pinhole to create spherical waves, a sample and a detector. The further development of this promising technique in terms of resolution enhancement and employment of shorter wavelengths was the objective of this dissertation along with a full exploitation of the method's advantages in view of applications in biology, soft matter and life sciences. The results presented in this work can be roughly divided into three sections: The first part describes the achievements obtained with short wavelengths and pinhole point sources applied to static samples along with an implementation of pulsed UV and VUV nano- and picosecond radiation. An application of in-line holography to fluidic studies in order to exploit the method's intrinsic three-dimensionality forms the second part of the thesis. The third part consists of the probing of optical fiber ends as suitable sources of divergent

illumination alternatively to the commonly used pinholes.

As general introduction to holography, Chapter 1 describes the basics of holography along with a short overview of the theoretical background including the relevant aspects of diffraction theory. Several applications of holography are also presented and an overview of the state of art of the method is given. Furthermore, a comparison between conventional and holographic microscopy is drawn. Chapter 2 describes the materials and methods used in this theses, i.e. the fabrication of pinholes used to derive spherical waves as well as the preparation of the observed samples. Optical fiber ends used as alternative sources for divergent wavefronts were either cleaved or, in order to improve the degree of divergence, mechanically drawn which is also explained in Chapter 2. From Chapter 3 on, the results obtained in this thesis are presented. Spherical wavefronts of visible light were used for digital in-line holography. An increase of resolution was pursued by decreasing the wavelength and increasing of the numerical aperture. Different samples were tested with respect to their imaging and resolution properties. Polystyrene beads on glass substrates were imaged in distributions that varied from single scatterers to extended clusters. Thin lithographic structures were designed and imaged for resolution testing. As a first step towards biophysical problems, fibroblast cells served as biological samples. An additional increase of resolution by increasing the numerical aperture was achieved through the inclusion of an oil chamber in the setup. Nanosecond UV radiation was used for digital in-line holographic microscopy in order to probe the applicability of pulsed illumination with respect to the planned measurements with picosecond VUV radiation or, as a future vision, to those with the femtosecond pulses of the XFEL. First experiments attempted with synchrotron radiation at BESSY II are presented in Chapter 4. The general applicability of those short wavelengths for pinhole-source digital in-line holography was tested and could be shown. Especially with respect to applications in biology, the possibility to extend the method into the fourth dimension was probed. Apart from the high resolution capacity of the technique, the possibility to obtain three-dimensional images is an extremely important property. Tracking experiments with tracer particles such as polystyrene beads or oil droplets

in fluidic channels were done with visible light which are described in Chapter 5. The obtained data was displayed in a four-dimensional representation and the traces analyzed. Furthermore, as an alternative to the otherwise used pinholes, optical fibers were implemented to guide the wave and illuminate the sample divergently which is presented in Chapter 6. These highly flexible light sources are especially interesting for biological problems as they can be placed inside solution, thus enabling very short recording distances and therefore the acquisition of highly magnified images. Additionally, a comparison between images obtained with optical fiber and pinhole sources is given.

Chapter 1

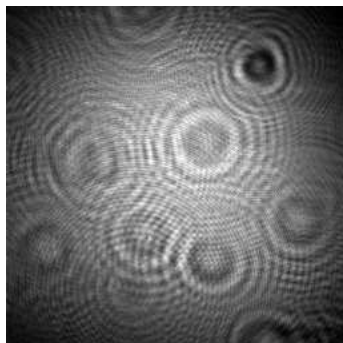# Theoretical Background

1.1 Basics of Holography

Figure 1.1: Concentric interference fringes

Holography in contrast to photography is a method to record objects three-dimensionally. The wavefront scattered by any illuminated object contains both amplitude and phase information. Conventional recording materials, however, only respond to intensity, requiring all phase information to be converted into variations of intensity. Holography does this by introducing the so-called reference wave, originating from the same source as the scattered wavefront or object wave. When using coherent illumination, both waves form an interference pattern at the detector screen, the hologram. In the case of illumination with a spherical wavefront it consists of concentric fringes centered on one axis through the object and normal to the propagation direction of the illuminating wavefront (Figure 1.1). The intensity at each point of this pattern now also depends on the phase of the object wave and thus the hologram contains information on both its phase and amplitude. If the hologram is

illuminated with the reference wave again, the original object wave is re-
constructed. A three-dimensional image is created that contains perspective
and focus depth of the original. Unlike conventional microscopy, holography
does not use lenses. The achievable resolution thus depends solely on the
wavelength of the used illumination and the angle of detection.

In 1948 the British-Hungarian physicist Dennis Gabor proposed a theory
to overcome the spherical abberation of electron lenses and thus the lim-
ited resolving power of electron microscopes [1]. His idea was to employ a
lensless setup and use it to record the image of an object in its complete
three-dimensional structure.   In the practical implementation, an arrange-
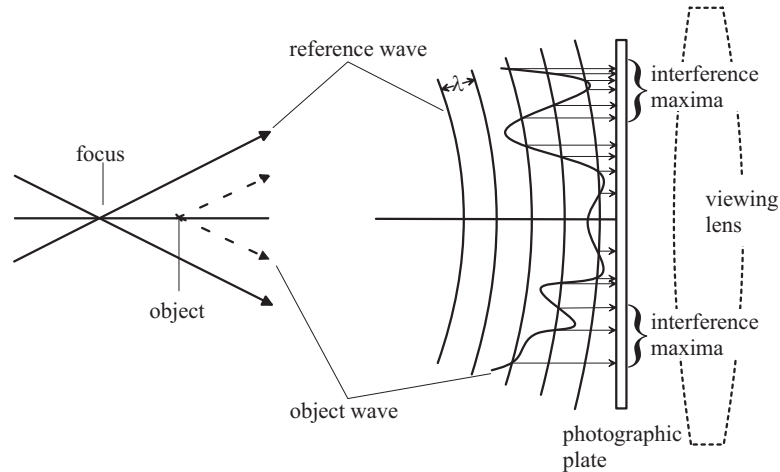
Figure 1.2: Schematic drawing of the interference between object and
reference waves

ment of opaque lines on a transparent background was illuminated with a
beam of monochromatic light as depicted in Figure 1.2. The interference
pattern formed by the directly transmitted beam and the beam scattered by
the lines was recorded on a photographic plate. Gabor then made a positive
transparent out of this negative and called it hologram. He illuminated it
with light of the same wavelength as before [2] and obtained two diffracted
waves: one reconstructing a virtual, undistorted image in the object's former
position and another one with the same amplitude but the opposite phase,
producing a real image. The object field of view corresponds to the virtual
image field of view, so the virtual image corresponds to the true image while

the real image is often called conjugated [3] or twin image [2].

By use of this method a complete three-dimensional image of the object can be produced. It exhibits all effects of perspective and depth of focus and is - if recorded and reconstructed with the same reference wavefront - apart from the missing color information indistinguishable from the original [4].

With the development of the laser in the 1960s which supplied next to a high, uniform and stable intensity the necessary coherence in space and time the importance of holography increased greatly [2]. Narrow, low divergence beams with a well-defined wavelength enabled for the first time stable interference patterns between reference and object wave. Gabor was awarded with the Nobel Prize in physics in 1971 for his development.

1.2   Principles of In-Line Holography

As all elements of the technique introduced by Gabor are positioned along an optical axis perpendicular to the photographic plate and also to distinguish it from other, later developed methods, for example like off-axis or Fourier holography, it is called in-line holography. In this simplest realization of the holographic method, plane as well as spherical waves can be used for illumination. However, using spherical waves to record and reconstruct holograms is the more general case as plane waves can be treated as spherical waves whose origins lie at infinite distances from the observer. All results of this thesis have been achieved by implementation of a setup based on the in-line principle with spherical waves (see Section 3.1). The radial propagation of spherical waves induces a magnifying effect, enabling holography to be used as a microscopy technique. The extension of the hologram greatly influences the achievable resolution which is thus no longer limited by the granularity of a photographic material or the pixel size of a digital detector. The hologram itself does not carry the image of the object but a permanent signature in the form of an interference pattern. Mathematically, a hologram can be regarded as a diffraction grating with a highly complex transmission profile and thus can be treated within the theory of diffraction [5].
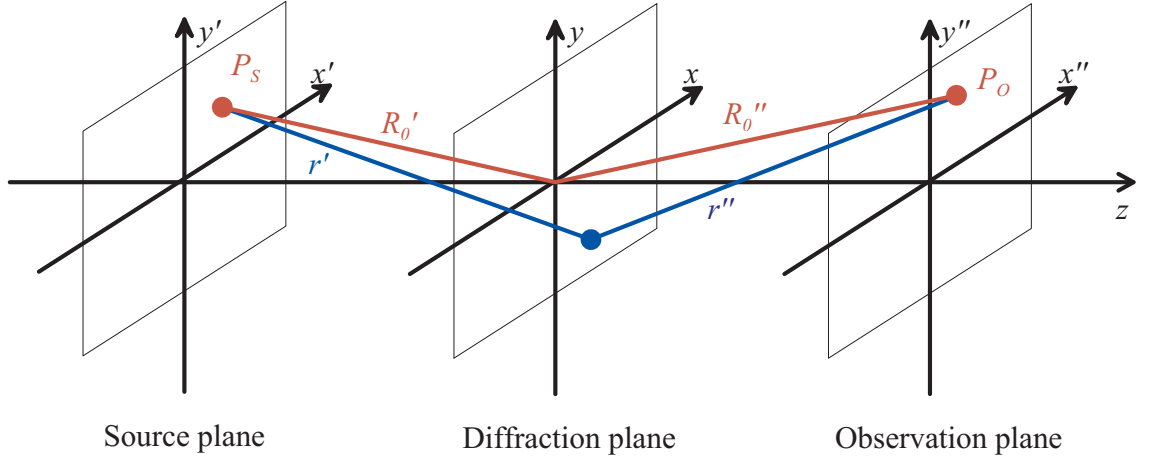
1.2.1   Kirchhoff's Diffraction Theory

Figure 1.3: Coordinate systems to visualize diffraction

Diffraction is the phenomenon of light bending across edges which occurs when the dimensions of the obstacle are in the range of the wavelength of the light. Qualitatively it can be explained by Huygen's principle that states that every point of a wavefront can be considered as a source point for secondary wavefronts. Thus, a diffracting object placed between a light source and a detector becomes itself a source radiating in all directions. The diffracted light field satisfies the homogeneous scalar wave equation [5]

$$\nabla^2 E(\mathbf{r}, t) - \frac{1}{v^2} \frac{\partial^2}{\partial t^2} E(\mathbf{r}, t) \;=\; 0. \tag{1.1}$$

Kirchhoff could show that the light field at any point P_O could be calculated if the scalar field was known at every point on an arbitrarily chosen closed surface S enclosing P_O but excluding the source [5]. For practical calculations he considered a diffracting aperture of infinite size which is opaque except for a portion Σ. Kirchhoff chose to solve the scalar wave equation (Equation 1.1), thus ignoring polarization effects in diffraction. Although boundary conditions at an edge of the aperture are different for light waves polarized parallel and perpendicular to the plane of the edge, the solution of the scalar wave equation can describe light diffraction adequately in most

practical cases [5]. For a quasi-monochromatic optical field

$$E(\mathbf{r}, t) \;=\; E(\mathbf{r}) \exp(-i\omega t) \tag{1.2}$$

of mean frequency ω, insertion of the complex amplitude $E(\mathbf{r})$ into Equation 1.1 leads to the Helmholtz equation

$$(\nabla^2 + k^2)E(\mathbf{r}) = 0 \tag{1.3}$$

with $k = \omega/c$. Let $E_{in} = a_0 \exp(ikr')/r'$ be the scalar field incident at the diffracting aperture, r' being the position of a point in the diffraction plane with respect to the point source P_S (Figure 1.3) and a_0 the real amplitude of the spherical wave at unit distance from the source. The field $E(P_O)$ observed at a point P_O in the observation plane is given by the Fresnel-Kirchhoff diffraction formula [5]

$$E(P_O) \;=\; \frac{ia_0}{\lambda} Q \iint_\Sigma \frac{\exp(-ik(r' + r''))}{r'r''} \, dS \tag{1.4}$$

where r'' is the position of a point in the diffraction plane with respect to P_0. The factor Q is the so-called obliquity factor that controls the extent of diffraction in different directions. In particular it prohibits backwards wave propagation. Under usual diffraction conditions where the integration is performed over the complete aperture S which is different from zero only for the small portion Σ the changes in r' and r'' do not significantly change the amplitude factor $1/r'r''$ which then may be replaced by the constant factor $1/R_0'R_0''$ (see Figure 1.3).   Figure 1.4 shows the geometry of the diffraction process. The position coordinates of the points $P_S(x', y', z')$ and $P_O(x'', y'', z'')$ are related to the origin of the diffraction plane via the direction
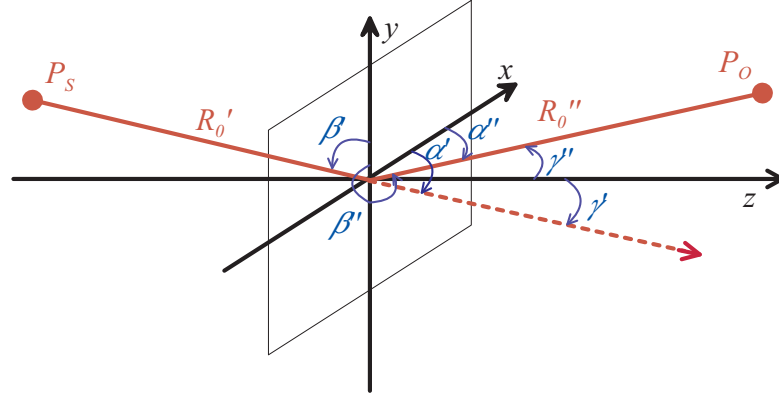
Diffraction plane

Figure 1.4: Diffraction geometry

cosines

$$
\begin{aligned}
l' &= \cos\alpha' = -x'/R_0' \\
m' &= \cos\beta' = -y'/R_0' \\
n' &= \cos\gamma' \\
l'' &= \cos\alpha'' = x''/R_0'' \\
m'' &= \cos\beta'' = y''/R_0'' \\
n'' &= \cos\gamma''
\end{aligned}
$$

between the directions of propagation of the incident and diffracted waves. The Fresnel-Kirchhoff diffraction formula then takes the form [5]

$$
E(P_O) = \frac{ia_0}{\lambda}Q\frac{\exp(ik(R_0' + R_0''))}{R_0' + R_0''} \iint\limits_{\Sigma} t(x,y)\exp(-ik\xi(x,y))\ dxdy \quad (1.5)
$$

where

$$
\xi(x,y) = x(l' - l'') + y(m' - m'') + \frac{1}{2}(x^2 + y^2)\left(\frac{1}{R_0'} + \frac{1}{R_0''}\right)
$$
$$
- \frac{1}{2R_0'}(xl' + ym')^2 - \frac{1}{2R_0''}(xl'' + ym'')^2
$$

and $t(x, y)$ is the transmission function of the aperture.

1.2.2   Diffraction Theory of Image Formation

Except for the nonlinear summands in the phase factor, Equation 1.5 has the form of a two-dimensional Fourier transform of a function $f(x, y)$

$$F(u, v) \; = \; \iint\limits_{-\infty}^{\infty} f(x, y) \exp(-i2\pi(ux + vy)) \; dxdy \qquad (1.6)$$

with the spatial frequencies u and v. Fourier transforms are extensively used in optics as they allow the expression of a nonperiodic function in terms of an integral [5]. Among their important and useful properties are [5]

1. Scaling property: Compression in the spatial coordinate domain results in an expansion in the spatial frequency domain and vice versa. A Fraunhofer diffraction pattern broadens if the size of the diffracting aperture is reduced.

2. Shifting property: A spatial translation of a function produces a phase shift in its Fourier transform. A translation of the diffracting aperture in the transverse plane does not change the intensity distribution in Fraunhofer diffraction.

3. Linearity property: Fourier transforms of complementary functions are identical except for a change in sign.

4. Parseval's theorem: This is a statement of energy conservation. In Fraunhofer diffraction, Parseval's theorem ensures the equality of the energy contents of the field distributions over the object and diffraction planes.

5. Solvability: Most absolutely integrable functions have a large variety of well-known analytical solutions. Furthermore, efficient algorithms, e.g. Fast Fourier Transform (FFT) Techniques exist to compute digital signal processing.

In order to make use of these properties one has to get rid of the phase introduced by the quadratic terms in the diffraction integral (Equation 1.5) which is done by entering the Fraunhofer diffraction region [5]

$$\frac{a^2}{R_0} \ll \lambda \tag{1.7}$$

where a defines the maximum values of the x- and y-coordinates of a point in the diffraction plane, i.e. the extent of the scattering aperture. R_0 is the smaller of the R_0' and R_0'' distances. Practically, this means that source and observation points have to be sufficiently far away from a small diffracting aperture. Under these condition, Equation 1.5 reduces to

$$
\begin{aligned}
E(P_O) \quad & = \quad -\frac{ia_0}{\lambda} Q \frac{\exp(ik(R_0' + R_0''))}{R_0' + R_0''} \quad \times \\
& \times \quad \int\!\!\!\int\limits_{-\infty}^{\infty} t(x,y) \exp(-ik(x(l'' - l') + y(m'' - m)))\ dxdy \\
& = \quad -\frac{iA_0}{\lambda} \int\!\!\!\int\limits_{-\infty}^{\infty} t(x,y) \exp(-i2\pi(ux + vy))\ dxdy, \tag{1.8}
\end{aligned}
$$

where

$$A_0 = a_0 Q \frac{\exp(ik(R_0' + R_0''))}{R_0' + R_0''}.$$

$$u \quad = \quad \frac{l'' - l'}{\lambda} = \frac{1}{\lambda}\left(\frac{x'}{R_0'} + \frac{x''}{R_0''}\right)$$

and

$$v \quad = \quad \frac{m'' - m'}{\lambda} = \frac{1}{\lambda}\left(\frac{y'}{R_0'} + \frac{y''}{R_0''}\right)$$

are the spatial frequencies which determine the positions of the points P_S and P_O with respect to the diffracting aperture. The diffraction integral (Equation 1.8) is now exactly in the form of the Fourier transform integral (Equa-

tion 1.6), thus it is possible to express the field distribution in Fraunhofer diffraction in terms of the Fourier transform of the aperture transmission function $t(x, y)$ [5]:

$$E(u, v) = -\frac{iA_0}{\lambda}F(u, v) \tag{1.9}$$

where

$$F(u, v) = \iint\limits_{-\infty}^{\infty} t(x, y)\exp(i2\pi(ux + vy))\ dxdy.$$
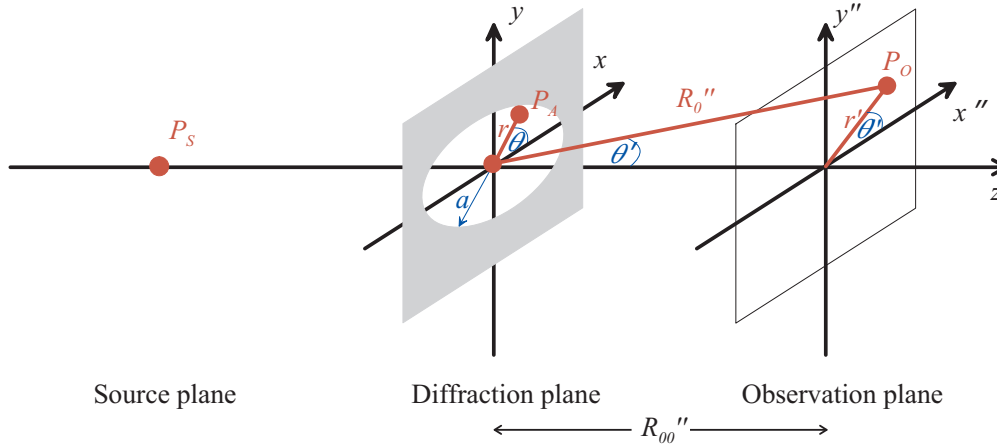
1.2.3 Spherical Wave Generation

Figure 1.5: Schematic drawing of Fraunhofer diffraction from a circular aperture

In order to be able to use holography as a microscopy method, the radial propagation of spherical waves is exploited that induces a magnifying effect. There are several ways to change the plane wavefront supplied by the laser into a divergent one, e.g. through lenses or apertures. The most advantageous way for in-line holography is by introducing a pinhole with a diameter of the order of the illuminating wavelength into the beam path. The pinhole is mounted at a distance from the detector that satisfies the Fraunhofer criterion (Equation 1.7). Diffraction from a circular aperture can be derived

from Equation 1.8 if one introduces polar coordinates (Figure 1.5) [5]

$$u = \frac{x''}{\lambda R_0''} = \rho \, \cos\theta''$$

and

$$v = \frac{y''}{\lambda R_0''} = \rho \, \sin\theta''$$

where

$$\rho = \frac{r''}{\lambda R_0''}.$$

The amplitude transmission function of the circular aperture with radius a is then

$$t(r,\theta) = \begin{cases} 1 & \text{for } r \leq a \\ 0 & \text{for } r > a. \end{cases}$$

Its Fourier transform can be expressed as

$$
\begin{aligned}
F(\rho,\theta'') &= \int_0^\infty \int_0^{2\pi} t(r,\theta) \exp(-i2\pi(ur\cos\theta + vr\sin\theta))r \; drd\theta \\
&= \int_0^a r \left(\int_0^{2\pi} \exp(-i2\pi\rho r \cos(\theta - \theta''))d\theta \right) dr.
\end{aligned}
$$

Due to rotation symmetry F cannot depend on θ'' and thus θ'' can be set to 0, yielding

$$F(\rho) = \int_0^a r \left(\int_0^{2\pi} \exp(-i2\pi\rho r \cos\theta)d\theta \right) dr. \qquad (1.10)$$

The inner integral is a Bessel function which is defined as

$$J_n(x) = \frac{i^{-n}}{2\pi} \int\limits_0^{2\pi} \exp(i(n\phi + x\cos\phi))d\phi. \tag{1.11}$$

Thus, one can write

$$F(\rho) = 2\pi \int\limits_0^a r J_0(2\pi\rho r)dr$$

$$= \frac{1}{2\pi\rho^2} \int\limits_0^{2\pi\rho a} (2\pi\rho a) J_0(2\pi\rho a)d(2\pi\rho a). \tag{1.12}$$

Using the recursion relation

$$x' J_1(x') = \int\limits_0^{x'} x J_0(x)dx \tag{1.13}$$

and

$$\lim_{2\pi\rho a \to 0} \frac{J_1(2\pi\rho a)}{2\pi\rho a} = \frac{1}{2}$$

one can finally derive the intensity of the Fraunhofer diffraction pattern from a circular aperture [3]

$$I(\rho) = \frac{|A_0|^2}{\lambda^2}|F(u,v)|^2 = I_0 \left(\frac{R''_{00}}{R''_0}\right)^2 \left[\frac{2\ J_1(2\pi\rho a)}{2\pi\rho a}\right]^2$$

where I_0 is the maximum intensity on the detector ($\rho = 0$). Rewritten for the angle θ' between the diffracted ray and the z-axis with $\sin\theta' = r'/R''_0$ and thus $\rho = \sin\theta'/\lambda$ we have

$$I(\theta') = I_0 \left(\frac{R''_{00}}{R''_0}\right)^2 \left[\frac{2\ J_1(2\pi\frac{a}{\lambda}\sin\theta')}{2\pi\frac{a}{\lambda}\sin\theta'}\right]^2. \tag{1.14}$$

The first root of $J_1(2\pi\frac{a}{\lambda}\sin\theta')$ is at 1.220π. With a wavelength $\lambda = 405$ nm

and a distance $L = 11$ mm one can derive the theoretical intensity distributions shown on the left-hand side of Figure 1.6 for varying pinhole diameters $A = 2a$. Due to the axial symmetry this distribution is rotation-symmetric
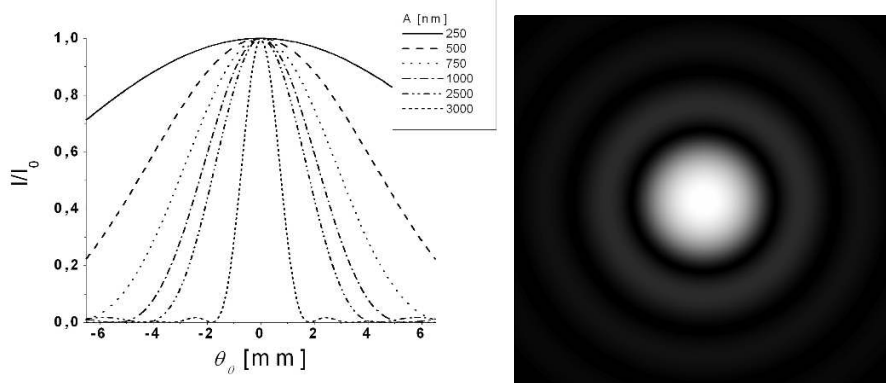
Intensity distribution for various pinhole diameters and for $\lambda = 405$ nm, $L = 11$ mm

Computer-generated image of an Airy pattern [6]

Figure 1.6: Angular intensity distribution for various pinhole diameters (left) and lateral intensity distribution in the detector plane (right)

to the intensity axis. The bright region in the center is known as the Airy disc (see Figure 1.6, right). It is surrounded by a number of concentric alternating bright and dark rings, the Airy pattern. The dark rings are the roots of the function J_1. The angular radius θ_0 of the first dark ring is given by [3]

$$\sin \theta_0 = 1.22 \frac{\lambda}{A}.$$

For small values λ/a the half-angular width of the Airy disc is then

$$\theta_0 \;=\; 1.22 \frac{\lambda}{2a} \tag{1.15}$$

and the linear diameter of the Airy disk has the value

$$D_A \;=\; 1.22 \frac{\lambda}{a} R_0''. \tag{1.16}$$

The diameter of the Airy disc is thus inversely proportional to the aperture

diameter. If A approaches the wavelength λ, the Airy disc increases, and the aperture more and more resembles a pinhole that emits truly spherical waves.

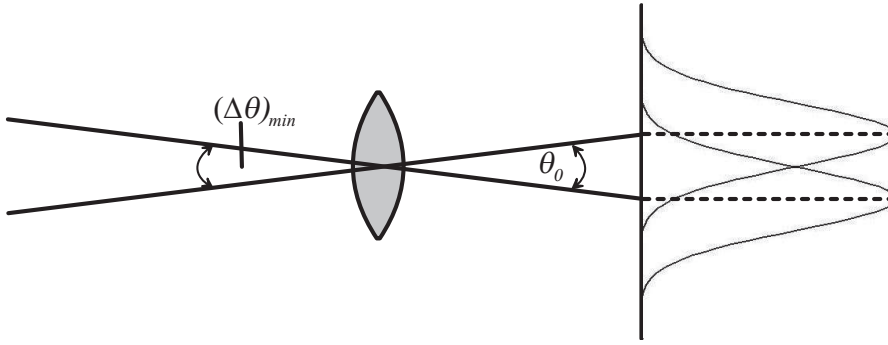## 1.2.4 Resolving Power of Image-Forming Systems

Figure 1.7: Schematic drawing of the resolving power of an optical device

The resolving power of an image-forming system is its ability to resolve images of close lying objects [5]. In analogy to diffraction from a circular aperture as described above, the circular aperture of an optical system produces for each point of the object an Airy pattern in the image plane. The criterion for two incoherently illuminated point objects to be resolved is that their Airy discs do not overlap. As derived above (see Equation 1.16), the angular radius of the Airy disc for small angles is

$$\theta_0 \quad \approx \quad \sin \theta_0 \quad = \quad 1.22 \frac{\lambda}{A}$$

where A is the diameter of the aperture. An optical device can resolve two points if their angular separation $\Delta\theta$ is larger than the angular radius of the Airy disc of either one of the objects (Figure 1.7):

$$\Delta\theta \geq \theta_0.$$

The minimum angular separation of the objects that can be resolved is then

$$(\Delta\theta)_{min} \;=\; \theta_0 \;=\; 1.22\frac{\lambda}{d} \tag{1.17}$$

where $d \;=\; 2a$ is the diameter of the objective of the optical device. The Abbe sine condition is [5]

$$n_0 y_0 \sin\alpha_0 \;=\; ny\sin\alpha \tag{1.18}$$

where y is the separation of the point objects in the image plane and y_0 their distance in the object plane. n and n_0 are the refractive indices in the object and image spaces, respectively. Combined, these two equations yield the linear resolution limit of a microscope with incoherent radiation

$$(y_0)_{min} \;=\; \frac{0.61\;\lambda}{n_0\;\sin\alpha_0} \;=\; \frac{0.61\;\lambda}{NA}. \tag{1.19}$$

The product $n\sin\alpha$ is known in optics as the numerical aperture (NA), a dimensionless number that characterizes the range of angles over which the system can accept or emit light. Thus, Equation 1.19, also known as the Abbe resolution limit, states that exact spacing can be resolved when the numerical aperture of the objective lens is large enough to capture the first-order diffraction pattern produced in a diffraction-limited microscope at a specific wavelength [7]. For coherent illumination the limit of resolution increases a little as the intensity distribution in the image plane depends on the phase difference between the fields originating from the two points in addition to their separation due to their spatial coherence [5]. If one considers an infinite square grating of grating element a at least the $m \;=\; 0$ and $m \;=\; \pm 1$ diffraction orders of the grating must reach the image plane which results in the distance

$$(a)_{min} \;=\; \frac{\lambda}{\sin\alpha_0}$$

between two points that can be resolved. Due to periodicity it is sufficient to only consider the $m \;=\; 0$ and $m \;=\; 1$ (or $m \;=\; -1$) diffraction orders,

which results in the least distance

$$(a)_{min} = \frac{\lambda}{2 \sin \alpha_0}.$$

Taking into account the refraction index n_0 of the object space the minimum distance that can be resolved under coherent illumination is [5]

$$(a)_{min} = \frac{\lambda}{2 n_0 \sin \alpha_0} = \frac{\lambda}{2NA}. \tag{1.20}$$

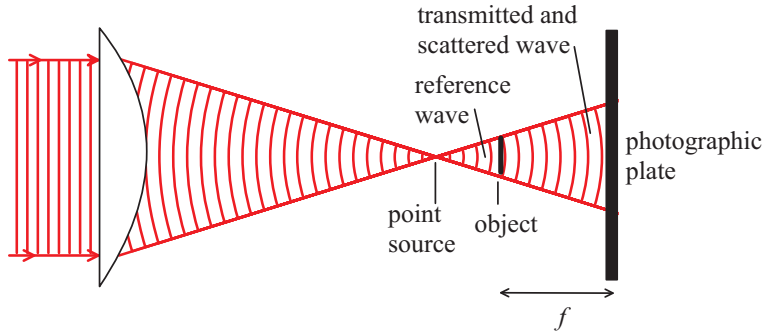## 1.2.5 In-Line Holography with Spherical Waves

Figure 1.8: Schematic drawing of a setup used to record an optical in-line hologram with spherical waves

To record a transmission hologram in an in-line setup the object is illuminated by a beam of monochromatic light brought to a focus (i.e. focused onto a pinhole with a diameter of the order of the wavelength) from which it diverges (Figure 1.8). The object on a transparent mount is positioned relatively close behind the focal point and the photographic plate follows at a larger distance f from the object. The pinhole functions as a point source and emits by approximation a spherical wave with a complex amplitude $\psi_{in}(\theta, \phi, r) = A(\theta, \phi) \exp(ikr)/r$ where A represents the real amplitude of the spherical wave and the exponential factor contains its phase. One part of the spherical wave, ψ_{ref}, passes the sample undisturbed while the other part, ψ_{scat}, hits the sample and is scattered. The scattered object wave interferes with the

stronger undisturbed reference wave, thus creating an interference pattern, the hologram, on the surface of the detector. Unlike in the image plane of a lens, light from the object reaches every point of the detector and thus every portion of the hologram obtains complete information on the amplitude and phase distributions of the object field in the form of the interference pattern. The detector image intensity is then given by

$$I(\mathbf{r}) = |\psi(\mathbf{r})|^2. \tag{1.21}$$

As the wave function ψ at the detector consists of the reference wave ψ_{ref} and the scattered wave ψ_{scat}, it is

$$\psi(\mathbf{r}) = \psi_{ref}(\mathbf{r}) + \psi_{scat}(\mathbf{r}).$$

The intensity then yields [8]

$$
\begin{aligned}
I(\mathbf{r}) &= |\psi_{ref}(\mathbf{r}) + \psi_{scat}(\mathbf{r})|^2 \\
&= |\psi_{ref}(\mathbf{r})|^2 + \psi_{ref}^*(\mathbf{r})\psi_{scat}(\mathbf{r}) + \psi_{ref}(\mathbf{r})\psi_{scat}^*(\mathbf{r}) + |\psi_{scat}(\mathbf{r})|^2 \\
&= \frac{|A(\theta,\phi)|^2}{r^2} + \left[A^*(\theta,\phi)\frac{\exp(-ikr)}{r}\psi_{scat}(\mathbf{r}) \right. \\
&\quad \left. + A(\theta,\phi)\frac{\exp(ikr)}{r}\psi_{scat}^*(\mathbf{r}) \right] + |\psi_{scat}(\mathbf{r})|^2.
\end{aligned}
\tag{1.22}
$$

The right-hand side of Equation 1.22 consists of four terms. The first one, $|\psi_{ref}(\mathbf{r})|^2$, describes the directly transmitted beam. As it contains no information whatsoever about the object, it is not of interest and needs to be suppressed. The following two terms, i.e. the sum in brackets, are the hologram terms as they consist of the superposition of reference wave and scattered (object) wave. The fourth term, $|\psi_{scat}(\mathbf{r})|^2$, is referred to as the self-interference term, containing the interference between the scattered waves. If the object is adequately chosen, this classical diffraction term is very small compared to the other three and thus becomes negligible [8].

The hologram consists of a system of concentric fringes (see Figure 1.1) that act like Fresnel zone plates [9] which focus the passing light by diffraction.

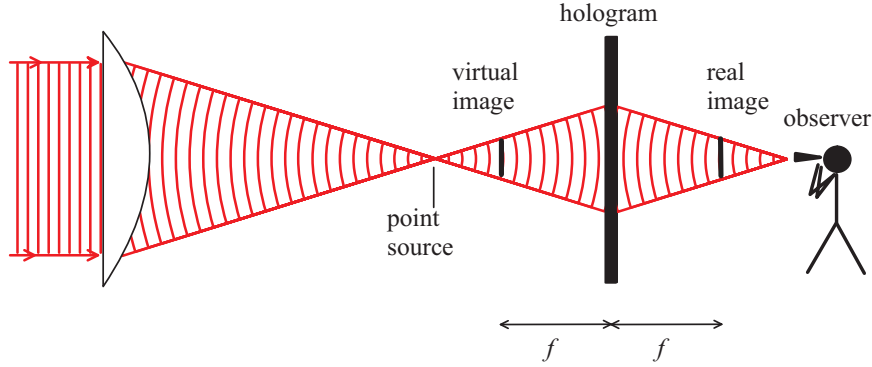Thus, when the object is removed and the hologram is illuminated once again

Figure 1.9: Schematic drawing of a setup used to optically reconstruct an in-line hologram

with the spherical reference wave, the former observation plane now becomes the diffraction plane, and the former diffraction plane becomes the (virtual) object plane: For each point in the hologram two image points are created on opposite sides of the hologram but at equal distances from it. All image points to the right of the hologram are real as they are the converging points of the spherical waves and could be detected directly by a screen at that position. By contrast, the image points to the left of the hologram are virtual as the respective spherical waves only seem to converge there. Thus, the first part of the term in brackets, $\psi_{ref}^*(\mathbf{r})\psi_{scat}(\mathbf{r})$, is except for a constant factor identical to the complex amplitude of the wave scattered by the object and creates a virtual image of the object in its original position [9]. The second part of the term in brackets, $\psi_{ref}(\mathbf{r})\psi_{scat}^*(\mathbf{r})$, also represents the object wave, but with the complementary phase. This wave creates a real image in the converging space between hologram and observer, the twin image. The negative phase results in a depth inverting effect: The point closest to the observer appears the furthest away in the image. Due to the existence of the additional terms next to the hologram term the observer in Figure 1.9 does not only see one image, but a superposition with the out-of-focus twin image and additionally a strong background created by the unscattered light of the direct beam. The reconstructed image's quality is influenced by both [2]. The adequate choice of the object must include a high average transmission

in order to fulfill the condition $|\psi_{scat}(\mathbf{r})| \ll |\psi_{ref}(\mathbf{r})|$, allowing the fourth term of Equation 1.22 to be negligible. Thus fine opaque lines on a transparent background for example are easily reconstructible but an attempt the other way around is very unlikely to be successful [2].

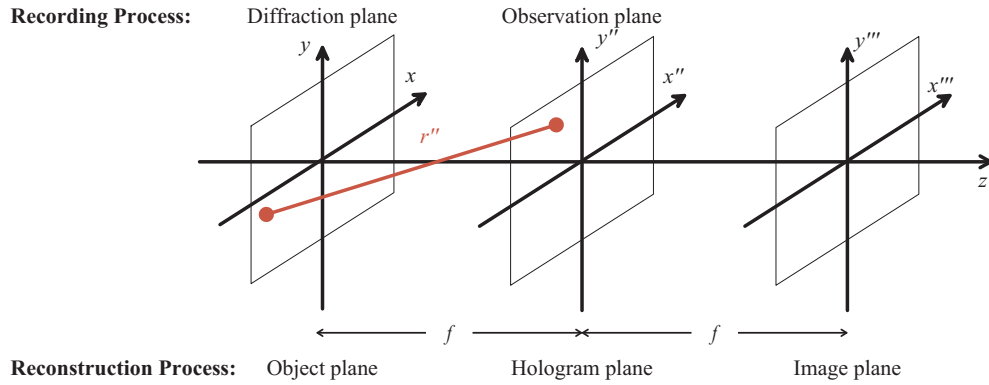Mathematically, the diffraction of a light wave at the hologram can again be

Figure 1.10: Schematic drawing of the coordinate system used for hologram reconstruction

described by the Fresnel-Kirchhoff integral

$$E(x,y) \;=\; \frac{i}{\lambda} \iint h(x,y)\psi_{ref}(x,y)\frac{\exp(-ikr'')}{r''}\; dx''dy'' \qquad (1.23)$$

with

$$r'' \;=\; \sqrt{(x''-x)^2 + (y''-y)^2 + (f)^2}$$

as drawn in Figure 1.10. $E(x,y)$ is the complex amplitude in the object plane, $h(x,y)$ is the hologram transmission function and $\psi_{ref}(\mathbf{r})$ the complex amplitude of the reference wave. r'' is the distance between a point in the hologram plane and a point in the object plane.

1.2.6 Resolution in In-Line Holography with Spherical Waves

The key characteristic of an optical instrument is the magnitude of its resolving power δ. As holography is a lensless technique, the achievable resolution is not limited by the numerical aperture of an objective lens, but by the one of the illuminating wavefront. The numerical aperture in an in-line geometry as used in this thesis is given by [10]

$$NA \;=\; n\,\sin\vartheta \;=\; n\,\frac{D}{2\sqrt{\left(\frac{D}{2}\right)^2 + L^2}}, \tag{1.24}$$

where ϑ is the half-opening angle of the illumination cone emitted by the pinhole, D is the detector width and L the distance between pinhole and detector [10]. For experiments in air $n \approx 1$. As described above in the scaling property of Fourier transforms, the resolution of a hologram depends on its diffraction aperture size. The larger the diameter of the hologram the smaller the details that the hologram can resolve [5]. The theoretical lateral resolution as described in Equation 1.20 is [10]

$$\delta_{lateral}^{theo} \geq \frac{\lambda}{2\,NA}. \tag{1.25}$$

The depth resolution δ_{depth}^{theo} yields [10]

$$\delta_{depth}^{theo} \geq \frac{\lambda}{2\,(NA)^2}. \tag{1.26}$$

Equations 1.24, 1.25 and 1.26 however only qualify for an ideal detector that can resolve the interference fringes resulting from superposition of the reference wave with the waves scattered from the different object points. Thus, increasing the detector size does not necessarily result in an increased resolution. The separation of interference fringes in the plane of the hologram decreases as one moves away from its center. For spherical waves the fringe

spacing d is given by [9]

$$d \;=\; r_{m+1} - r_m \;=\; \left(\sqrt{m+1} - \sqrt{m}\right)\sqrt{2\lambda f} \qquad (1.27)$$

where r_m ($m \in \mathbb{N}$) is the radius of the m-th fringe counted from the center and f the object-detector distance. Instead of the fringe spacing d the fringe pattern can be described by the spatial frequency F which is the reciprocal of d [4]:

$$F \;=\; \frac{1}{d} \;=\; \frac{1}{\left(\sqrt{m+1} - \sqrt{m}\right)\sqrt{2\lambda f}}. \qquad (1.28)$$

The maximum resolvable spatial frequency of the detector is given by the granularity of the photographic material or, in the case of digital recording, the distance Δx of neighboring pixels of the camera [4]

$$F_{max} = \frac{1}{2\Delta x}. \qquad (1.29)$$

Concluding, the quality of a transmission in-line hologram with spherical waves is mostly depending on the following factors:

1. Coherent illumination: The ultimate requirement for holography is sufficient coherence of the illumination as an interference pattern at the detector can only be formed with coherent reference and object waves.

2. Wavelength: As the achievable resolution is strongly dependent on the wavelength of the illuminating light, short wavelengths should be approached.

3. Numerical aperture and maximum spatial frequencies: Both important factors for the achievable resolution are mainly determined by detector characteristics, e.g. size and granularity or, for digital recording means, pixel spacing.

4. Pinhole size: In order to generate a coherent spherical wave, the pinhole diameter must be of the order of the wavelength of the illuminating

light. Using a larger pinhole reduces the spatial coherence on the one hand and narrows the Airy disc of the reference wave on the other hand, thus resulting in a smaller effective numerical aperture as the detector is not fully illuminated. When using laser illumination the latter effect is of greater importance for the image quality than the first one [10].

5. Sample: In order to allow the reference wave to pass undisturbed the sample needs to possess sufficient transparency, i.e. the opaque parts of the sample should occupy a relatively small area compared to the cross section of the incident wavefront. Obeying this requirement at the same time satisfies the Fraunhofer criterion. However, the strict compliance with this criterion limits the extensions of applicable specimens quite drastically, e.g. to $a = 14$ µm for a wavelength of $\lambda = 405$ nm and a typical sample-detector distance of $d_{rec} = 500$ µm. In order to be able to reconstruct images of larger specimens, a method of numerical reconstruction can be applied that will be discussed in Section 1.6. By this method, the nonlinearity in the phase factor in the diffraction integral (see Equation 1.5) is removed via a nonlinear coordinate transformation. This enables the exact evaluation of the diffraction formula [11] and thus allows the imaging of samples with dimensions that exceed the ones allowed by the Fraunhofer criterion.

Additionally, the sensitivity of the recording material is of importance as it determines the necessary exposure time and thus the required period of time for an object to remain immobile. The diffraction efficiency of a hologram, i.e. its ability to diffract the illuminating light appropriately and create a reconstructed image as a true replica of the original is another important material property [2]. Both aspects will be discussed in Section 1.5.

1.3   Off-Axis Holography

The twin image problem was finally solved when E. Leith and J. Upatnieks developed the off-axis technique in the early 1960s [12]. As depicted in Fig-
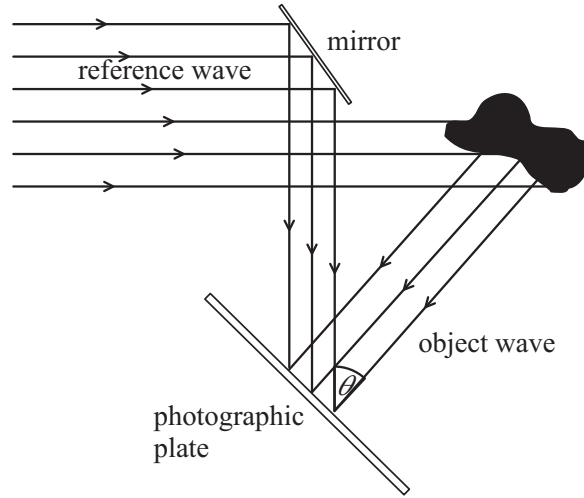
Figure 1.11: Schematic drawing of a setup used to record an off-axis hologram

ure 1.11 they implemented a setup with a relatively large angle θ between reference and object wave. Thus, in the reconstruction the image is spatially separated from the twin image and also from the zeroth-order term created by the undiffracted reference wave preventing the superposition with these undesired disturbances. Although historically in-line holography was developed first, it can be considered as a special case of off-axis holography where $\theta = 0°$. The reference wave is a collimated beam of uniform intensity that is derived from the same source as the illuminating one [2]. It reaches the photographic plate over a mirror. In a reflexion geometry as shown in Figure 1.11 the object wave is scattered off the object without the use of another mirror while in a transmission geometry it is directed over a second mirror onto the photographic plate after passing through the object. For optical reconstruction, the hologram is illuminated with collimated light of the original wavelength. The transmitted beam consists once again of four components [2]: (1) the directly transmitted beam, surrounded by (2) a halo caused by the self-interference of the object wave, (3) the true image and (4) the twin image. The virtual image of the object is produced in its former position. The conjugate real image appears under the same angle θ from the reference beam as the virtual image. Corresponding points on the real
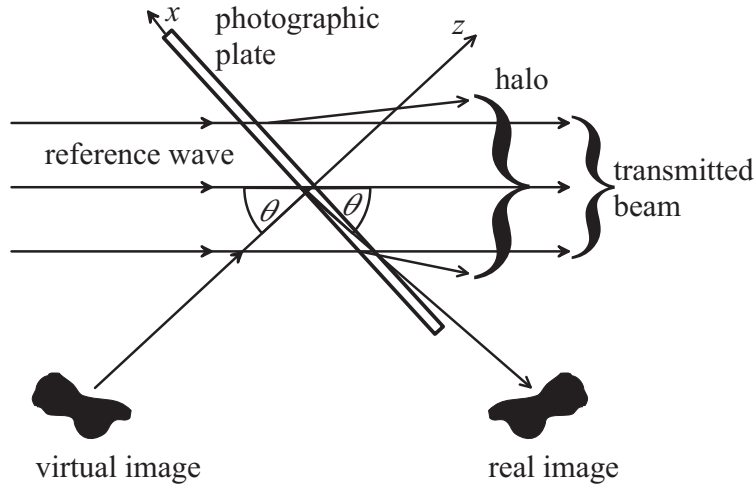
Figure 1.12: Schematic drawing of a setup used to optically reconstruct an off-axis hologram

and virtual images are located at equal distances from the hologram, but on opposite sides of it. If the angle θ between reference and object wave was chosen large enough, the virtual image can be separated spatially from the directly transmitted beam and the twin image.

Various off-axis geometries have been used for holographic imaging [13–15]. Fuhse et al. [16] implemented waveguides in an off-axis setup and used hard X-rays at 10.4 keV photon energy. A commercially available holographic off-axis microscope has been designed by Marquet et al. [17] and is distributed by Lyncée Tec (Switzerland). This holographic microscope uses objectives to focus the beam, thus the resolution is dependent on their numerical aperture. For oil immersion objectives it reaches a lateral resolution of 300 nm [18].

1.4 Fourier Holography

Yet another interesting holographic setup is the Fourier setup as shown in Figure 1.13 that was introduced by A. van der Lugt [19]. In this transmission technique the collimated illumination passes through the object that is located in the front focal plane of a lens. The spherical reference wave emerges from the same plane. Due to the lens Fourier transforms of the original object
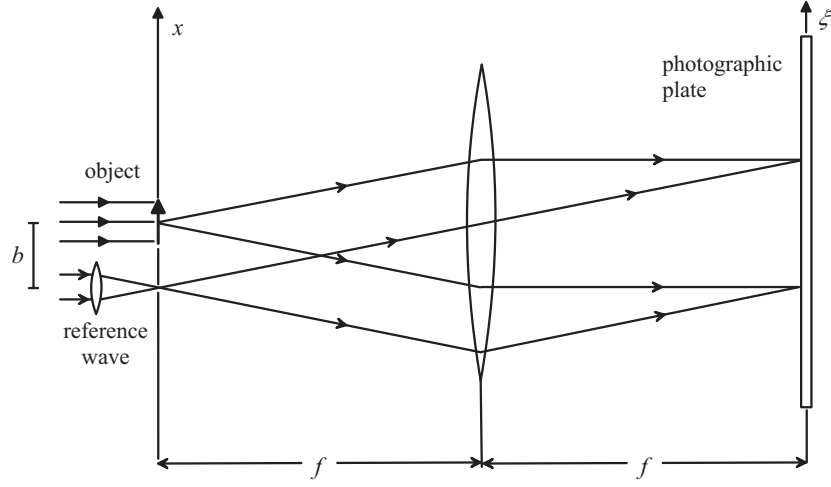
Figure 1.13: Schematic drawing of a setup used to record a Fourier hologram

and reference wavefronts are created. When these transformed waves interfere at the hologram in the back focal plane of the lens the interference fringes have a constant mean frequency instead of one that increases with increasing distance from their center [3]. This lessens the resolution requirements of the photographic medium. For reconstruction as depicted in Figure 1.14 object and point source are replaced by the hologram in the front focal plane of the lens, and a collimated beam of monochromatic light is used for illumination [2]. The lens again Fourier-transforms the transmitted wavefront, and one part of it comes to a focus in the back focal plane of the lens. Again, a halo is formed around this focus. The primary image of the original object is shifted downwards from this focus by a distance b while the conjugate image is shifted upwards by the same distance and rotated by 180° [2]. Another advantage of these holograms is that the reconstructed image does not move upon translation of the hologram within its own plane which is due to the fact that spatially shifting a function only results in a multiplication with a phase factor of its Fourier transform [2]. Recently, Fourier holography has been used to image magnetic nanostructures with soft X-rays [20–23].
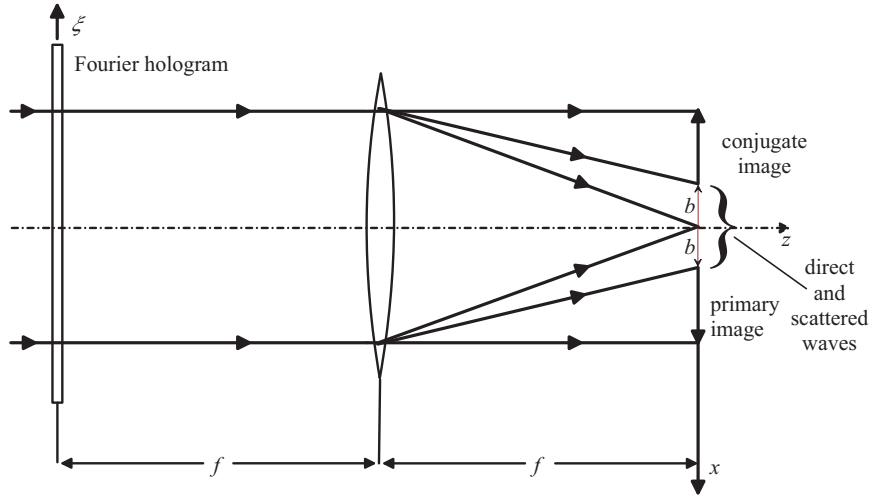
Figure 1.14: Schematic drawing of a setup used to optically reconstruct a Fourier hologram

1.5 Recording Materials

Holograms can be stored as amplitude or phase gratings, depending on the attribute of the recording material that is modulated during the exposure. An amplitude hologram is recorded by changing the absorption properties of the recording material while changing its refractive index or thickness yields a phase hologram. Amplitude holograms have a lower diffraction efficiency η than phase holograms, typically a few percent [9] and are therefore not commonly used. The first materials to record holograms were high-resolution photographic plates and films. Gelatin-embedded silver halide crystals are reduced to black metallic silver in a developing solution if they have been exposed. The unexposed silver halide is removed from the photographic layer in a fixing bath. Thus, the hologram is recorded as an absorbance distribution [9]. Due to the limited diffraction efficiency, however, the reconstructed images are relatively dark. In order to increase this efficiency to about 60% the amplitude grating can be processed into a phase grating by bleaching: In a rehalogenating bleach bath the developed silver is converted back into a transparent silver halide with a high refractive index [2].

A phase hologram with an efficiency of 100% can be recorded on dichromated

gelatin (DCG), where a gelatin layer contains a small amount of a dichromate. A local modulation of the refractive index is obtained by the formation of crosslinks between the carboxylate groups of neighboring gelatin chains. Other commonly used recording materials are photoresists. The areas exposed to light change their solubility and (in the case of a positive resist) are washed away during the developing process. A relief image with a relatively high diffraction efficiency is formed.

The major drawback of the described techniques next to the obviously limited acquisition frequencies of all optical recording materials is the difficult and time-consuming wet chemical developing process along with the fact that the recording materials can not be reused. Photopolymers used to produce phase holograms with excellent diffractive efficiencies are also not reusable, but avoid the wet chemical developing process. Due to photopolymerization the refractive index of the material changes upon exposure. The necessary post-exposure to UV light and baking at high temperatures for 1-2 hrs, however, are not necessarily less demanding process steps.

Reusable recording materials include photothermoplastics (PTP) where a spatially varying electrostatic field is created upon exposure and heating of the substrate erases the hologram again, and photorefractive crystals where electrons are liberated in the exposed areas and become trapped in the adjacent dark areas [2]. In the latter technique no processing is necessary except for the uniform illumination of the material to erase the space-charge pattern. An overview of the properties of the above-mentioned optical recording materials is given in Table 1.1. The maximum resolution F_{max} is given in linepairs per millimeter (Lp/mm).

In recent years, classical photographic films have been replaced by digital media. Charged-Coupled Device (CCD) or Complementary Metal Oxide Semiconductor (CMOS) sensors are commonly used devices to record images on electronic memory cards. These media have the striking advantage of being able to process and alter digital recordings at will, e.g. in order to eliminate imperfections of the illumination (see Section 1.6). In contrast to optical recording materials, complex developing processes are avoided which along with high acquisition frame rates allows qualitative and quantitative

Recording Material	Process	Type	η [%]	Reuse	Sensitivity [J/m^2]	F_{max} [Lp/mm]
photogr. emulsions	wet	ampl. phase	6 60	no	0.01-10	500-5000
DCG	wet	phase	100	no	100	5000
photoresists	wet	phase	33	no	100	1500
photo polymers	post-exposure	phase	100	no	10-1000	1000-2500
PTP	charge/ heat	phase	33	yes	0.1	250-600
photo refractives	none	phase	100	yes	1-500000	1000-5000

Table 1.1: General properties of optical recording materials. Source: [2]

analysis of the sample almost in real time. Longevity and reusability criterions are also met. However, while optical recording materials have a resolving capacity of up to 5000 Lp/mm (see Table 1.1), the distance between neighboring pixels of a high-resolution CCD is only $\Delta x \approx 5$ µm which yields a maximum resolution of about 100 Lp/mm if calculated by Equation 1.29. The minimum required exposure of CCD cameras is typically in the range of 10^{-4} to 10^{-3} J/m^2 [4] which is by far better than the average sensitivity of optical recording materials (see Table 1.1). Another advantage of digital recording means is their greater linearity in the exposure curve [4]. The maximum contrast in any interference pattern is achieved if the intensity ratio between reference wave and object wave is 1:1. In contrast, optical recording materials are subject to nonlinear effects that can be avoided if the intensity ratio between reference and object wave is 5:1 to 10:1 [4]. For transmission in-line holography with mostly transparent samples as implemented in our setups where reference and object wave have approximately the same intensity when interfering at the detector this linearity of CCD cameras is quite convenient as no filters have to be applied in order to change the intensity ratio. Both optical and digital recording devices need to control the total light energy impinging on the material over the exposure time, usually by means of mechanical or electronic shutters. Dynamic ranges of 8 bit apply to

both device types - a magnitude fully sufficient for hologram recording [4].

A CCD sensor functions in a three-step process [4]: Upon exposure the photons impinging onto each pixel are converted into electronic charges by the internal photoelectric effect. A charge transfer function then moves the packets of charge within the semiconductor substrate to memory cells. Finally, charges are converted to voltage and amplified.

In a CMOS sensor the inner photoelectric effect is also applied for the photon-electron conversion. Contrary to the CCD the electrons are not moved to a single read-out amplifier, but the conversion and amplification is carried out at each pixel individually. Thus, it is also called an active pixel sensor. CMOS cameras can be read out faster than CCDs and consume less power (about 10% [24]). Their fabrication is cheaper as both the image sensor function and image processing functions can be combined within the same integrated circuit. However, in order to be comparable to CCDs with respect to noise, dynamic range and sensitivity, CMOS sensors have to be relatively large. Small CMOS sensors are far noisier than CCDs of comparable size.

All experiments in this work have been done with one of the following digital recording devices:

1. CCD camera model AT200 (Photometrics, USA) equipped with a SI003 chip (1024x1024 pixels on an area of 24x24 mm^2) yielding a resolving capacity of $F_{max} = 21$ Lp/mm;

2. CCD camera model Lu160 (Lumenera, Canada) with a CCD image sensor (1280x1024 pixels on an area of 8.2x6.6 mm^2) with a maximum resolution of $F_{max} = 77$ Lp/mm;

3. CMOS camera model CSB4000CL (Toshiba-Teli, Japan) with a CMOS image sensor (2048x2048 pixels on an area of 12.3x12.3 mm^2) that can resolve $F_{max} = 83$ Lp/mm.

1.6   Digital In-Line Holography

In Section 1.2 the optical reconstruction of in-line holograms was described. Among the disadvantages of the method were [2]:

- The reconstructed image of the sample is superposed by the much brighter, defocussed source image.

- Additionally, the twin image superposes the reconstructed sample image.

Besides using various off-line geometries in order to avoid these problems, holograms can also be reconstructed numerically. This was already envisaged by Gabor, however, not until the development of computer technology it became possible to transfer the whole reconstruction process into the computer. Schnars and Jüptner [25] were the first to fully digitalize both recording and reconstruction processes of holograms. Fundamental work in the field of point source holographic microscopy has been done by the group of H.J. Kreuzer [11], a brief review of which is given in [26]. The use of electronic devices such as CCDs for holography without photographic recording as intermediate step greatly enhanced the importance of the method as it became possible for instance to calculate the phases of the recorded light waves directly from the digital holograms, without generating phase shifted interferograms [4]. The required setup to record a digital in-line hologram with spherical waves is depicted in Figure 1.15. Again, coherent light emitted by a laser illuminates a pinhole in an opaque material. The pinhole functions as a point source and emits by approximation a spherical wave ψ which is partly scattered by the object. The scattered object wave ψ_{scat} interferes again with the undisturbed part of the reference wave ψ_{ref} and creates an interference pattern, the hologram, on the two-dimensional detector screen.
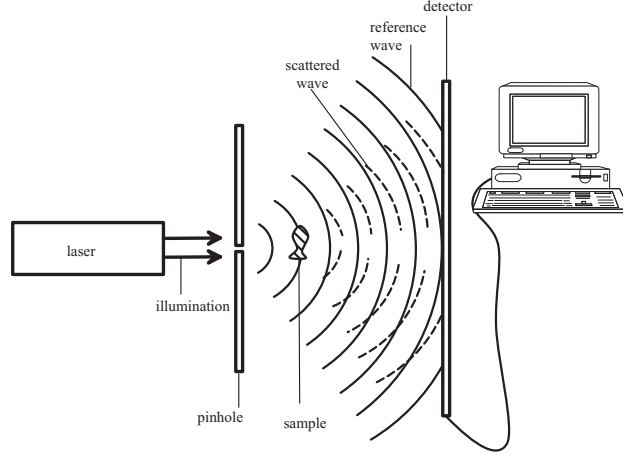
Figure 1.15: Schematic drawing of a setup used to record a digital in-line hologram

The intensity of the wave at the screen is given by

$$
\begin{aligned}
I(\mathbf{r}) &= |\psi(\mathbf{r})|^2 \\
&= |\psi_{ref}(\mathbf{r}) + \psi_{sc}(\mathbf{r})|^2 \\
&= |\psi_{ref}(\mathbf{r})|^2 + \psi_{ref}^*(\mathbf{r})\psi_{sc}(\mathbf{r}) + \psi_{ref}(\mathbf{r})\psi_{sc}^*(\mathbf{r}) + |\psi_{sc}(\mathbf{r})|^2
\end{aligned}
$$

$$. \tag{1.30}$$

As mentioned previously, the first term is the source term created by the undisturbed reference wave. The next term is the hologram term, followed by the twin image and the self-interference term. The latter three are caused through interference with the object wave [8].

The hologram is reconstructed with the help of a computer. In order to obtain the three-dimensional structure of the sample from the two-dimensional hologram on the detector the image is reconstructed at various distances from the point source. In reference to optical microscopy, the planes perpendicular to the optical axis in which specific virtual image points appear focused are sometimes referred to as focal planes.

For best results it is advisable to consider the following practical issues [27]:

- The implementation of an objective lens focussing the incident irradiation onto the pinhole increases the intensity of the light emitted by the

point source and thus decreases the necessary exposure time.

- The pinhole diameter should be in the same range as the wavelength of the used laser light in order to derive an approximately spherical wavefront.

- The sample should be small compared to the area illuminated by the point source and be positioned at a relatively short, yet sufficient distance from the pinhole. Most suitable is a distance of a factor 10^3 to 10^4 larger than the wavelength. Thus the condition for Fraunhofer diffraction $a^2 \ll d\lambda$ is met, where a is the dimension of the sample, d the distance between pinhole and sample and λ the wavelength of the illuminating light. Additionally the smallest possible distance d provides for the highest possible magnification ν, as the intercept theorem supplies $\nu = L/d$, L being the distance from the detector to the pinhole.

- The sample-detector distance as well as the dimension, pixel size and dynamics of the detector have to guarantee the resolution of the smallest interference fringes in order to ensure maximum resolution.

- The interference fringes caused by the reference wave and the object wave are recorded as an intensity distribution. Afterwards the sample is removed and the image of the source is recorded. Before the reconstruction a subtraction of the source image from the image with the sample is executed. This process is obligatory in order to minimize artifacts of the point source and eliminate disturbances.

Employing an adequate source-sample distance has another major advantage - minimizing the twin image effect. If that distance is about a factor 1000 larger than the wavelength the twin image appears at the same distance on the other side of the hologram, and the produced signal is smeared out over the whole length scale. Choosing an adequate distance thus enables the twin image term to be neglected [27].

Numerical Reconstruction

The basis for numerical reconstruction of real space information from a
hologram is the quantum mechanical simulation of a spherical wave's for-
ward propagation. In order to reconstruct with the method implemented by
Kreuzer [27] one starts at the hologram and calculates its propagation back-
wards to each diffraction point by the Kirchhoff-Helmholtz reconstruction
formula [27]:

$$K(\mathbf{r}) = \int_S \tilde{I}(\boldsymbol{\xi}) \ \exp\left(\frac{ik\boldsymbol{\xi}\mathbf{r}}{\xi}\right) d^2\xi \qquad (1.31)$$

where

S is the area of the detector. The integration is performed over the surface
S with the coordinates $\xi(X, Y, L)$, X and Y being the horizontal and
vertical coordinates of the screen, and L the distance of the source to
the screen center.

$\tilde{I}(\xi)$ is the intensity of the contrast image i.e. of the hologram of intensity I
that has been background-subtracted.

$k = 2\pi/\lambda$ is the wavenumber.

$\mathbf{r} = \mathbf{r}(x, y, d_{rec})$ is a position vector in the reconstruction plane, whose com-
ponents d_{rec} describe the reconstruction distance and x and y the po-
sition of the reconstructed image in the xy plane.

The complex function $K(\mathbf{r})$ (the sample image) is significantly structured
and different from zero only in the space region occupied by the object [27].
The wavefront $K(\mathbf{r})$ can be reconstructed in a number of planes at differ-
ent distances from the source, thus creating a three-dimensional image of
the sample. The absolute value of $K(\mathbf{r})$ represents the intensity image of the
sample, and its phase the sample's phase image. One usually calls the deriva-
tion of the function $K(\mathbf{r})$ from the hologram reconstruction. The graphical
display of $|K(\mathbf{r})|$ on a two-dimensional plane perpendicular to the optical

axis corresponds to an image in real space, similar to a focussed microscopy image. It is also possible to derive a three-dimensional image of the object by combination of a number of two-dimensional reconstructions of the same hologram [27].

It is not convenient to employ Equation (1.31) in order to obtain the reconstructed image $K(\mathbf{r})$ as the full execution of the integral for high-resolution images requires rather long compilation times. Especially the nonlinearity of the phase factor in the spatial domain complicates the computations. To correct this, a reconstruction method based on a slightly modified Kirchhoff-Helmholtz formula was introduced [11]. The major difference, however, are computations being performed on the coordinates and intensity values of the hologram prior to the reconstruction process.

Shortly summarized, the reconstruction method introduced by Kreuzer consists of the following steps [11]:

1. Transforming the intensity distribution measurements into a coordinate system that linearizes the phase factor in the Kirchhoff-Helmholtz formula;

2. Rewriting the linearized Kirchhoff-Helmholtz formula as a sum;

3. Interpolating the transformed integrand in the sum version of the Kirchhoff-Helmholtz formula onto an equidistant point grid;

4. Rewriting the Kirchhoff-Helmholtz formula as a convolution and applying Fast Fourier Transform (FFT) techniques in order to compute the sample image.

Reconstruction with LEEPS and DIHM

All recorded holograms in this thesis were numerically reconstructed with the program package LEEPS (Low Energy Electron Point Source) or its successor DIHM (Digital In-line Holographic Microscope) as developed by Kreuzer [11].

These programs, initially designed for electron sources, work just as well with photon sources. The algorithm is based on the above-mentioned Kirchhoff-Helmholtz reconstruction formula.

The first step is to subtract the source image from the hologram in order to obtain a contrast image (Figure 1.16). This image is now processed with
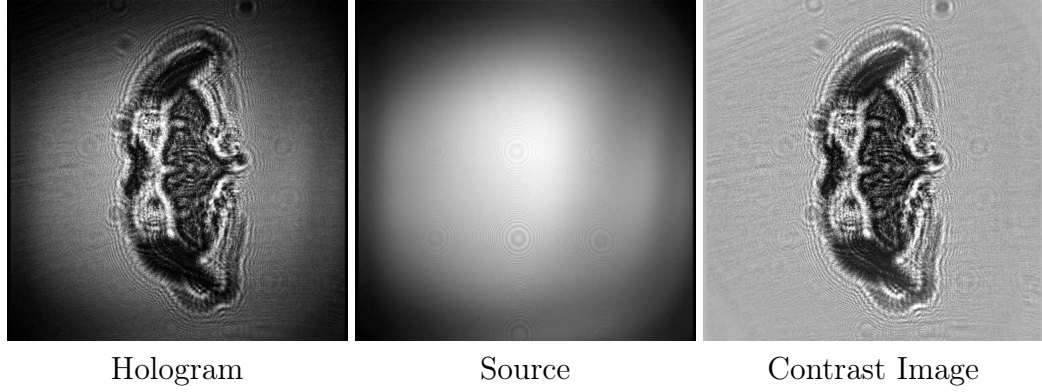

Hologram   Source   Contrast Image

Figure 1.16: Subtraction of the source from the hologram creates a contrast image.

the algorithm based on the Kirchhoff-Helmholtz transform (Equation 1.31), starting with the offset subtraction (Figure 1.17, left image). A constant value is subtracted in order to balance the differences between sample and source intensities.

Next, one applies the so-called bispline algorithm (center panel of Figure 1.17) which contains a number of operations. The nonlinearity in the phase factor of the Kirchhoff-Helmholtz formula is eliminated by introducing a new coordinate system (X',Y', R) which is related to the initial system (X, Y, L) through a coordinate transformation of the form [11]

$$
\begin{aligned}
X' &= XL/R \\
Y' &= YL/R \\
R &= \sqrt{L^2 + X^2 + Y^2}.
\end{aligned}
\tag{1.32}
$$

The transformation is applied to the coordinates of each single intensity value of the hologram, and its position changes in the initial xy plane. The initial image S had a rectangular shape, and the coordinate transformation results

in the barrel-shaped, transformed image S' inside the borders of S. The second part of the bispline algorithm is the rewriting of the double integral into a double sum. This step does not include a true changing of the hologram coordinates or intensity values, it merely describes the linearized version of the Kirchhoff-Helmholtz formula necessary for the numerical computation. Third, the transformed integrand of the sum version of the formula is interpolated onto an equidistant point grid. Holograms are normally recorded perpendicular to the optical axis on a flat detector with equidistant pixels. The coordinate transform that was performed first, however, transferred the equidistant grid to non equidistant points, resulting in a barrel-shaped set of coordinates. Theses intensity values of the hologram on non integer, non equidistant positions in the xy plane are not useful for FFT techniques. Therefore, a new, equidistant point grid is placed over the barrel-shaped coordinates, and the intensity value of the underlaying image is determined at each point of this grid. This is done by a bispline algorithm that compares the intensity values of the surrounding points of the underlaying grid in order to interpolate the intensity values of each new grid point. Due to the detector's final dimension artificial lines parallel to the image borders are created. These border frequencies can be removed again by applying a cosine filter (see right panel Figure 1.17).

Offset Subtraction   Bispline   Rectangular Cosine
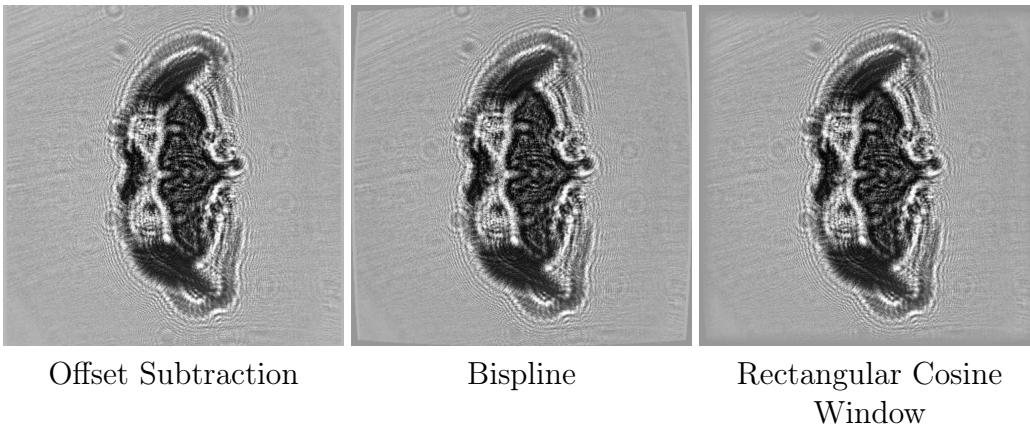   Window

Figure 1.17: Preparation for reconstruction of the hologram from a slice of a fly head

The hologram has now been prepared for the actual reconstruction. This
is done with the program package LEEPS or its successor DIHM, both
developed by the group of H.J. Kreuzer at Dalhousie University (Halifax,
Nova Scotia, Canada). These programs employ an implementation [11] of
the Kirchhoff-Helmholtz formula which basically applies a FFT in order to
rewrite the initial formula Equation 1.31 into a convolution.

As the exact source-sample distance can usually only be estimated, a set
of reconstructions at different distances is created. Figure 1.18 shows re-
constructions for source-sample distances of $d_{rec} = $ 190-210 µm. The third
image with the reconstruction distance $d_{rec} = 200$ µm seems to represent the
focal plane as even the tiny hairs in the peripheral regions of the fly head are
resolved.

A theoretical criterion to find the focal plane, i.e. the particular plane of
interest within the three-dimensional space formerly occupied by the object
has been developed by A. Eisele [28]. According to his criterion, the intensity
distribution through the focal plane has steeper flanks than those closer to
or further away from it.

1.7   Applications of Holography

Since Gabor [1] first proposed holography in 1948 as a new microscopic prin-
ciple to overcome the limitation of lenses the method has been applied in a
wide variety of fields. Especially after the full digitalization of both recording
and reconstruction processes of holograms [25] in 1994, the use of holography
in various domains increased greatly. Since then, three-dimensional images
can be recorded easily in various setups. In-line holography with spherical
waves as originally proposed by Gabor is the simplest realization of the tech-
nique. Digital in-line holographic microscopy (DIHM) is a technique to record
images with micrometer resolution [8, 11, 27, 29, 30], an overview of which is
given in [10]. In combination with an oil immersion technique [31], the nu-
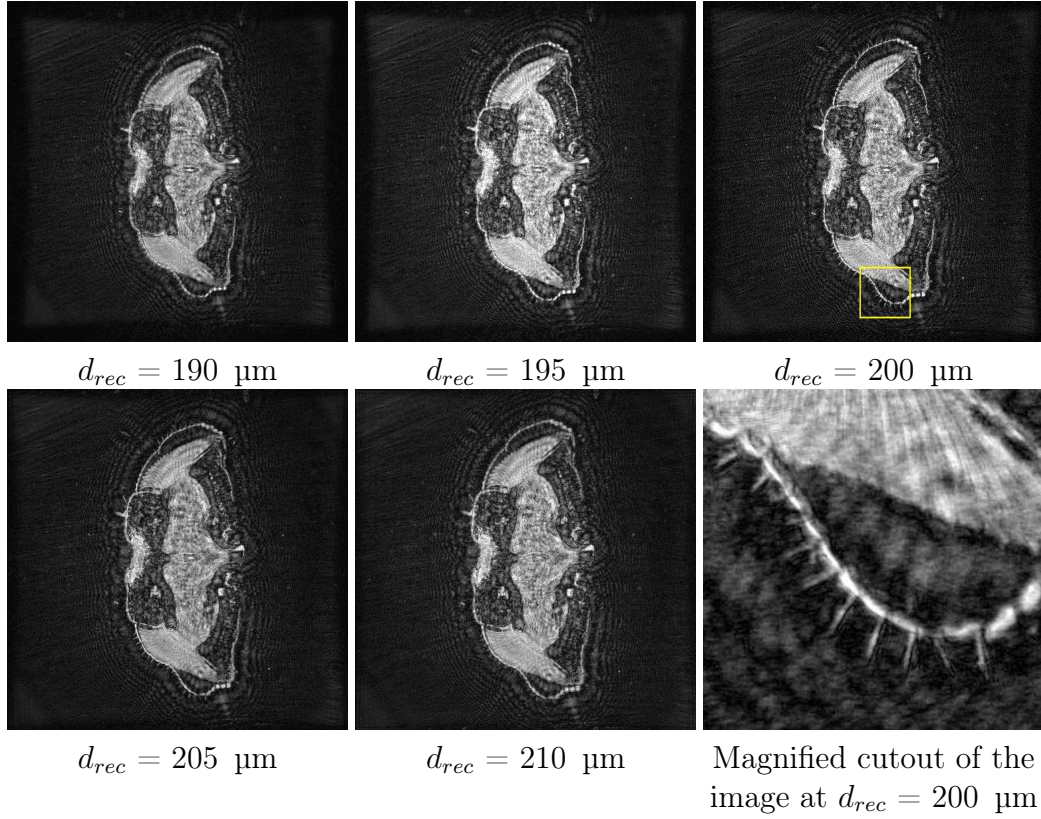merical aperture and thus the resolution can be increased even more. DIHM

Figure 1.18: Reconstruction at various distances, $\Delta d_{rec} = 5$ µm

can be extended into the fourth dimension by recording motion sequences of objects through a spatial volume. Xu et al. [32] were the first to record the trajectories of 5-10 µm thick marine algae in a single hologram by creating difference holograms from a series of each two consecutive holograms. Each combined hologram then contains information in four dimensions. Since then numerous 4D-tracking experiments were published by the group [31, 33–37], the latest of which showed the possibility to holographically record and reconstruct images of microscopic aquatic organisms down to a depth of 20 m. Underwater holographic imaging to measure distributions of marine organisms and characterize their size, swimming behavior and speed was implemented by Malkiel et al. [38, 39] in an in-line setup and by Watson et al. [40] who applied in-line as well as off-axis geometries. The latter group developed a waterproof camera that allowed the simultaneous acquisition of organisms

a few microns in size via in-line holography in such small concentrations as ten particles per cubic meter by off-axis holography. Plankton and other marine particles can thus be recorded in their natural environments down to a water depth of 100 m.

Owen et al. [41] were the first to use a shorter wavelength ($\lambda = 680$ nm) along with a CCD array and succeeded in resolving individual particles of 5 µm in diameter in a field depth of more than 25 cm. Moreover, using an even shorter wavelength ($\lambda = 473$ nm) it was possible to obtain three-dimensional images of marine protozoa *Ditylum brightwellii* [30]. The obligatory refocussing in optical microscopy is redundant due to the intrinsic three-dimensional nature of the method [11].

Another application of holography is in Particle Imaging Velocimetry (PIV) where visible laser light is used to detect tracer particles of a few microns in diameter. The flow in technical processes can thus be investigated. While classical PIV combined with a stereoscopic measuring method enables three-component(3C)-velocity data acquisition, only the extension of the method towards holographic PIV (HPIV) made the coverage of the complete three-dimensional space possible [42]. With the help of digital in-line video holography erosion processes have been investigated with a resolution of down to 25 µm [43].

Very short wavelengths in the soft X-ray range between the oxygen and the carbon edge are very interesting as here high resolution and in situ suitability are potentially combined. In this so-called water window (see Figure 1.19) between 2 and 5 nm the absorption coefficient of carbon is one order of magnitude larger than that of oxygen. This means that the phase contrasts of organic material differs from that of water by one order of magnitude which yields a sufficiently large contrast for imaging biological samples [44]. Holographic experiments with X-ray lasers have been successfully done [45], and a magnifying of the sample can be achieved via reconstruction with a longer wavelength. Thus images with a resolution of 10 µm were achieved with a few hundred picoseconds acquisition times [45]. Implementing soft X-rays ($\lambda = 1.89$ nm) Lindaas et al. [46] succeeded in the holographic imaging of complex biological specimens with a resolution of 40-50 nm. The hologram

was recorded as a relief pattern on a photoresist detector and read out by Scanning Force Microscopy (SFM) after the developing process. Reconstruction was then done numerically.

Holography is by far not limited to photon illumination. Electrons [47], neutrons [48] and gamma rays [49] have also been successfully used to create holograms.

1.8   Comparison of Holography to Other Microscopic Methods

As holography is used in this thesis as a microscopic method, a comparison between conventional microscopy and our method is drawn. Optical microscopy is the most commonly used magnification method of small objects. Manifold applications in medicine, biology, mineralogy, metallurgy and nowadays also in technical micro-manipulation are evidences of the immense significance of the method [9]. Apart from a sufficient transparency the observed specimen are not required to have any special properties. Living systems can be imaged damage-free. The highest resolution is achieved via oil immersion microscopy. When using light of the wavelength $\lambda = 400$ nm and an objective with a numerical aperture of 1.4 a resolution down to 200 nm can be obtained [50]. Optical microscopy is especially attractive due to the possibility to record all aspects of an image at the same time, for example with the above-mentioned CCD camera. It is, however, only possible to simultaneously image the projection of a thin plane. Thus, the thinner the layer the sharper the image turns out. When focussing onto one plane of a three-dimensional sample, all other planes above and below the one in focus are also illuminated, and the reflected light appears in the focal plane as a distorted halo of the sample. An interpretation of the image is thus hindered.

In confocal laser microscopy three-dimensional structures can be imaged. Confocal fluorescence microscopy has contributed greatly to understanding the functions of structural elements inside cells. The exciting illumination

propagating through an aperture is focused onto one point of the sample and the fluorescence emitted from this point is detected. Fluorescence emanating from other planes than the focal plane is blocked from the detector by a second aperture. This second aperture is positioned in the confocal position to the first one, i.e. in the exact position where the fluorescence from the point converges that had been the focus of the exciting illumination. Only this light can then pass the aperture and reach the detector.

In order to obtain a two-dimensional image, the illuminating beam scans the whole focal plane and displays the acquired information on a screen. A three-dimensional object is derived by mathematical combination of a number of these focus planes. With this technique structures with a lateral resolution down to 200 nm and a depth resolution of 500-900 nm can be recorded [51]. 4Pi-confocal microscopy [52] improves the spatial resolution in the far-field fluorescence microscopy to a lateral resolution of 200-220 nm and an axial resolution of 140 nm through the concept of two opposing large aperture lenses. As early as 1978 Cremer and Cremer [53] envisaged a resolution enhancement by increasing the accepting angle of a microscope to the full solid angle of 4π, an idea that was later practically realized by Hell [54]. Important insights on the architectural structure of mammalian cell nuclei were obtained [55]. The principle works as follows [54]: Because in conventional microscopy the spherical wavefront focused by the objective is only a section of a complete spherical wavefront, an elongation of the focus along the optical axis takes place. This results in a lower depth than lateral resolution. In 4Pi-microscopy a second objective is placed opposite to the first one, and the common focal point is illuminated with coherent wavefronts. The constructive interference results in a more spherical shape of the illumination and thus an improved depth resolution [54]. By a combination of Stimulated Emission Depletion (STED) and 4Pi microscopy the achievable resolution of confocal microscopy was extended to a lateral resolution of 16 nm and depth resolution of 60 nm [56].

The great advantage of fluorescence-based methods is their high sensitivity in respect to receptors as only the stained regions are imaged. Especially when fluorescent dyes can be brought into defined areas of a cell by genetic mu-

tation, experiments can be made under moderate fixing conditions. As the creation of a specific cell line or fluorescent protein gene transfection is quite demanding, most specimens are stained with fluorescent molecules from the outside. Therefore, the cells have to be killed and made permeable before antibody-bound dyes can be added. Selectively coupled fluorescence markers can then be imaged by fluorescence microscopy. Especially the permeabilizing mostly is connected with massive structural changes. Furthermore, anisotropic diffusion might result in an inhomogeneous dyeing of the sample. The danger of destroying the fluorescent molecules (photobleaching) also complicates measurements. Another problem is introduced by the potentially damaging high energy exposure of the sample due to the intensity of the exciting laser. This is necessary as the fluorescence yield is limited and dyes emit into a larger solid angle than can be captured by the objective. As confocal laser microscopy is a scanning technique, simultaneous imaging of the different object points is not possible. Most dynamic processes, however, take place a lot faster than the time required to record a three-dimensional image section, demanding the sample to remain still for a certain time. Long recording times is a drawback of all three-dimensional optical microscopy techniques which generally prohibits dynamic studies. Highly desirable would be a method with intrinsic, if possible chemical, material contrast that allows the high-resolution imaging of specimen in three dimensions.

Lateral resolution of the order of 80 nm has been achieved by near-field scanning fluorescence microscopy [57] where light is forced through the tip of a pulled optical fiber. When the tip is brought to nanometers away from a sample, the resolution is not limited by diffraction anymore but by the diameter of the tip aperture that can be as small as only tens of nanometers [58]. This near-field microscopic method, however, is only applicable to surface analyses.

A resolution in the range of the combined STED and 4Pi microscope can be obtained by reducing the wavelength as for example in X-ray or electron microscopy. Via X-ray microscopy samples with a resolution down to 15 nm [59] have been imaged, for example after deep freezing the cells by cryopreservation. At these low temperatures any biological activity, includ-

ing cell apoptosis, is effectively stopped, enabling information very similar
to that from a living cell to be obtained. In a tomographic setup in which
the object is recorded in multiple two-dimensional projections that are com-
bined afterwards, a three-dimensional image can be derived. Yet again, long
recording times are necessary.

The technique of transmission X-ray microscopy enables the simultaneous
coverage of all aspects although the integration times are several seconds to
a few minutes. However, due to the reduced radiation damage, longer ex-
posure times are possible before structures are altered. In scanning mode
the local structures of the absorption edges can be analyzed and additional
information can be gained from the images [60]. For cell biology X-ray mi-
croscopy presents a compromise between necessary specimen preparation and
achievable resolution.

The best resolving method is electron microscopy. The technique has to be
performed in high vacuum in order to prevent a scattering of the electrons by
air molecules. The electrons are emitted by a cathode and then accelerated
by an anode before propagating through an aperture and forming the elec-
tron beam. Electromagnetic coils focus the illuminating beam. In the case
of a Transmission Electron Microscope (TEM) the electrons that have prop-
agated through the sample are recorded, whereas in the Scanning Electron
Microscope (SEM) technique the electrons that are scattered by the object
reach the detector.

At an acceleration voltage of 10^6 V the wavelength of the electrons is 4 pm,
leading to a theoretical resolution of 2 pm [50]. Due to spherical abbera-
tion of the lenses and a small numerical aperture the best electron micro-
scopes have a resolution of 2 nm for biological samples [50]. Electrons cause
electrostatic charging which can lead to further distortions of the image.
Three-dimensional information is obtained by reconstruction of the different
projections in a tomographic setup. Samples require special pre-treatment:
Electrons have a low penetration depth, thus samples need to be cut into
extremely thin slices of 50-100 nm, a thickness corresponding to 1/200 of a
cell's thickness [50]. Freezing or drying methods need to be applied prior to
sectioning. Furthermore, evaporation with conducting material is necessary

in order to enable the electrons to discharge. Again, a general drawback is the high electron energy subjecting the biological samples to damage.

Concluding, all described microscopy techniques that can be applied with high acquisition frequencies do not achieve high resolution in three dimensions whereas high-resolution microscopy techniques require long acquisition times, work in scanning mode or are unable to function in situ.

1.9   Objectives

Photon holography in principle is able to combine most of the above-described desired characteristics:

- Simultaneous recording of all image aspects with high acquisition frequency

- Three-dimensional information obtainable from a single recording

- In situ recording in liquid environments possible

- High spatial resolution in three dimensions without the restriction introduced by the Abbe resolution limit due to the lensless nature of the method

Due to the presence of the phase information of the object wave contained in the interference pattern an intrinsic property of the hologram is the complete three-dimensional information that is available from a single recording. A mathematical combination of two-dimensional projection planes or a scanning technique are not necessary. Simultaneous covering of all image elements is inherent.

For holographic in situ experiments in liquid environments generally two wavelength ranges are applicable. In the UV to IR range (200-1000 nm) water has a very high transmission (Figure 1.19). As the achievable resolution is
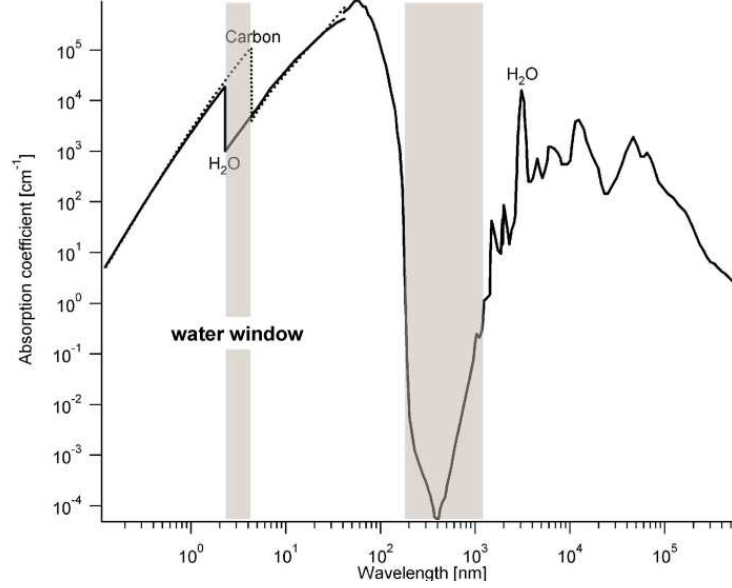
Figure 1.19: Water absorption spectrum. Sources: [61] and [62]

dependent on the wavelength, short wavelengths should be approached. Results presented in this thesis have been achieved in the UV to visible range ($\lambda = 355, 405, 534$ or 633 nm). The highest numerical aperture in this thesis was achieved with the setup described in Section 3.1. With the wavelength of $\lambda = 405$ nm, a detector side length of $D = 12.288$ mm and a pinhole-detector distance of $L = 9$ mm the numerical aperture yields $NA = 0.564$. The theoretical lateral resolution limit is then $\delta_{lateral}^{theo} = 359$ nm. The corresponding theoretical depth resolution is $\delta_{depth}^{theo} = 1273$ nm. Such values come close to those of expensive, commercial optical microscopes.

The second interesting wavelength range is the so-called water window at a wavelength of 2-5 nm (see Section 1.7). First experiments at the synchrotron facility BESSY II with picosecond radiation have been made. Especially with respect to the anticipated availability of free-electron X-ray lasers that will provide a high coherent photon flux in-line holographic microscopy with short wavelengths will become a highly useful tool for biological imaging.

Chapter 2

Materials

2.1 Pinholes
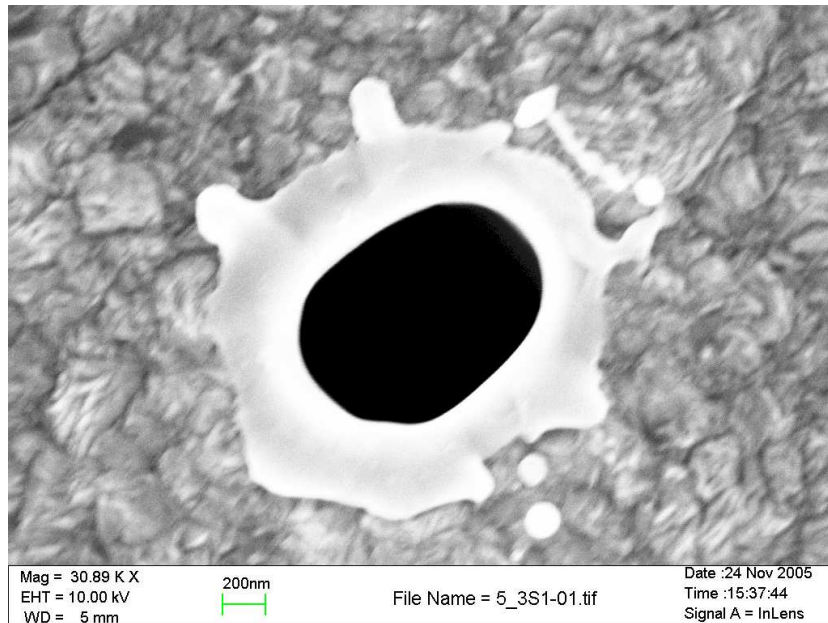
Figure 2.1: SEM image of a commercial 0.5 µm pinhole, magnification 30890x

Using imperfect spherical waves results in poorer resolution and complicates the reconstruction of the sample as the reconstruction algorithm assumes a

perfect spherical wave. Thus, the smallest possible pinhole diameter is desirable. Commercially available pinholes have a diameter down to 0.5 µm, an acceptable size for a laser wavelength of 405 nm. The pinholes used in this thesis were 0.5 µm in diameter and laser drilled into 2.54 µm thick nickel pieces mounted on stainless steel backings (National Aperture, USA). A Scanning Electron Microscopy (SEM) image of the pinhole's point-of-entry side is shown in Figure 2.1. These 0.5 µm pinholes, however, come with a tolerance of +0.3 µm, and thus do not necessarily qualify as having a diameter of the order of the wavelength. A slight drawback is also their rather elliptical instead of circular shape, although this does not particularly influence the imaging quality as long as the detector is fully illuminated. However, specially for the holographic experiments with synchrotron radiation (see Chapter 4) performed in our group, a minimization of the pinhole diameter is mandatory.

One approach was to evaporate a gold layer onto silicon nitride membrane windows (Silson, UK), remove the membrane by etching with hydrofluoric acid and subsequently drill a hole by Focused Ion Beam (FIB) milling as shown in Figure 2.2. A focused gallium ion beam sputters atoms from the surface because the collisions of the accelerated ions and the chemically bound surface atoms transfer sufficient energy to overcome the atom-atom binding energy and the material work function [63]. The method can then be used as a micro-machining tool to modify materials at the micro- and nanometer scale. Holes with a diameter down to less than 50 nm in lithium niobate substrates have been reported [64].

In the course of this work 0.75 mm x 0.75 mm silicon nitride membranes with a thickness of 100 nm on 5.0 mm x 5.0 mm silicon supporting frames with a thickness of 200 µm were coated with a gold layer > 350 nm, a value dense enough to prevent photons from passing through. The coating method used is called thermal evaporation, a high vacuum (10^{-7} mbar) process during which a metal block is heated up to a temperature close to its boiling point. The material evaporates and precipitates onto the cooler substrate, creating a thin film. For maximum smoothness the substrates are cleaned by heating to 300°C in the vacuum chamber prior to the evaporation process.

After cooling down to room temperature they are covered with 0.5-1.0 nm titanium as an adhesive and then finally with the gold layer. The thicknesses are controlled over the resonance frequency of an oscillating crystal present in the chamber.   The pinhole shown in Figure 2.3 was created by evaporat-
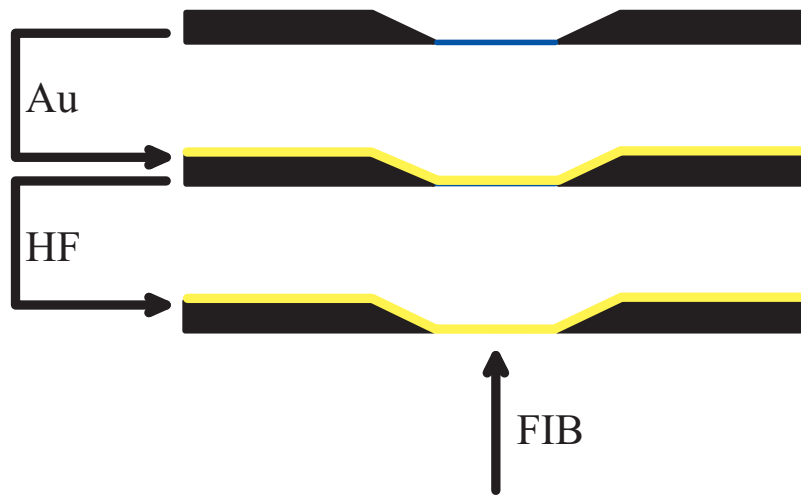

Figure 2.2: Schematic drawing of the procedure to manufacture pinholes with smaller apertures

ing 700 nm of gold onto the membrane (prepared by G. Albert, Institut für Physikalische Chemie, Universität Heidelberg) subsequent etching by applying a droplet of hydrofluoric acid for 30 min, followed by thorough rinsing with Millipore® water. Rendered smooth by etching, a hole was then drilled from the former membrane side. The milling was carried out by S. Albrecht at the New Materials and Biosystems Department (Max-Planck-Institut für Metallforschung, Stuttgart). Through this procedure pinholes with a diameter as small as 80 nm were attempted. It was, however, only possible to locate and measure the pinhole from the milling side (see Figure 2.3) by SEM. Hence, it could not be confirmed that the FIB had milled through the complete gold layer. With the same method, another attempt was made by R. Barth [65] at the Nanofabrication Laboratory (University of Western Ontario, London, Ontario, Canada). There, holes as small as 150 nm were

milled into a 700 nm thick gold foil which was later confirmed to go through
the complete layer by SEM. The decreased pinhole size, however, results in
a decreased amount of photons passing through the aperture and thus in
increased acquisition times. It is therefore necessary to find a compromise
between resolution and time expenditure. As the wavelength of 405 nm does
not necessarily require pinholes of this small size, and due to the rather
complex fabrication procedure these pinholes were not used for holography
with laser light, but merely for the experiments at the synchrotron radiation
facility (BESSY II) in Berlin (see Chapter 4).
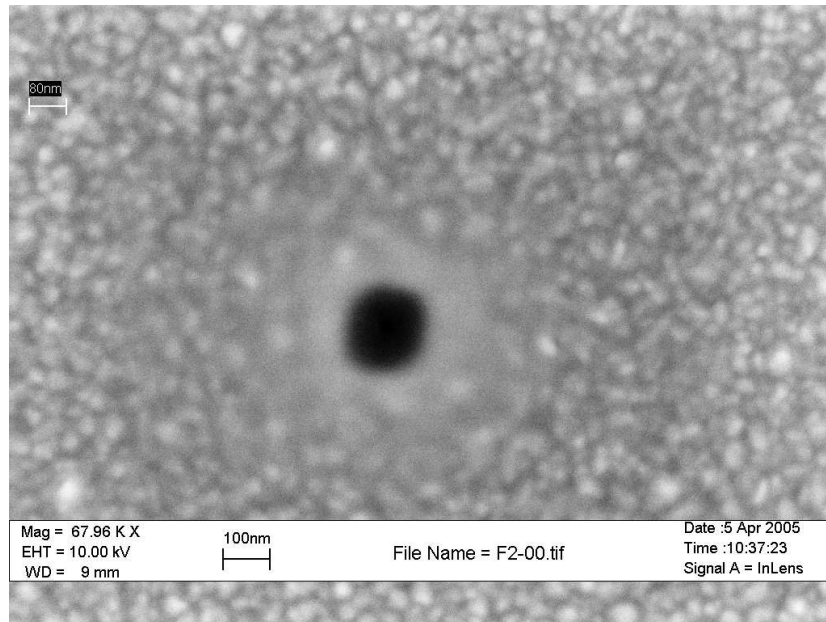
Figure 2.3: SEM image of a FIB-milled 80 nm pinhole, magnification
67960x

2.2   Samples

Mainly polystyrene beads, cells and lithographic structures were investigated
by holographic microscopy in the experiments presented in this thesis. Due
to their clearly defined size polystyrene beads allow straightforward compar-
ison between compound microscopy and holography. Samples are relatively

easy to prepare and very reproducible. Furthermore, the beads' uniform size distribution allows a direct evaluation of the method's resolution. The transparent beads absorb very little light; bead samples reveal their structure through local variations of the refractive index i.e. that of polystyrene opposed to that of air, causing a phase change of the transmitted light waves. Cells do not absorb a lot of light either because of their small thickness. Their manifold structures, however, make them interesting phase objects, especially due to the different organelles of various shapes and sizes. Additionally, their imaging properties were investigated particularly with regard to a possible application of holography to study biological phenomena.

Especially concerning holographic experiments with synchrotron light in order to elucidate contrast sensitivity in greater detail, e.g. in comparison to polystyrene beads, thin lithographic structures were prepared. These structures are also phase objects that present their structures through variation of the phase of the passing light waves. Although more complex to prepare, they have the advantage of being well-defined in size, especially quite thin, and also very stable. Furthermore, their steep flanks act more like step functions on the incident illumination, enabling easier resolution determination.

2.2.1   Polystyrene Beads

Polybead® polystyrene microspheres (Polysciences, USA) with diameter 2.9, 0.752, 0.500, and 0.356 µm were used. 2.5% (w/v) solids in an aqueous suspension as delivered were further diluted with Millipore® water to a concentration of $\approx 0.0025\%$ (w/v). 50 µl were distributed on an object slide of 1 mm thickness and air-dried under varying angles depending on the desired particle density.

2.2.2   Fibroblast Cells

Fibroblasts are cells in the mammalian connective tissue, for example in the skin. Cultured on flat substrates they spread on the surfaces and abandon their original round shape. The cells used for holographic imaging are the rat

embryonic fibroblast line REF52 wt and were cultivated in the cell culture of the Biophysical Chemistry (BPC) group of Prof. Dr. J.P. Spatz (Institut für Biophysikalische Chemie, Universität Heidelberg). Their cultivation followed protocols established in the BPC group [66]:

Cell Cultivation

1 mm thick object slides were cut into 5 mm wide sections and cleaned with ethanol followed by mechanical cleansing in the ultrasonic bath in the glass cleanser RBS 50 cleaning concentrate. After drying under a nitrogen flow the glass sections were cleaned in piranha solution (one part 30% hydrogen peroxide and one part concentrated sulphuric acid), rinsed with Millipore$^{®}$ water and again dried under nitrogen flow. For disinfection the objects slides were kept in 70% ethanol for 30 min. Three slide sections at a time were put into a petri dish and rinsed with Phosphate Buffered Saline (PBS) three times. Afterwards, the cell culture medium Dulbecco's Modified Eagle Medium (DMEM) with 3.7 g/l sodium hydrogen carbonate, 10% Fetal Bovine Serum (FBS) and 1% L-glutamine were added. The sodium hydrogen carbonate guarantees an enriched atmosphere of 10% carbon dioxide in the incubator. Subsequently, 3000 cells per petri dish were added and incubated in a Hera Cell Incubator (Kendro Laboratory Products, Berlin) for 24 hrs at 37°C. The relatively small number of seeded cells was chosen to yield surfaces with well-adhered and clearly separated fibroblasts.

Fixation

Fixation was done by inserting the sample into glutaraldehyde solution (4% glutaraldehyde in PBS) for 30 min. Afterwards, the fixation medium was subsequently exchanged with ethanol by immersing the slides in ethanol-water mixtures with percental ethanol concentrations of 50, 60, 70, 80, 90 and 100 for 10 min, respectively. The 100% ethanol was exchanged twice. The slides stayed overnight in 100% ethanol that was again exchanged the day after.

Critical Point Drying
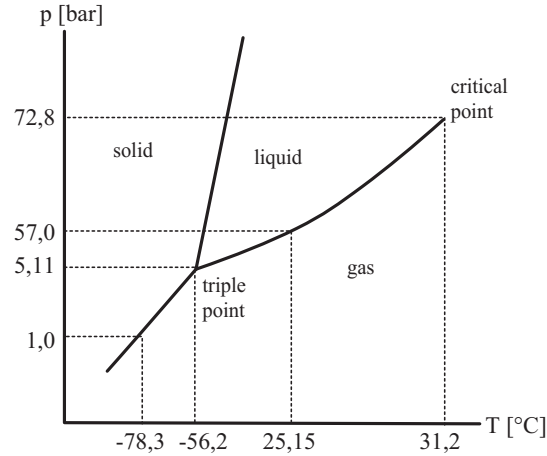
Figure 2.4: Phase diagram of carbon dioxide after [67]

During the phase change from liquid to gas that the intracellular water undergoes when a cell is subject to an air-drying process, the strong surface tension occurring at the gas-liquid interface can damage the delicate structures inside the cell. In order to avoid this phase transition, one applies a technique called critical point drying [50]. The critical point marks the end of the phase boundary between the gaseous and the liquid state. Above this point the gaseous and the liquid phase are indistinguishable as their densities are equivalent. The critical point of water can only be reached at high pressure and temperature conditions (T = 374.2° C and p = 220.3 bar [67]) making it easier to use carbon dioxide instead whose critical point is at T = 31.2°C and p = 72.8 bar [67]. Water and liquid carbon dioxide are not very miscible, requiring a gradual exchange with an intermediate medium, for example ethanol. Afterwards, the samples are transferred into a pressure chamber where the ethanol is gradually exchanged with carbon dioxide, being liquid at room temperature and a pressure of 55 bar. After the sample is completely soaked with pure carbon dioxide, the temperature in the pressure chamber can be raised, taking the solution from subcritical to supercritical fluid. The liquid changes to gas without the phase transition that usually damages the sample. The gaseous carbon dioxide is discharged slowly and in

a controlled manner. The pressure sinks but the temperature needs to stay above the critical value. As soon as atmospheric pressure is reached, the sample can be taken out completely dried and with well-preserved features. The above-described method was implemented with a critical point dryer CPD 020 (Bal-Tec, Liechtenstein).

2.2.3 Lithographic Structures

Lithography is a process to selectively remove parts of a thin film by transferring a pattern from a previously designed mask to a light-sensitive chemical, the resist, on the substrate. Shape and size of the structures are very well controllable and due to the existence of a mask highly reproducible [9].
The method consists of a number of processing steps. The substrate is first superimposed with a thin layer of resist by spin-coating, i.e. spreading an excess amount of the chemical over the substrate by centrifugal force. Depending on the amount of material one wants to remove, either a positive or a negative resist is chosen. When using a positive resist the part that has been exposed to light is dissolved by the developer while the unexposed part remains insoluble and forms the structure. On the contrary, the light-exposed part of a negative resist is insoluble to the developer and forms the remaining pattern while the unexposed portion is soluble to the developer. After spin coating, the substrate is soft-baked in a convection oven or on a hot plate in order to drive off excess solvent. The third step is the exposure, in our case done by electron beam as the dimensions of the created structures of a few micrometers and below are several magnitudes higher than the electron wavelength thus eliminating diffraction effects [9]. A post-exposure bake may be performed before developing in order to reduce standing wave phenomena caused by the destructive and constructive interference patterns of the incident light [9]. The final step is the developing step where the substrate is immersed into the developer in order to remove the unwanted resist layers.

Random Forms and Shapes

One task in this thesis was the creation of a sample set especially for holography with synchrotron radiation (see Chapter 4). Structures were designed to contain random forms and shapes, including dots and lines in order to investigate their imaging behavior. Tapered lines with 1 µm width at their broadest end were used to survey the sensitivity of the method in respect to structural sizes below the resolution limit. Figure 2.5 shows the de-
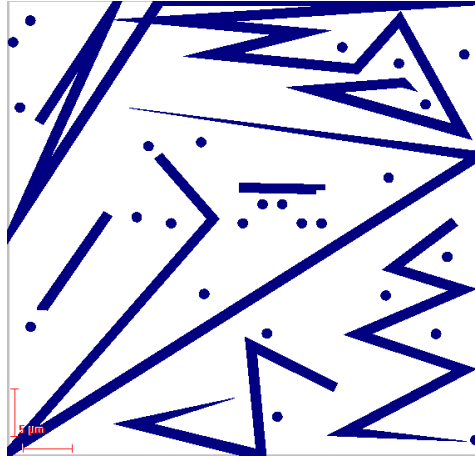

Figure 2.5: Design sheet of the test structure field

sign sheet for a 50 x 50 µm^2 field. A material commonly used as sample mount for imaging with X-rays is silicon nitride due to its high transmission properties for soft X-rays. The substrates were 1.0 x 1.0 mm^2 silicon nitride membranes (Silson, UK) with a thickness of 100 nm. A matrix of 6 x 6 fields with 100 µm wide free spaces in between was programmed to cover the membrane. The empty fields in between the writing field ensured ample space for the reference wave to pass undisturbed. The structure preparation procedure was as follows: The membrane was first made conductive by carbon thread evaporation with the coating system MED 020 (Bal-Tec). A special carbon thread is stretched between two high current electrodes and completely degassed by heating to a white glow. Afterwards, a current is run through the carbon thread to flash-evaporate it. The carbon atoms released into the vacuum chamber form a diffuse cloud of atoms condensing on the

specimen, thus forming an even conductive film. Subsequently, the negative electron beam resist SU8-2025 (MicroChem, USA) was spin-coated onto the substrate in a three-step ramping process in the spinner model TT200-8 (LP-Thermtech, Volkertshausen). After the resist has been applied the spin coater gradually increases speed to 4000 rpm within 5 s. It then runs at 4000 rpm for 60 s before returning to 0 rpm within 5 s. A film thickness of approximately 700 nm is created which was confirmed by SEM. The unexposed resist was handled under yellow light at all times to avoid unwanted exposure. The prebaking was done on a hot plate at 60 and 90°C for 1 min, respectively. The thus prepared substrate was then exposed to an electron beam in the SEM LEO1530 Gemini (Zeiss, Jena). The structures were written with an intensity of 125 mJ/cm^2 which was achieved by setting the SEM voltage to 5 kV and the area dose to 25 µC/cm^2. After the exposure the structures were post-exposure-baked on a hot plate at 60 and 90°C for 2 min, respectively, before being developed by immersion of the substrate into SU8 developer (MicroChem) and gentle stirring for 90 s. The final step included rinsing the structures with deionized water and successive drying in an argon stream. Figure 2.6 shows a SEM image of the complete membrane. The individual structures exhibit the designed form, although some of them
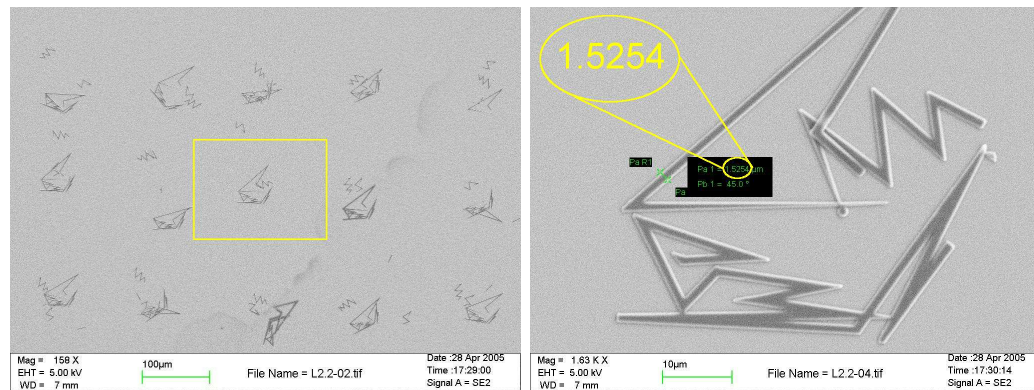
Figure 2.6: SEM images of the designed random forms and shapes, magnifications 158x (left) and 1630x (right)

are slightly shifted. A broadening of the structures can also be observed as the line width that was set to be 1 µm is now 1.5 µm. Later experiments showed that the resist requires an electron beam intensity of approximately

600 mJ/cm^2 which is almost 5 times higher than the above-used value. This explains the observed drift of the structures due to the insufficient depth of crosslinking, enabling the developing solution to wear away the lower parts of the structures that were not reached by the electron beam. Without a stable basis the remaining parts of the structure were subject to drifting. A broadening of the structures can most probably be reduced by decreasing the step size to less than 44.25 nm. However, with the current computer used to control the lithographic process this is not possible because of the limited clock signal frequency of the processor. As no explicit structure form or order was planned in the first place and the lines were still tapered, neither the even more random effect than intended nor the slight broadening impaired the structures' application as resolution test objects. The displayed structures have been imaged with synchrotron radiation at BESSY II during the beamtime of 2005 [68].

Siemens stars
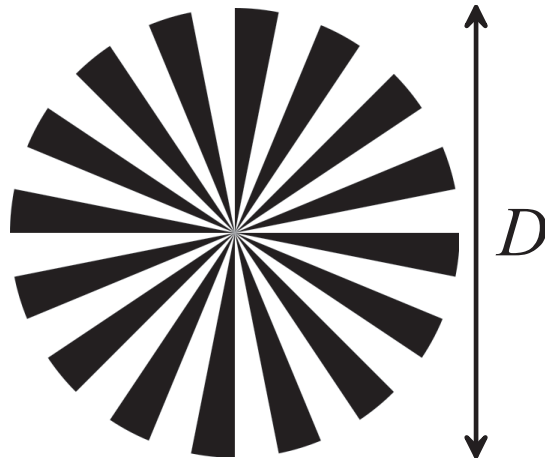
Figure 2.7: Resolution testing pattern Siemens star

A Siemens star (Figure 2.7) is a device of diameter D used to test the resolution of optical instruments. It consists of alternating black and white triangular sections that theoretically only meet at the exact center of the star. With increasing distance from the center the distance between the

black and white sections increases. An imaging device with limited resolving
ability cannot reproduce this pattern and the triangles appear to touch at
some distance from the center. A blurred spot, the so-called gray ring, ap-
pears at the center of the star. Its diameter d determines the resolution δ of
an optical device:

$$\delta = \frac{\pi d}{n}, \tag{2.1}$$

d being the diameter of the gray ring and n the number of the black and
white sections. Resolution test patterns for optical devices like the Siemens
star are commercially available. However, even the smallest ones available
have dimensions too large for our purposes, e.g. the Siemens star testing
plate (Linos Photonics, Munich) with a diameter of $D = 25$ mm consisting
of 72 opaque and transparent sections. The smallest structure is 8.7 µm [69].
Furthermore, no variation of the used substrates is given, i.e. silicon nitride
in particular is not available. In order to obtain test structures which can be
applied for the wide range of wavelengths used for holographic experiments
in our group, i.e. from red visible laser light (633 nm) down to soft X-rays
(1.89 nm) a large variety of structure sizes is desirable. By electron beam
lithographic structures can be designed at will. A test array of 5 x 5 Siemens
stars was created that theoretically allows the testing of resolution over a
range from $\delta = 26.18$ µm down to less than $\delta = 210$ nm within one sample
(see Table 2.1 and Figure 2.8, top image). Within one row the diameter of
the stars decreases in order to be able to center each star in the illuminated
field of view and still leave enough free space for the reference wave to pass
unscattered for varying field of view dimensions. This is especially important
for X-ray holography where the synchrotron radiation wavelength can be
tuned and the size of the Airy disc depends on the wavelengths diffracted
at the pinhole (see Equation 1.14). This in turn results in changing fields
of view. The sample within the vacuum chamber, however, cannot easily
be exchanged during one measurement which makes flexibility within one
sample desirable. Within one column, the size of the stars remains the same.
This should lead to a constant resolution for the same optical instrument
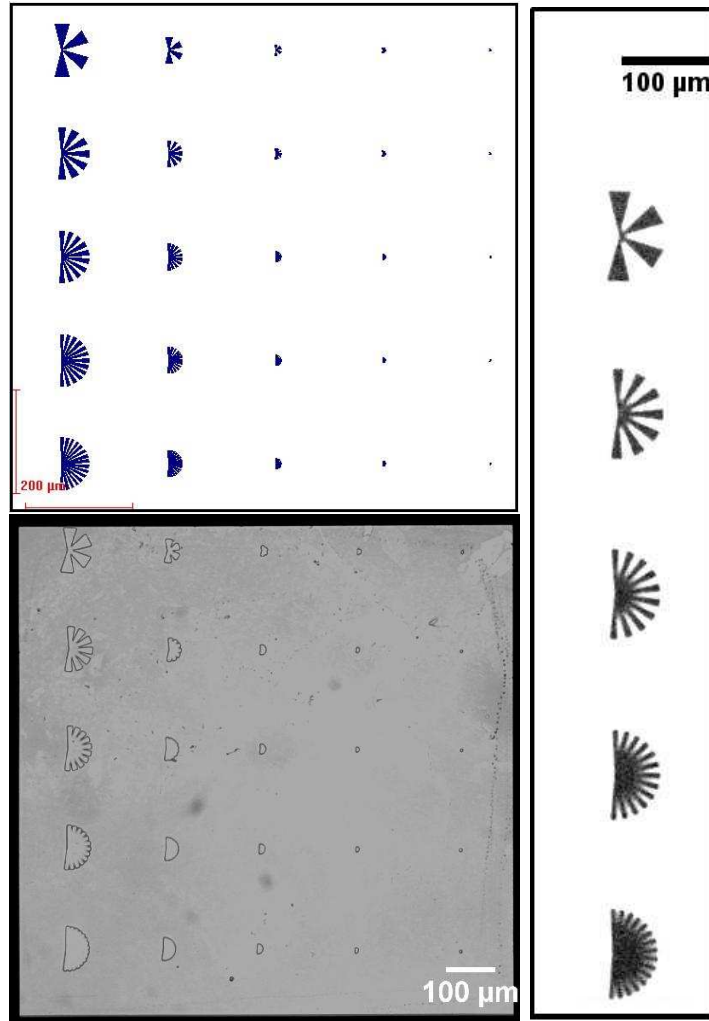
Figure 2.8: Custom designed Siemens star array for resolution testing. *Top*: Design sheet *Bottom:* Microscopy image of the array on Si_3N_4, Zeiss A-Plan 10x, $NA = 0.25$ *Right:* SEM image of the array on a glass substrate, magnification 72x

as the diameter of the unresolved gray spot should increase with increasing number of sections. The reason why only semi-circles were drawn is again to leave enough space for the reference wave to pass undisturbed.

The sample production steps for the Siemens star array were as follows:

1. Carbon thread evaporation as described above;

2. Coating with SU8-2025 by spin coating (ramp to 4000 rpm in 5 s, dwell

n=12 D=100 µm $\delta \leq 26.18$ µm	n=12 D=50 µm $\delta \leq 13.09$ µm	n=12 D=20 µm $\delta \leq 5.24$ µm	n=12 D=10 µm $\delta \leq 2.62$ µm	n=12 D=4 µm $\delta \leq 1.05$ µm
n=24 D=100 µm $\delta \leq 13.09$ µm	n=24 D=50 µm $\delta \leq 6.54$ µm	n=24 D=20 µm $\delta \leq 2.62$ µm	n=24 D=10 µm $\delta \leq 1.31$ µm	n=24 D=4 µm $\delta \leq 0.52$ µm
n=36 D=100 µm $\delta \leq 8.73$ µm	n=36 D=50 µm $\delta \leq 4.36$ µm	n=36 D=20 µm $\delta \leq 1.74$ µm	n=36 D=10 µm $\delta \leq 0.87$ µm	n=36 D=4 µm $\delta \leq 0.35$ µm
n=48 D=100 µm $\delta \leq 6.54$ µm	n=48 D=50 µm $\delta \leq 3.27$ µm	n=48 D=20 µm $\delta \leq 1.31$ µm	n=48 D=10 µm $\delta \leq 0.65$ µm	n=48 D=4 µm $\delta \leq 0.26$ µm
n=60 D=100 µm $\delta \leq 5.24$ µm	n=60 D=50 µm $\delta \leq 2.62$ µm	n=60 D=20 µm $\delta \leq 1.05$ µm	n=60 D=10 µm $\delta \leq 0.52$ µm	n=60 D=4 µm $\delta \leq 0.21$ µm

Table 2.1: Parameters of the designed Siemens star test array

    at 4000 rpm for 60 s, ramp down to 0 rpm in 5 s);

3. Prebake on a hot plate at 60 and 90°C for 1 min, respectively;

4. Exposure at 20 kV with an area dose of 30 µC/cm^2, step size 68.67 nm;

5. Post-exposure bake on a hot plate at 60 and 90°C for 2 min, respectively;

6. Develop with SU8 Developer (MicroChem) for 1.5 min under gentle stirring;

7. Rinse and dry.

The array (Figure 2.8) with a total area of 1.0 x 1.0 mm^2 was created over 25 individual stars in 100 x 100 µm^2 writing fields. Due to this higher magnification (688x) the electron beam is focussed onto a smaller spot which avoids exposure of unwanted parts of the sample. The step size with these settings is 68.67 nm. The higher electron beam intensity compared to the one used previously resulted in the retention of the structures in their designed

position even after developing. The bottom image of Figure 2.8 shows a silicon nitride window upon which the structures have been written with the above-described parameters in order to be able to use them for experiments with soft X-rays. Interestingly, the structure exhibits a broadening of the designed line widths, limiting the achievable probing resolution to a value far beyond the theoretical resolution of the geometry that was calculated to be 725 nm. By using the same protocol, on a glass substrate less broadening of the structures was measured by SEM (Figure 2.8, right image). The image corresponds to the first column of the planned array, and using Equation 2.1 the measured unresolved circles of $d = 11.48, 22.95, 37.20, 45.74$, and 59.13 µm yield probing resolutions of 3.01, 3.00, 3.25, 2.99, and 3.10 µm, respectively. Of course, this is also beyond any interesting probing resolution, making the samples useless for their designated purpose. The consistency of the obtained resolution for the combination of the chosen resist and the geometry, however, nicely proves the applicability of the designed pattern for resolution testing. Samples for the next beamtime will be prepared using a less viscous resist, e.g. AR-N 7500.08 (Allresist, Strausberg) that has been reported to produce similar patterns with better resolution [70].

2.2.4 Microfluidic Channels

In addition to 3D experiments with various static samples, DIHM aims to extend its application into the fourth dimension, e.g. by tracking particles in a fluidic environment over time. Fluidic structures on the micrometer scale are usually fabricated by lithography with light or particle beams as well as by wet and dry etching and subsequent sealing by silicon fusion or anodic bonding [71]. In the case of polymers, microchannels are often manufactured by injection molding [72] or hot embossing [73] prior to sealing by welding and gluing processes. The microscale fluidic structures were fabricated by the Institute of Microstructure Technology (IMT) (Forschungszentrum Karlsruhe). To create the bottom of the nanochannel, polymethylmetacrylate (PMMA) resist is spin-coated onto a glass substrate. The structuring then is done by hot embossing, deep UV lithography, electron beam lithography or,

for maximum aspect ratio, by deep X-ray lithography. The required X-ray
mask is created by electron beam lithography and electroplating of a 2 µm
high gold pattern on a 2.7 µm thick titanium membrane. The channels are
then sealed by a bonding technique recently developed at the IMT [71] which
is applied to both the molded structure and the lid. The surface of the poly-
mer is exposed to UV light which causes the glass transition temperature of
a thin surface layer of the polymer to drop. The parts are then welded by
heating them up to a temperature above the glass transition temperature of
the photodegraded layer but below the one of the underlying bulk polymer
and then pressed together. The relatively low welding temperatures allow
structure details even in the submicron range to remain dimensionally stable
while at the same time ensuring the liquid tightness of the channel. Being
entirely glue-free, the technique also provides for chemically homogeneous
channel walls.

Experiments were also done with commercially available flow cells (Ibidi -
Integrated BioDiagnostics, Munich). Their micro-slides consist of a high
optical quality plastic slide bottom of the thickness of a standard glass cov-
erslip. The smallest channel in production has the following dimensions:
height 0.4 mm, length 17 mm, and width 3.8 mm. It contains a volume of
30 µl. PVC tubes with an inner diameter of 2.0 mm can be coupled to the
slide by Luer-lock adapters.

2.3   Optical Fibers

Another question addressed within this work was the applicability of optical
fiber exit surfaces as alternative sources of coherent, divergent wavefronts for
DIHM to the commonly used pinholes. The fibers used were 460HP single
mode fibers (Thorlabs, USA) with an operating wavelength of 450-630 nm.
Their mode field diameter in the silica core is 3.5 $\pm$ 0.5 µm, their silica
cladding 125 $\pm$ 1.5 µm and their dual acrylate coating 245 $\pm$ 15 µm. Max-
imum attenuation is less than 30 db/km and the numerical aperture (NA)
0.13. Prior to implementation in the setup both ends of the fiber were cleaned

in ethanol, mechanically stripped with the MS-1-FS Tool (Micro-Strip, USA) and then cleaved with the XL410 Fiber Cleaver (Thorlabs). This procedure ensured clean, perpendicular interfaces (Figure 2.9) which produced illumination that was not distorted by artifacts induced by protruding glass portions.
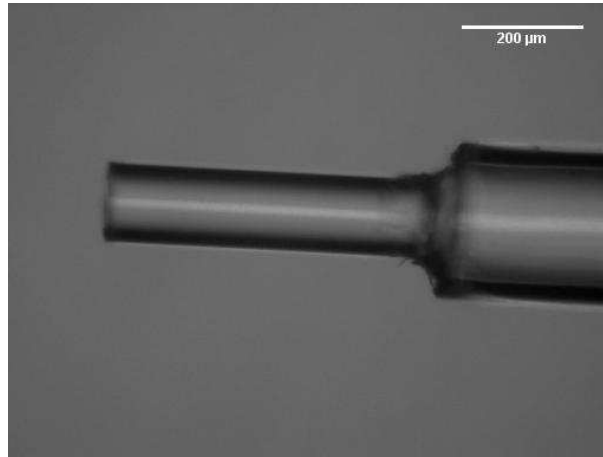

Figure 2.9: Microscopy image of a cleaved fiber, Zeiss A-plan 20x, $NA = 0.45$

2.3.1   Mechanical Drawing

Tapered optical fiber ends were produced with a CO_2 laser-based Micropipette Puller model P-2000 (Sutter Instruments, USA). By this method, an axial draw is applied to both ends of the fiber while the surrounding of the desired point of rupture is scanned by the laser. The heat softens the silica which is tapered under the drawing. If the pulling velocity reaches a certain value, the so-called trip point, a stronger pull is activated that finally breaks the fiber and creates two tips. The following settings were applied: The

HEAT	FILAMENT	VELOCITY	DELAY	PULL
350	0	20	126	150

Table 2.2: Settings applied for mechanical pulling of silica

parameter HEAT describes the power of the laser and thus the energy that

is transferred to the glass. FILAMENT controls section length and rate of the laser scanning. FILAMENT 0 means a 1 mm section of the fiber is heated. The parameter VELOCITY sets the velocity the pulling system needs to have reached before the strong pull is activated. As the velocity during the weaker pull is dependent on the viscosity of the fiber which in turn is dependent on the temperature of the glass, this is an indirect measurement of the glass temperature. The trip point at which the strong pull is activated, is thus also dependent on the glass temperature. PULL describes the force of the strong pull. The stronger the force the smaller the apex diameter and the longer the taper. DELAY controls the start of the strong pull relative to the deactivation of the laser. The higher it is the colder is the glass before the strong pull is activated. Thus, an increase of the DELAY value results in a decrease of the taper length and an increase of the apex diameter. The setting DELAY 126 activates the strong pull 2 ms before the laser is turned off. Prior to the mechanical drawing, the 10 cm long fiber pieces were cleaned with ethanol and about 1 cm in the center was stripped off its coating by immersion in chloroform for 60 s. Typical taper lengths of the thus processed fibers (Figure 2.10) are about 1 mm, opening angles are below 10°, and the apexes about 1 µm in diameter [74].
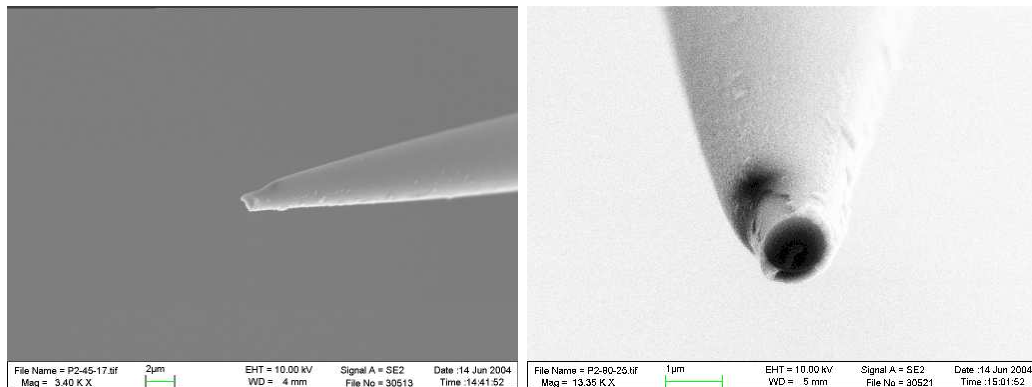
Figure 2.10: SEM images of mechanically drawn fiber tips, magnifications 3400x (left) and 13350x (right)

Chapter 3

Resolution Enhancement in Digital In-Line Holographic Microscopy

As pointed out in Section 1.7, digital in-line holography has emerged in recent years as a novel microscopy technique [10, 29, 30]. The shortest visible wavelength used for digital holographic microscopy so far published was $\lambda = 405$ nm. With this wavelength and a pinhole of 0.5 µm in diameter 1.09 µm microspheres in a self-assembled cluster were resolved [75]. The numerical aperture of the setup was 0.46. In this chapter by use of the same wavelength ($\lambda = 405$ nm) and the same pinhole diameter (0.5 µm) images with a numerical aperture as high as 0.564 are presented, yielding a theoretical lateral resolution of 359 nm. Particles and particle dimers down to a size of below 500 nm are resolved. Results on imaging larger agglomerates of particles are presented and the effect of oil immersion as first proposed by Garcia-Sucerquia et al. [26] on the obtained imaging quality is discussed. The shortest illuminating wavelength used in immersion DIHM so far published was $\lambda = 532$ nm with a numerical aperture of 0.39, which led to an effective wavelength and numerical aperture of 355 nm and 0.55, respectively [26]. In our setup the wavelength used was $\lambda = 405$ nm and the numerical aperture 0.414. The implementation of immersion DIHM increased the numerical

aperture to 0.572. For the first time, clusters consisting of polystyrene beads
as small as 0.752 nm could be imaged in excellent quality. Furthermore,
fibroblast cells with a diameter of about 200 µm were imaged with a numer-
ical aperture of 0.524, and the results are compared to conventional optical
microscopy.

3.1   Experimental Setup

All holograms presented in this chapter were recorded with one of the two
following setups. In the first setup, implemented in the laboratory of Prof.
Dr. H.J. Kreuzer (Dalhousie University, Halifax, Nova Scotia, Canada), visi-
ble blue light with a wavelength of 405 nm was derived from a diode-pumped
laser CRL series (Laser 2000, Munich) operating in continuous wave (cw)
mode with an output power of 25 mW and a multimode coherence length of
more than 5 m. The laser beam passed a system of lenses, mirror, pinholes
and beam expander as shown in Figure 3.1 in order to obtain an optimally
cleaned and shaped beam before finally being focused onto the final 500 nm
pinhole (National Apertures, USA) by an objective (Edmund Optics, USA;
10x, $NA = 0.25$). The sample was mounted on an xyz-stage between the
pinhole and the detector, and the magnification was given by the via high
precision manipulators (Melles Griot, USA) adjustable pinhole-sample dis-
tance. A high-resolution camera, model CSB4000CL (Toshiba-Teli, Japan)
with a CMOS image sensor (2048x2048 pixels of 6x6 $µm^2$) was used to record
the hologram. During the measurements the exposure time was adjusted for
a maximum contrast without saturating the CMOS chip, typically several
hundred milliseconds for the presented images.
In the similar setup (not shown) for the described UV experiment, UV-
light with a wavelength of 355 nm was produced by a Nd:YAG laser system,
model YG671C (Continuum, USA) by frequency tripling the fundamental
wavelength of 1064 nm. The output power of the laser was 5 mW with a
pulse length of 8 ns and a repetition rate of 10 Hz. The laser light was fo-
cused by an UV objective (Zeiss Fluar; 20x, $NA = 0.75$ UV) onto pinholes,
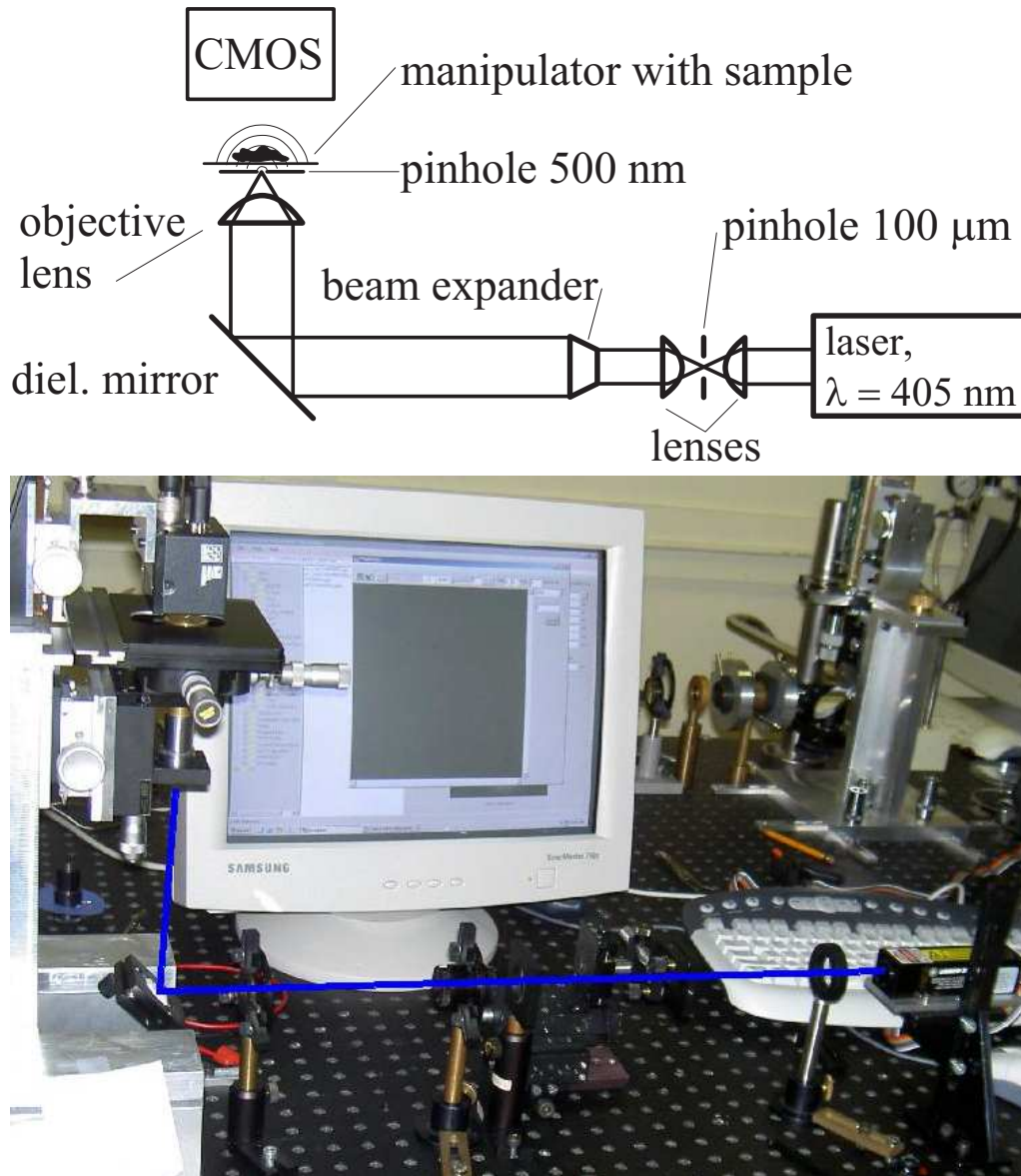
Figure 3.1: Implemented setup for high numerical aperture recordings by DIHM at Dalhousie University

laser-drilled into molybdenum foils on stainless steel backings with an initial diameter of 0.5 µm which changed, however, during the measurement, to as much as 0.8 to 1.5 µm. The holograms were recorded by a UV detector camera, model AT200 (Photometrics, USA) equipped with a SI003 Chip (1024x1024 pixels on an area of 24x24 mm^2). The exposure time in these

experiments was typically several seconds.

The following protocol has been carried out for all recorded and reconstructed images [27]:

1. Positioning of the pinhole. The pinhole is glued to a manipulator and needs to be adjusted for maximum illumination and thus minimum acquisition times.

2. Inserting and adjusting the sample into the optical path via manipulator: The focus loop function of the data acquisition program enables precise control over desired sample section and magnification.

3. Digital recording of the sample hologram: The intensity matrix I_{nm} is recorded on the camera chip, n and m specifying the chip pixels.

4. Removing of the object from the beam path and recording of the intensity matrix $I_{nm}^{(0)}$ of the illumination after the pinhole.

5. Numerical compilation of the contrast image $\tilde{I}_{nm}$ and correcting of potential intensity variations of the reference wave $I_{nm}^{(0)}$ [27]:

$$\tilde{I}_{nm} = \frac{I_{nm} - I_{nm}^{(0)}}{\sqrt{I_{nm}^{(0)}}} \; . \tag{3.1}$$

3.2   Digital In-Line Holographic Experiments

3.2.1   Polystyrene Beads

The goal of this study was to demonstrate the performance of digital in-line holography using short laser wavelengths and high numerical apertures. In order to characterize the resolution, polystyrene beads with sizes between 356 nm and 1.1 µm in diameter were used and the imaging properties of single beads, bead dimers and bead clusters were studied. These well-defined shapes and small size variations were confirmed by SEM (Figure 3.2) prior to the experiments. The degree of dispersion on the surface was adjusted
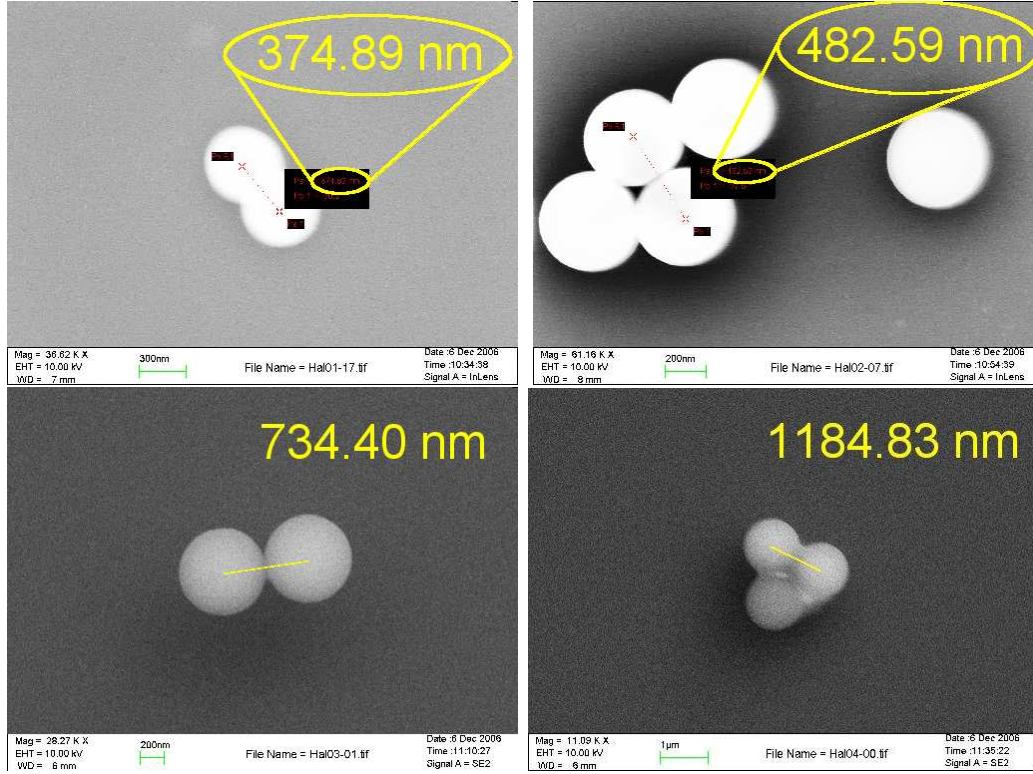
Figure 3.2: SEM images of polystyrene beads for size verification, magnifications 36620x (upper left), 61160x (upper right), 28270x (lower left), 11090x (lower right)

mainly by changing the angle under which the substrate was kept while drying. By this preparation procedure, monodisperse particles, as well as dimers and island-like aggregates consisting of a particle monolayer were obtained. Figure 3.3 shows the results for the imaging of monodisperse, individual 1.1 µm polystyrene beads. The hologram was recorded with the 405 nm laser setup described above (see Section 3.1). The numerical aperture of the geometry was 0.414, thus leading to a theoretical lateral resolution of 490 nm. The reconstruction at a distance of 123 µm away from the pinhole is given in the center panel, showing four beads. The intensity profile through the particle as indicated by the arrow is shown on the right-hand side. The FWHM is 1.1 µm, thus being in very good agreement with the nominal particle size. The fact that no additional broadening is observed is not surprising as the size of the particle is larger than the theoretical reso-

Hologram,	Reconstruction,	Line profile through the
$\lambda = 405$ nm, $NA = 0.414$	$d_{rec} = 123$ µm	bead indicated by an
		arrow
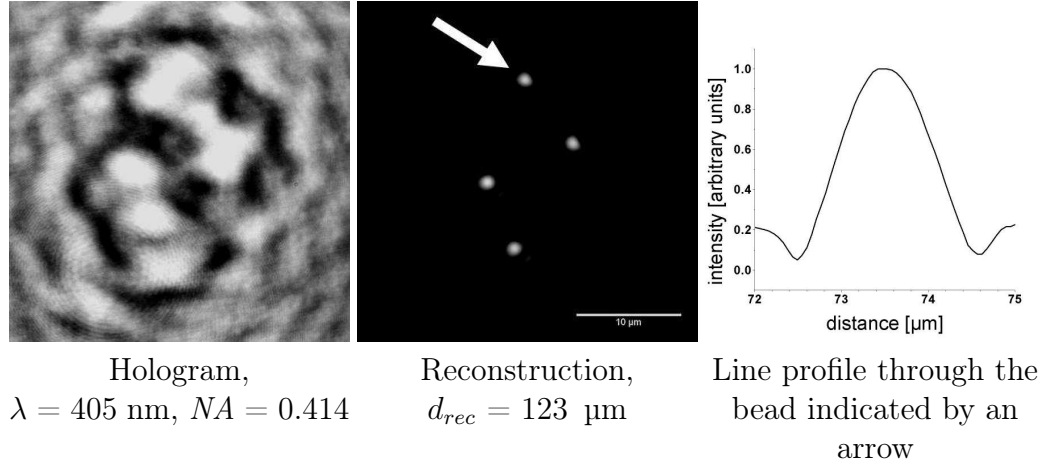
Figure 3.3: 1.1 µm polystyrene beads deposited on a glass substrate

lution of 490 nm. According to the Rayleigh criterion, two point sources are

| 0% broadening | 2.5% broadening | 5% broadening | 7.5% broadening |

| 10% broadening | 12.5% broadening | 15% broadening | 17.5% broadening |
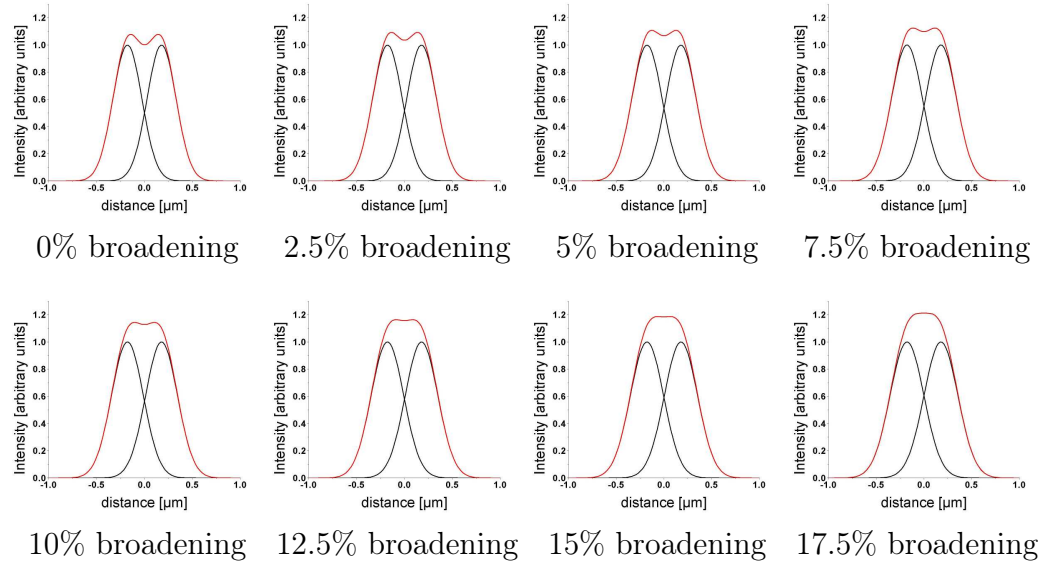
Figure 3.4: Simulation of bead dimers for the example of 356 nm beads

just resolved if the intensity maximum of the one coincides with the first intensity minimum of the other [7]. The reconstruction image of two adjacent beads was simulated by modeling the beads with Gaussian functions and the superposition of these curves examined. Figure 3.4 shows the situation for a series of broadening percentages. The initially apparent minimum in

the center of the superposition curve decreases with increasing broadening of the Gauss functions. Two maxima are barely visible up to a broadening of 10% before turning into one single maximum. Of course, using a Gaussian

| Hologram, | Reconstruction, | Line profile through the |
| $\lambda = 405$ nm, $NA = 0.564$ | $d_{rec} = 46.3$ µm | bead dimer indicated by an arrow |
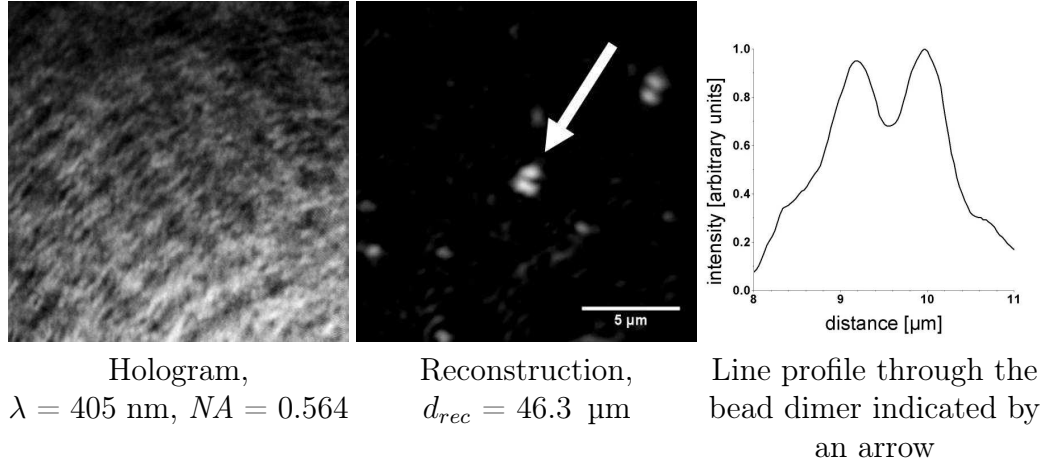
Figure 3.5: 0.500 µm polystyrene particles deposited on a glass substrate

function to model two adjacent beads is a rough approximation as neither the point source is taken into account nor the bead scattering effects. For an accurate simulation the object function has to be convoluted with a so-called point-spread function that describes the response of an imaging system to a point object. For a circular aperture the point spread function would be the Airy distribution (see Figure 1.6). The general tendency, however, becomes clear even from this crude model. Thus, in order to test the resolution, intensity distributions through bead dimers were analyzed. Figure 3.5 shows the result obtained for polystyrene beads with a nominal size of 500 nm on a glass slide. The hologram was recorded with a numerical aperture of 0.564, leading to a theoretical lateral resolution of 359 nm. A reconstruction of the hologram at a distance of 46.3 µm away from the pinhole is shown in the center panel of Figure 3.5. The arrow indicates a bead dimer whose intensity profile along the direction of the arrow is displayed in the panel on the very right. Both particles can clearly be distinguished from each other as a minimum between the two particle positions is resolved. The general appearance of the beads is slightly smeared out which is due to the fact that the bead size

is approaching the theoretical resolution. The smallest beads investigated in

Hologram,	Reconstruction,	Line profile through the
$\lambda = 405$ nm, $NA = 0.564$	$d_{rec} = 44.1$ µm	bead dimer indicated by an arrow
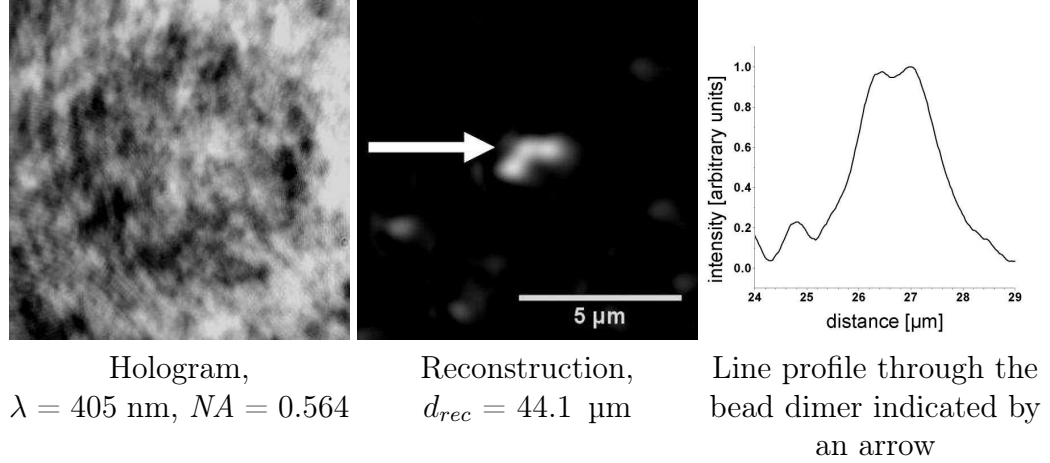
Figure 3.6: 0.356 µm polystyrene particles deposited on a glass substrate

this study were 356 nm polystyrene beads fixed on a glass slide. The results
are shown in Figure 3.6. The numerical aperture used to record the holo-
gram on the left was 0.564, which leads to a theoretical lateral resolution of
359 nm. A reconstruction at a distance of 44.1 µm away from the pinhole is
depicted in the middle panel. The arrow indicates again a bead dimer whose
intensity profile (shown on the right) was examined in the direction of the
arrow. In accordance to the results observed with the 500 nm beads, again
a dip in between the two maxima can be observed, thus indicating that even
these small particles very close to the resolution limit of the setup can be
resolved. The broadening of the beads is now becoming obvious, which is not
surprising as their diameter is just at the limit of the theoretical resolution
and also smaller than the wavelength used for imaging. These experiments
yield to our knowledge the highest resolution ever achieved with a digital
in-line holographic microscopy as the so far published highest resolution was
1.09 µm [75]. As described above, the interference of scattered photons with
the undisturbed reference wave is the source of hologram formation. One
frequently raised question is how strongly the quality of a reconstruction is
affected when the reference wave is disturbed. Therefore a complex arrange-
ment of polystyrene particles as test object was used. The conventional light

Hologram,
$\lambda = 405$ nm, $NA = 0.488$

Reconstruction,
$d_{rec} = 290$ µm

Line profile
through the row of beads
indicated by an arrow

Transmission light microscopy image,
Olympus objective 100x,
$NA = 0.9$
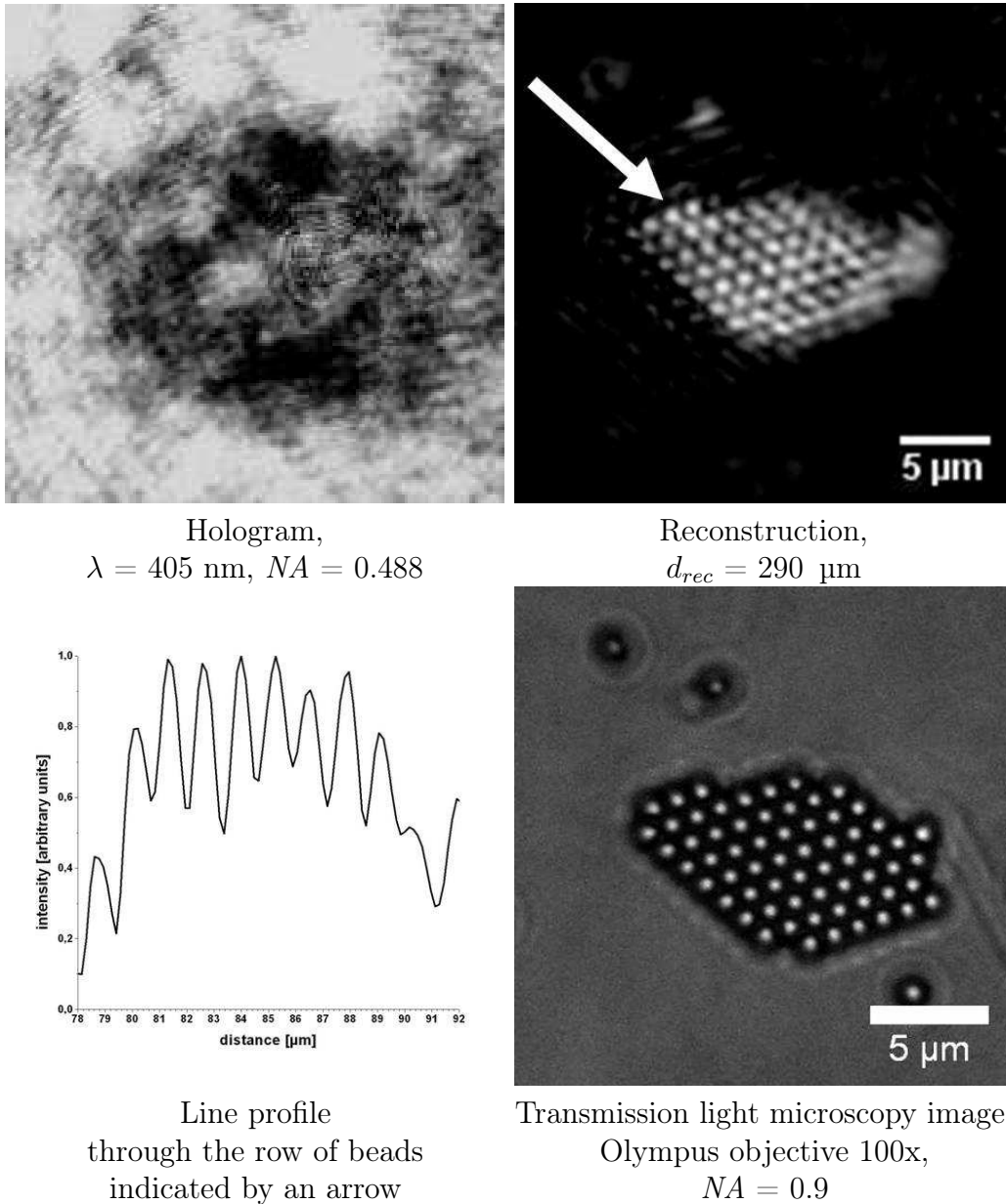
Figure 3.7: 1.1 µm polystyrene particles deposited on a glass substrate

microscopic image in Figure 3.7 shows multiple beads with a size of 1.1 µm in a self-organized arrangement on a glass surface. As the patch with the beads has only small areas where light can pass through without being scattered, nearly no reference wave can pass undisturbed. Nonetheless, the correspond-

ing hologram in the top left panel of Figure 3.7 shows still well-resolved interference fringes. The numerical aperture was 0.488 yielding a theoretical lateral resolution of 415 nm which should be sufficient to resolve the particles. In the top right panel one can see the reconstructed hologram at a reconstruction distance of 290 µm. Quite remarkable are the clearly visible internal structures of this rather large cluster. The resolution of the internal structures is as good as the one of the particles located at the border of the object. The arrow shows the direction of the line scan shown on the right through the indicated row of beads. Beads in this cluster are well resolved as the obvious minima in the profile reveal. For comparison, images of the cluster were also obtained with a compound microscope (Zeiss Axioplan 2, Olympus Objective 100x, $NA = 0.9$), shown on the bottom right-hand side. The qualitative comparison between the hologram and the microscopy image shows that DIHM is able to provide microscopic images with a quality comparable to that of commercial optical microscopes. To approach the resolution of smaller particles, 752 nm beads in a cluster were investigated, and the results are presented in Figure 3.8. The hologram on the top left was taken with a numerical aperture of 0.564. The geometry leads to a theoretical lateral resolution of 359 nm. The top right panel shows the reconstructed image at a reconstruction distance from the pinhole of 64.2 µm. For comparison, a conventional microscopy image is shown on the bottom right. The line scan through one row of beads indicated by the arrow shows clearly defined minima which further states the feasibility to resolve 752 nm beads inside a large cluster. Besides using immersion techniques as described in Section 3.3, it is also straightforward to enhance the imaging quality by decreasing the wavelength beyond 405 nm. In a first experiment with UV light that was presented previously [74] isolated and small clusters of 2.9 µm latex beads immobilized on a glass slide were examined. The hologram is shown in the top left panel of Figure 3.9 and was recorded with a numerical aperture of 0.33 which should theoretically lead to a spatial resolution of 660 nm. The top right panel shows the reconstructed image at a distance of 350 µm from the pinhole. Beads in the small cluster are clearly resolved, and a line profile through two touching beads (not shown) confirms this. Also a line profile

Hologram,
$\lambda = 405$ nm, $NA = 0.564$

Reconstruction,
$d_{rec} = 64.2$ µm

Line profile
through the row of beads
indicated by an arrow

Transmission light microscopy image,
Olympus objective 100x,
$NA = 0.9$
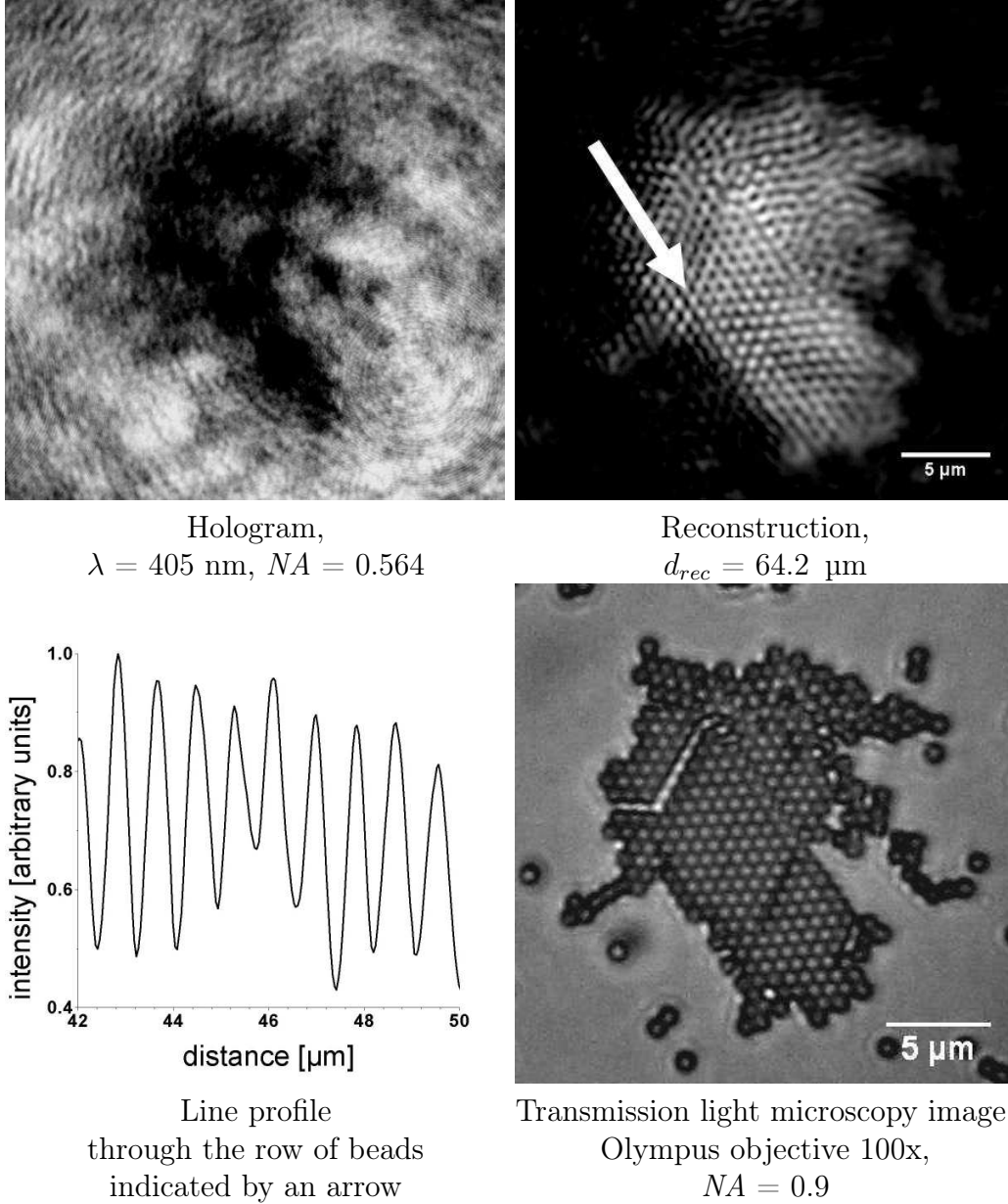
Figure 3.8: 0.752 µm polystyrene particles deposited on a glass substrate

through a single bead confirms its nominal size as the measured FWHM is 2.9 µm. This is not surprising as the size of the beads is much larger than both the theoretical resolution for this experiment and the size of the pinhole (<1.5 µm). For comparison a phase contrast image of the particle sample

<div align="center">
Hologram,
$\lambda = 355$ nm, $NA = 0.33$
</div>

<div align="center">
Reconstruction,
$d_{rec} = 350$ µm
</div>

<div align="center">
Line profile
through the row of beads
indicated by an arrow
</div>

<div align="center">
Phase contrast light microscopy
image,
Zeiss A-Plan 50x,
$NA = 0.8$
</div>
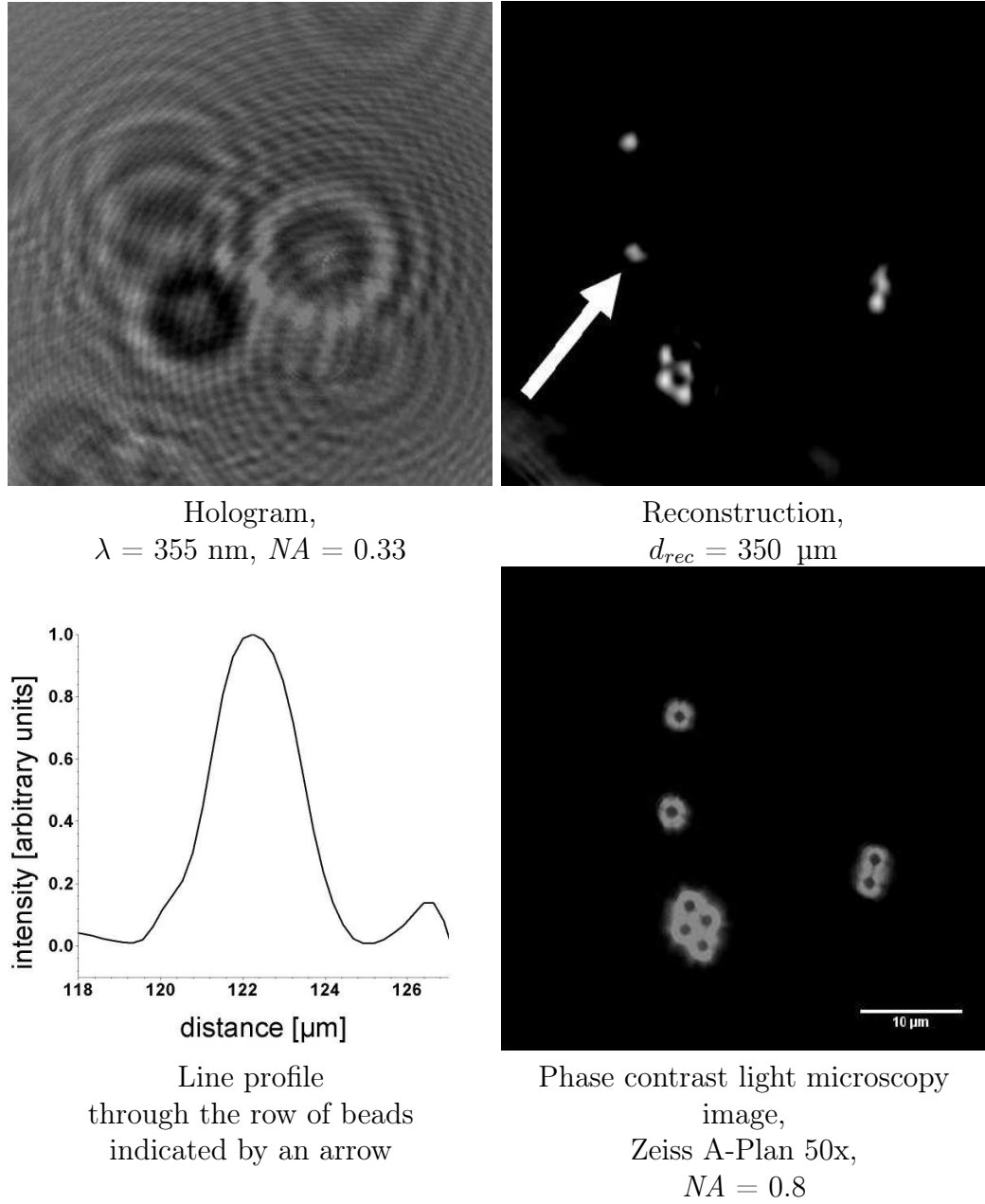
Figure 3.9: 2.9 µm polystyrene beads deposited on a glass slide

is shown on the bottom right. Using a pulsed laser with a nanosecond pulse length makes the situation more difficult compared to cw-mode lasers as used above. Due to the low repetition rate of 10 Hz, the pulse intensities need to be some hundred µJ in order to become able to record images with expo-

sure times of seconds. The high pulse energy and the pulse-to-pulse intensity variations can in some cases alter the pinholes, affecting the imaging quality. Considering the rapid developments on the laser market, it is very likely that UV holography becomes possible and affordable with cw-mode or high repetition rate lasers in the near future. Especially with the availability of the femtosecond X-ray free-electron laser (XFEL) currently under construction for instance in Hamburg, substantial improvements in terms of coherence, pulse length and photon flux will be achieved. It would then be possible, for instance, to study protein resonances by extending holography into the UV range. Seen in the light of the availability and price of full UV optics digital in-line holography will be a highly useful tool for selective imaging in this wavelength range in the future.

In general, the use of a pulsed laser for holography has two sides: On the one hand, short pulses are advantageous as problems of vibrations and air currents are largely eliminated [2]. Even moving objects can be made to appear at rest when a hologram is produced with short pulses as long as the object does not move more than $1/10$ of a wavelength during the duration of one pulse [4]. This is due to the requirements for spatial coherence between the interfering waves - their optical path difference should not exceed $1/10$ of a wavelength during exposure or a movement of the fringes and reduced contrast in the hologram will result [4]. One the other hand, temporal coherence is correlated with the spectral bandwidth of the radiation over [9]

$$\Delta l \approx \frac{c_0}{\Delta \nu},\qquad(3.2)$$

where Δl is the coherence length, c_0 the speed of light in vacuum, and $\Delta \nu$ the spectral bandwidth. The pulse duration in turn can be related to the bandwidth via Heisenberg uncertainty relation:

$$\Delta E \Delta t \geq \frac{\hbar}{2}.\qquad(3.3)$$

Thus, pulse duration and bandwidth are inversely proportional to each other which in turn leads to a decreasing coherence length with decreasing pulse

duration. The applicability of UV illumination for holography with nanosecond pulses presents a highly important preliminary test for the envisaged picosecond VUV experiments at BESSY II that will be described in Chapter 4.

3.2.2 Fibroblast Cells

Hologram, $\lambda = 405$ nm, $NA = 0.524$	Reconstruction, $d_{rec} = 272$ µm	Microscopy image, Zeiss A-Plan objective 10x, $NA = 0.25$
Hologram, $\lambda = 405$ nm, $NA = 0.524$	Reconstruction, $d_{rec} = 260$ µm	Microscopy image, Zeiss A-Plan objective 10x, $NA = 0.25$
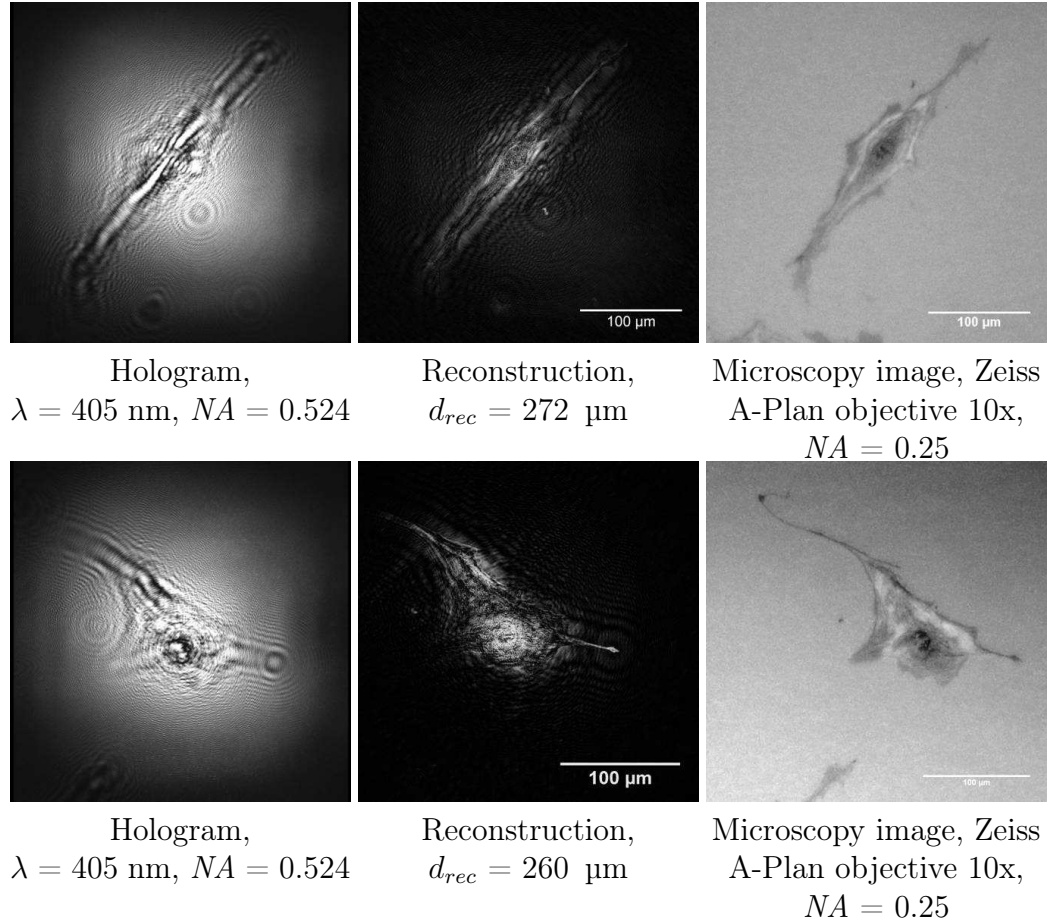
Figure 3.10: Fixed and critical-point-dried REF52 wt cells on a silicon nitride window

The applicability of DIHM to biology has been presented previously including the motion of bacteria in single cells [29,30,33]. As one motivation of extending DIHM to shorter wavelengths is the investigation of biological processes in cells, digital in-line holography was used to image REF52 wt cells. The

conventional microscopy images in Figure 3.10 show critical-point-dried fibroblast cells in transmission mode, and the insets in Figure 3.11 present a magnification of the cell nucleus area and of one filament in the periphery of the cell. The panels on the left column of Figure 3.10 show the holograms of the cells, and the center column the reconstruction planes with foci close to the glass slide. Both holograms show again well-resolved interference fringes that are crucial for good edge sharpness in the reconstruction. The holograms were recorded with a numerical aperture of 0.524, leading to a theoretical resolution of 386 nm. The reconstructions reveal that the borders of the large objects appear somewhat distorted which can be explained by the fact that these delicate features are superposed by interference fringes. These fringes are caused by the predominance of the object wave compared to the reference wave due to the close proximity of the sample to the source. Additionally, the large extension of the cells violate the Fraunhofer criterion (see Equation 1.7) as they measure approximately 200 µm, and for the reconstruction distance of $d_{rec} = 272$ µm and the employed wavelength of $\lambda = 405$ nm the criterion asks for sample dimensions not exceeding $a = 10.5$ µm. On the contrary, internal features within the cells are resolved. The slightly larger amount of internal material seems to provide enough phase contrast to superpose the interference fringes yet leave enough space for the reference photons to pass through the cell and form a hologram. Therefore, features within the cell like the nucleus become reconstructible. The insets show a comparison of optical microscopy and holography at different parts of the samples. For both cell nuclei a high sensitivity of the nuclear envelope can be observed while the contrast for the nucleoli is rather weak. The insets with filaments located in the periphery of the cells in both cases show clearly resolved features. The possibility to reconstruct features within a cell combined with the intrinsic three-dimensionality suggest applications in biophysics like the monitoring of changes within cells during the application of mechanical stress or the direct, three-dimensional tracking of transport phenomena within cells.
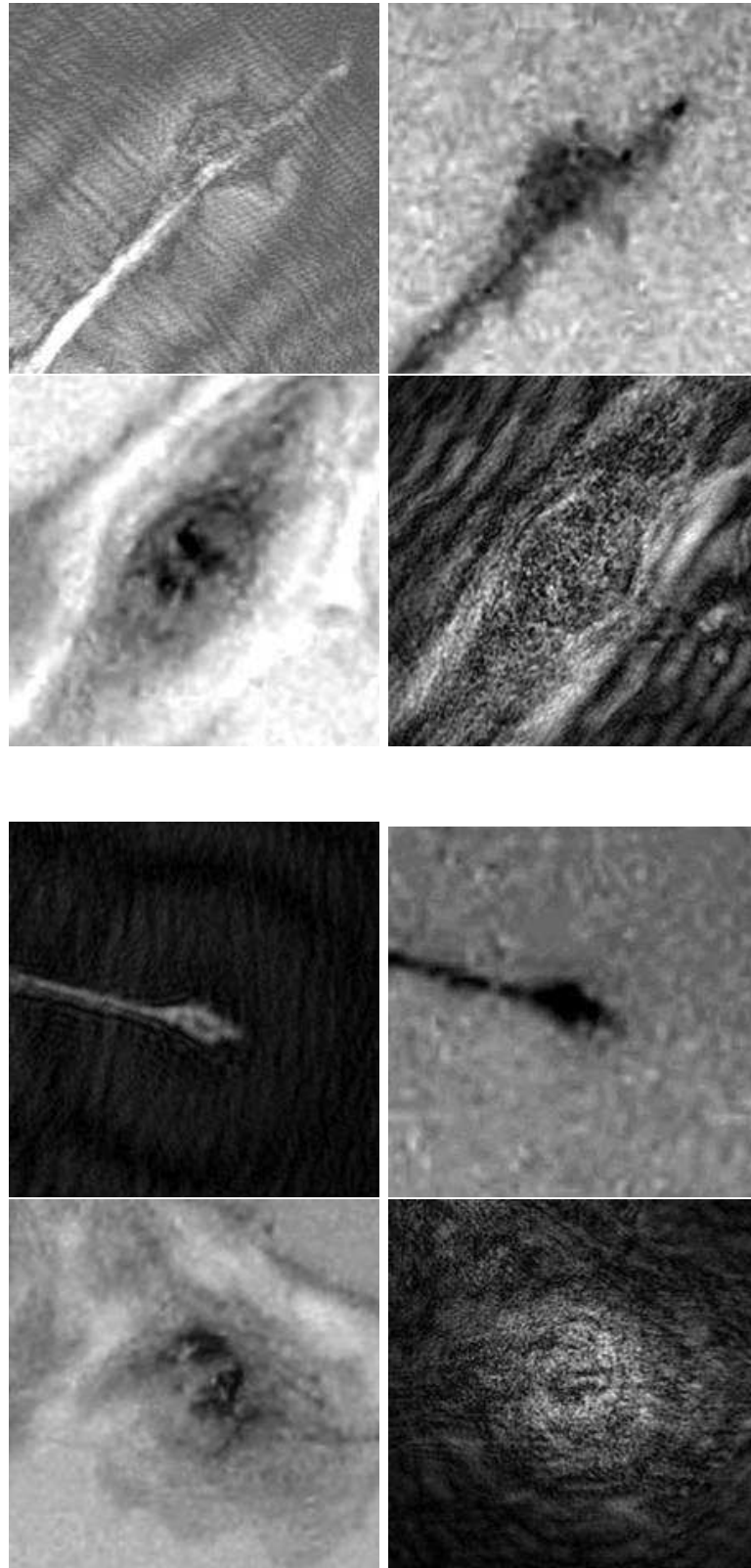
Figure 3.11: Magnified filament and nucleus cutouts of the REF52 wt cells in Figure 3.10. *Left column:* Microscopy images, *Right column:* Reconstructions

3.3   Immersion Digital In-Line Holography

As described above, the performance of DIHM can greatly be enhanced by
making use of oil immersion techniques [26]. Here, a chamber filled with
immersion oil with a refractive index $n_{oil} = 1.515$ is placed between the
sample and the detector. As a result, the achievable resolution significantly
increases as it is dependent on the numerical aperture $\delta_{lateral}^{theo} \geq \frac{\lambda}{2\,NA}$ (see
Equation 1.25) of the system which in turn is dependent on the refractive
index of the surrounding medium: $NA = n\sin\vartheta$. Figure 3.12 shows the
influence of the immersion oil on an extended cluster consisting of the same
752 nm particles as imaged in Figure 3.8. The numerical aperture used for
this experiment was 0.414, thus slightly smaller than in the above-described
experiment with a theoretical resolution of 489 nm. The reconstruction at a
pinhole-sample distance of 59.9 µm is shown on the top left. The same spot
was then recorded with an oil chamber of $H = 10$ mm height in between the
sample and the detector. As the space between sample and detector could
not entirely be filled with oil, it is necessary to calculate an effective refractive
index $n_{eff} = (L - H + nH)/L$, with L being the distance between pinhole
and screen and H the height of the chamber [26]. Thus, one obtains a value
of n_{eff} of 1.38 which leads to an effective numerical aperture of 0.572 and
thus a theoretical lateral resolution of 354 nm. The increase in resolution by
28% can be seen by the improved sharpness and resolution of the particles
of the top right panel compared to the top left. A conventional microscopy
image is again shown for comparison on the bottom right. Through the
same row of beads indicated by the arrows, line profiles are shown. The
visual impression is confirmed by the profiles as the minima in the curve
representing the oil immersion holography are much more pronounced than
the ones in the curve without the oil. The previous observation that internal
structures in the clusters can be resolved can again be confirmed, indicating
that the disturbance of the reference wave does not affect the quality of
imaging.
The smallest resolved self-assembled polystyrene beads so far published had
a diameter of 1.09 µm [75], thus the successful resolution of 752 nm sized

Reconstruction,
$d_{rec} = 59.9$ µm

Reconstruction,
$d_{rec} = 59.9$ µm,
oil column $H = 10$ mm

Line profile
through the row of beads
indicated by an arrow

Transmission light microscopy image,
Olympus objective 100x,
$NA = 0.9$
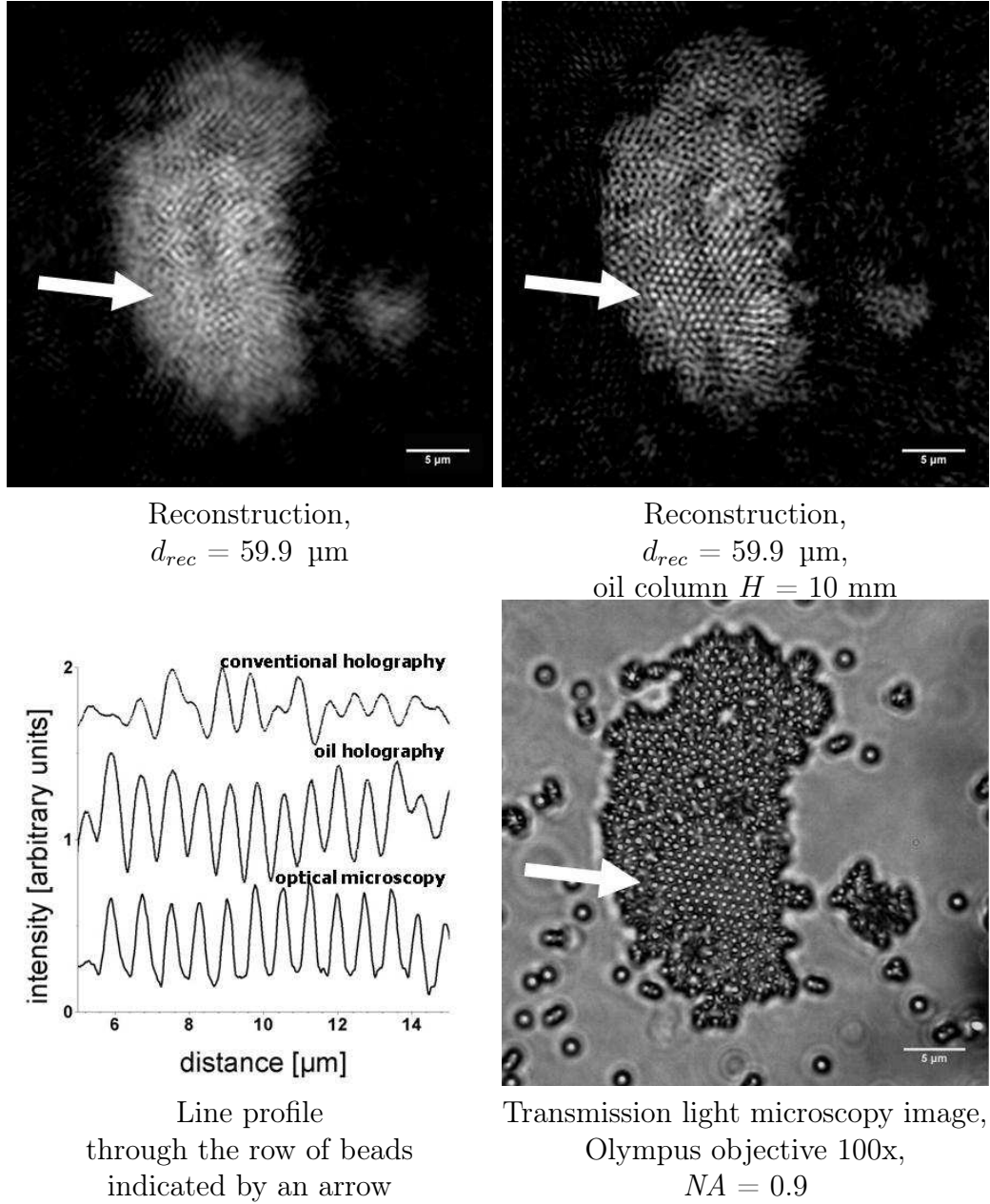
Figure 3.12: 0.752 µm polystyrene particles deposited on a glass substrate. Holograms recorded with $NA = 0.414$ (top left) and $NA_{eff} = 0.572$ (top right).

particles presents to our knowledge the best resolution of particles in a large cluster ever achieved by DIHM with visible light.

3.4   Conclusion and Outlook

DIHM was performed with visible light of the wavelength of 405 nm in order to resolve single polystyrene beads, bead dimers and bead clusters down to a nominal bead size as small as 356 nm. Even though FWHM measurements in intensity profiles show broadened appearances, pronounced minima are visible, clearly fulfilling the resolution criterion. Thus, it can be concluded that 356 nm resolution is possible with visible laser light. Extended arrangements of 1.1 µm and 752 nm beads were tested for their ability to be resolved, and even inner parts in extended particle arrangements where the reference wave is disturbed through the shear size of the cluster were reconstructible. Immersion DIHM as described in [26] was used to increase the numerical aperture and thus the resolution. The reconstructed images of 752 nm polystyrene beads in a cluster with and without an oil chamber of higher refractive index were compared and an increase of resolution of 28% was shown. Polystyrene bead arrangements were used to test the imaging properties of the setup. For single beads, well-resolved images were obtained. Biological samples like cells are suitable objects to be investigated by DIHM which suggests applications in biophysics.

Furthermore, the feasibility of DIHM with pulsed nanosecond UV radiation was demonstrated which supplied important knowledge for the experiments with picosecond VUV radiation that will be described in the following chapter and also for the anticipated experiments with femtosecond pulses derived from an XFEL facility. As an outlook, different protein resonances in the deep UV region could in the future selectively be used for holographic imaging in order to obtain label-free protein specific contrast with much higher quality than UV microscopes can achieve. As another future goal the implementation of an immersion setup with UV light seems highly recommendable as the numerical aperture could be increased to 0.6 even with the present setup,

leading to a theoretical resolution of 296 nm and below.

Chapter 4

Digital In-Line Holography with Synchrotron Light

The achievable resolution in digital in-line holographic microscopy is next to the numerical aperture mainly dependent on the wavelength of the used light:

$$\delta_{lateral}^{theo} \geq \frac{\lambda}{2NA}.$$

Thus, it is straightforward to decrease the wavelength used for coherent illumination in order to improve the efficiency of the technique. A first step towards this was the extension into the UV range that was described for nanosecond pulses in the previous chapter. In this chapter, a further decrease of the wavelength for DIHM into the VUV range is pursued.

Via X-ray fluorescence holography Angstrom resolution has been achieved to determine atomic positions in ordered solids [76–78]. In-line holograms have been recorded using a selenium X-ray laser at a wavelength of 21 nm with a resolution of 5 µm [45]. Soft X-rays, especially in the water window (see Figure 1.19) between 2 and 5 nm, are known to allow high-resolution microscopy imaging of biological specimens [79, 80]. X-rays are produced by accelerating electrons, e.g. in a synchrotron. The *Berliner Elektronenspeicherring-Gesellschaft für Synchrotronstrahlung* (BESSY) operates a 3rd generation

synchrotron radiation facility, the storage ring BESSY II, whose beamlines provide ultrabright photon beams from the terahertz region to hard X-rays [81]. As the electrons move though the storage ring in so-called bunches, the obtainable radiation is pulsed. The pulse duration is 18 ps and the distance 2 ns [9] yielding a repetition rate of approximately 500 MHz. An especially useful property of synchrotrons is their tunable wavelength that can be exploited for instance at experiments with energies around the carbon absorption edge in order to distinguish particles with different intrinsic material contrast [65].

4.1   Experimental Setup
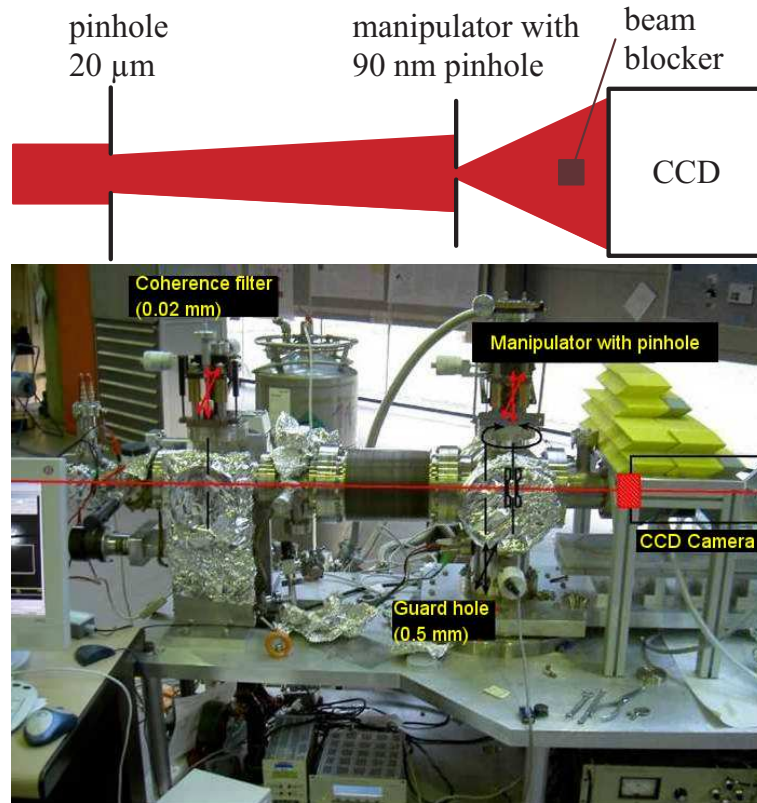
Figure 4.1: Speckle chamber at the beamline UE56-1/SGM

During the first beamtime in 2004 experiments were carried out at the speckle

chamber originally designed for magnetic Fourier holography [20] at the undulator beamline UE56-1/SGM (Figure 4.1). Soft X-rays were derived from an undulator source in combination with a spherical grating monochromator that determined the coherence length Δl. The coherence length of the picosecond pulsed beam for example for a photon energy of 775 eV or a wavelength of 1.6 nm is $\Delta l = 1.6$ µm [20]. The beam then impinged on an aperture of diameter $D = 20$ µm acting as a spatial coherence filter before coherently illuminating a pinhole of 90 nm diameter on a high precision manipulator at a distance of $z = 723$ mm behind the coherence filter. The spatial coherence length is thus determined to $\Delta l_s = 9.1$ µm [20] for the wavelength of 1.6 nm. Images were recorded with a CCD camera (Roper Scientific, PI-SX-2048, Marconi CCD42-40 chip, 2048 x 2048 pixels of 13.5 x 13.5 µm^2) at a distance of 315 mm from the pinhole. The whole setup is placed inside an ultra high vacuum chamber to avoid air-molecule scattering and protected against disturbances by cosmic rays through lead blocks on top of the CCD camera.

4.2 Results and Discussion

The goal of the first beamtime was to probe the possibility of using coherent X-rays for point source holography. This cannot be taken for granted as several problems may arise due to the high photon energy. Manipulation of X-rays is only successful through reflection, diffraction and interference effects [9], for example via zone plates. Thus, the applicability of pinholes to diffract X-rays had to be tested in general. The attenuation of X-rays by a material is given by the Beer-Lambert law [9]:

$$I_1 = I_0 \exp(-\alpha d) \tag{4.1}$$

where I_1 and I_0 are the intensities of the incident light and of the light after passing through the material, α is absorption coefficient of the material and d its thickness. All elements in the beam path need to be selected according

to this law in order to serve their purpose when interacting with the X-rays. Pinholes need to be placed within opaque enough backings in order to prevent the direct beam from passing through. Increased thickness of the material, however, complicates the fabrication of small pinholes necessary to have a diffraction effect in the first place and additionally one large enough to form a spherical wave necessary for the exploitation of the method as microscopy technique. Samples also need to provide enough contrast to produce an intense enough secondary wavefront. Sample substrates on the other hand, need to be transparent enough to let the reference wave pass undisturbed. Only then can a reconstructible hologram be formed by interference with the scattered wave. Another problem is the limited coherent photon flux available from an incoherent source which scales as $1/\lambda^3$ for the number of photons available [68]. As the pulses are even shorter than for the previously used nanosecond UV radiation, the coherence length is even shorter as well, namely 1.6 µm for a wavelength of 1.6 nm even after a monochromator has been applied [20]. Additionally, the necessity to perform the whole experiment in a vacuum chamber dictates certain boundary conditions, e.g. the large pinhole-detector distance that decreases the numerical aperture and thus the achievable resolution.

A mandatory requirement for holographic microscopy is the formation of a divergent coherent wavefront. This results in an Airy pattern (see Section 2.1) at the screen. The 90 nm pinholes supposed to provide divergent illumination were FIB-milled by C. Rettner (IBM Corporation, Almaden Research Center, Menlo Park, USA) into 220 nm thick gold films on 150 x 150 µm^2 silicon nitride membranes of 30 nm thickness, similar to the pinhole shown in Figure 4.2. The latter of approximately the same diameter was FIB-milled by W. Schlotter (Stanford Linear Accelerator Center, Menlo Park, USA).

During the measurement with the above-described setup it became clear that the gold film unfortunately did not have the necessary opacity to prevent the direct beam from being transmitted even at the lowest used photon energy of 280 eV. In order to find out whether a signal emitted by the pinhole could be found somewhere in the overall transmission, the source was recorded for 50 min (Figure 4.3). To prevent the detector from being satu-
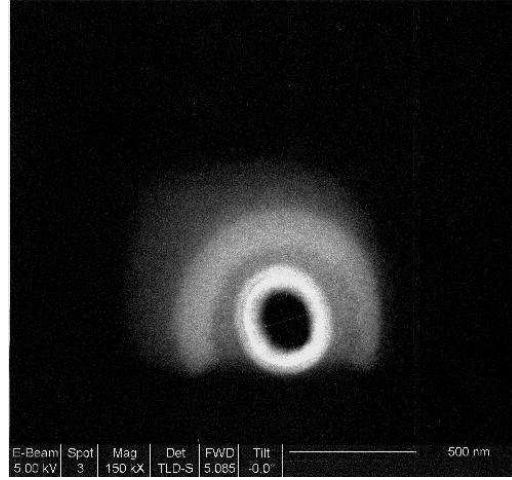
Figure 4.2: SEM image of a pinhole fabricated by W. Schlotter for experiments at BESSY II

rated, a beam blocker was introduced in the beam path directly in front of the detector as can be seen by the horizontal dark bar in the image. As described in Section 2.1 the illumination provided by a circular aperture forms an Airy pattern on the screen. The size of the Airy disc is dependent on the wavelength (see Equation 1.16). The source was recorded at four different photon energies: 280, 403, 644, and 775 eV corresponding to wavelengths of 4.43, 3.08, 1.93, and 1.60 nm, respectively. Background images were subtracted to eliminate dark noise of the CCD. The images were cropped to a square with the center of the light source as its center which resulted in an odd number of pixels. Then, the cropped images were analyzed by placing concentric rings with a width of 5 pixels around the center, and the counts within one ring were divided by the number of pixels within that ring. The counts per pixel depending on its distance to the center results in a radial distribution function (RDF) (Figure 4.4). While the raw image is dominated by the strong transmitted light coming through the gold film, the image's background shows a distinct pattern that might be explained by an Airy distribution. The curves for the lowest photon energies (280 eV) shows a distinct shoulder at a distance of about 500 pixels from the center which might indicate the outer part of the central Airy disc while the distributions of the higher photon energies (644 and 775 eV) show a second feature at 750 and
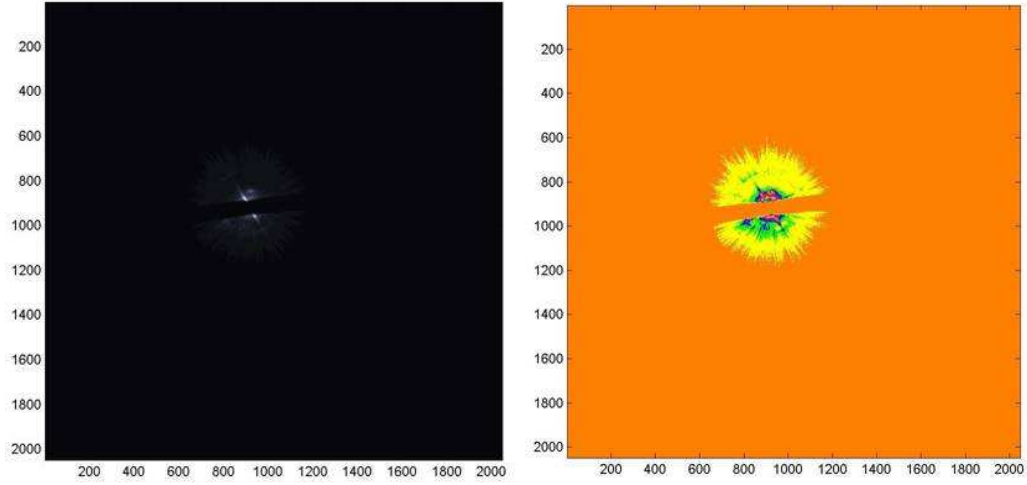
Figure 4.3: Source images of a 90 nm pinhole at 280 eV or $\lambda = 4.43$ nm
as recorded (left) and pseudocolored (right) to show all features
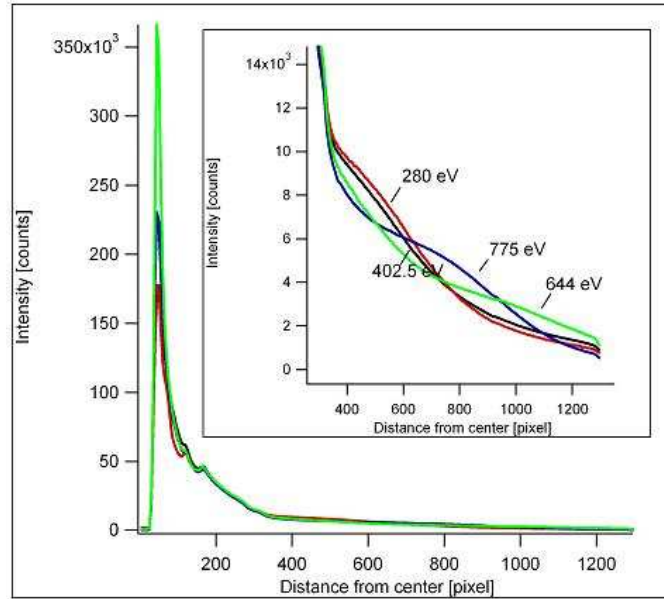
Figure 4.4: RDFs of the source images for different photon energies

1100 pixels from the center, respectively. These features might arise from the
presence of the second Airy ring. The general trend of decreasing disc radii
with increasing photon energies seems also reasonable.   Figure 4.5 shows the
same curves separated from each other through an offset (solid lines) and the
calculated Airy patterns (dotted lines) (see Equation 1.14) for the different
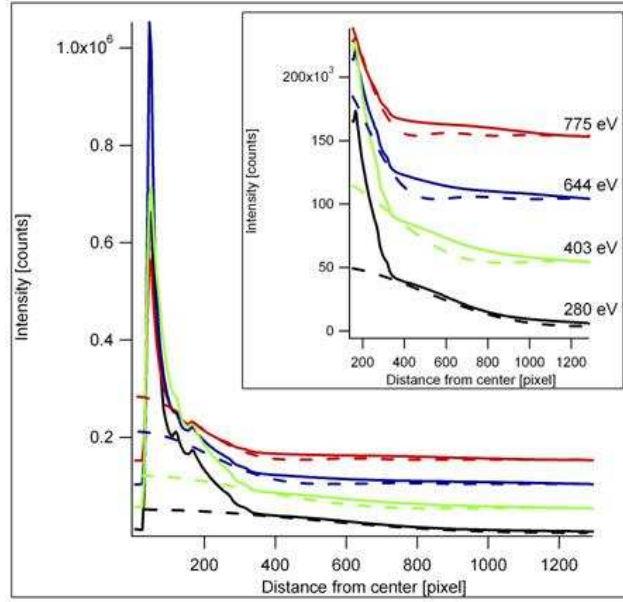
Figure 4.5: RDFs and estimated Airy profiles for a 90 nm pinhole

wavelengths and a pinhole diameter of 90 nm. Experimental and calculated curves are in very good agreement, indicating that an Airy pattern is indeed hidden in the background. The most important fact is that the photon energy of 280 eV is sufficient to produce a wavefront that is nearly exclusively consisting of the Airy disc as can be seen from the almost identical calculated and experimental curves in Figure 4.5. This energy corresponds to the carbon edge (see Figure 1.19), and the natural phase contrast of biological samples should be sufficient to obtain a reconstructible in-line hologram.

A second question to be solved was whether the sample backings consisting of 50 nm thick silicon nitride windows (1 x 1 mm^2 membranes on 200 µm thick 5 x 5 mm^2 supports) were transparent enough for an undisturbed transmission of the reference wave.

In Figure 4.6 the first measurement with a sample between pinhole and detector is shown. The left-hand side shows the pseudocolored raw image recorded with a photon energy of 280 eV. On the right its RDF is compared to the one obtained previously at 280 eV without the presence of a sample. The basic shape of the curve stays the same, only the intensities for the curve obtained in the presence of the sample are a little lower which might be due
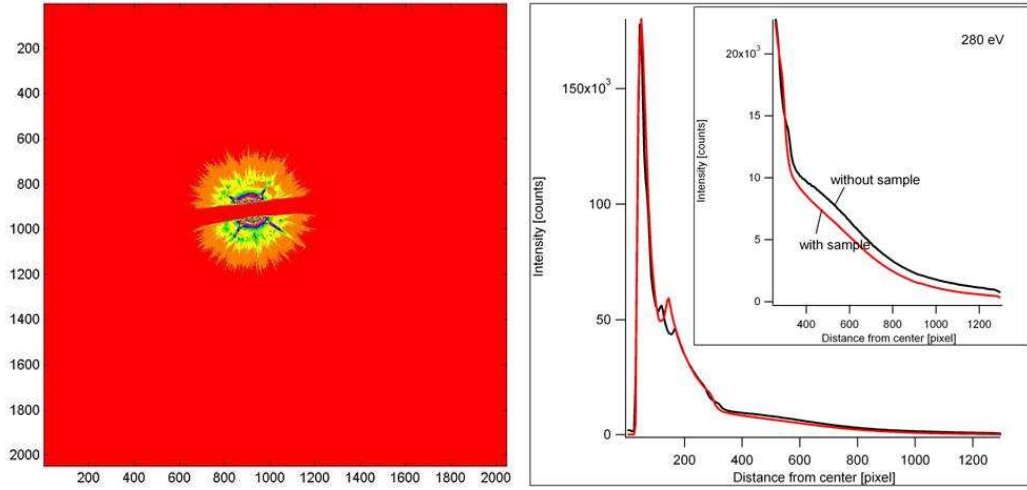
Figure 4.6: Results obtained with a sample present at a photon energy of 280 eV and a pinhole diameter of 90 nm

to the interaction with the material. The most important thing, however, is that the Airy disc is still present even if the wavefront has to pass through the sample membrane window which confirms the practicability of the planned sample mounting geometry.

Concluding, the first beamtime showed the general suitability of pinholes several orders of magnitude larger than the illuminating X-ray wavelength to produce an Airy pattern at the detector, a mandatory requirement in respect to the applicability of X-rays for in-line holography. However, the average count rate for a 50 min exposure is between 10^4 and 10^5 photons. In order to decrease acquisition times a better focusing of the beam seems advisable. Changing from beamline UE56-1/SGM (10^{11} photons per 1 x 1 mm^2) to a focused one, e.g. UE52/SGM (10^{11} photons per 18 x 18 µm^2) would increase the flux through the pinhole by a factor of more than 3000, thus enabling acquisition times of mere minutes with a reasonable count rate. Additionally, increasing the gold layer in order to ensure its opacity is mandatory for further experiments.

During the following beamtimes the above-described conclusions were used to realize X-ray digital in-line holographic (DIXH) microscopy. Among the improvements were the higher photon flux per area by making use of a fo-

Hologram,
$\lambda = 13.8$ nm, $NA = 0.012$

Reconstruction,
$d_{rec} = 4340$ µm

ROI of reconstructed
image above

ROI of SEM image,
magnification 673x

ROI of microscopy
image, Zeiss 40x
Neofluar objective,
$NA = 0.75$
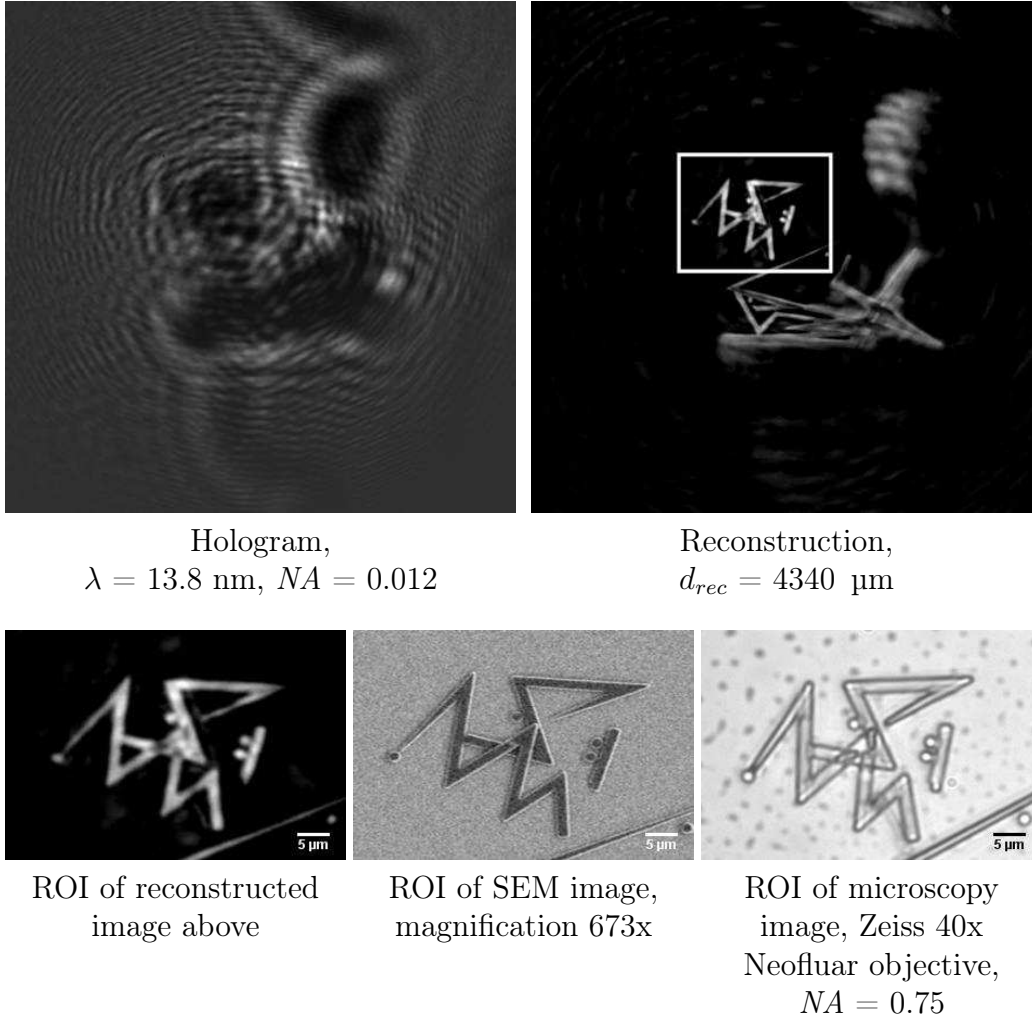
Figure 4.7: Lithography structures in SU8 photoresist on a silicon nitride membrane

cused beamline and opaque pinhole backings. Details of the experimental setup, measurements and results obtained during these beamtimes will be discussed in the forthcoming PhD thesis of R. Barth (Angewandte Physikalische Chemie, Universität Heidelberg) [65]. One task during the thesis at hand was to develop suitable test structures. At the used wavelength of 13.8 nm carbon-containing material has a high absorption coefficient (10^4 cm^2/g [82]), and in respect to the use of DIXM to investigate organic material, the carbon-based SU8 resist seems an excellent material. Structures can be designed at will by electron lithography. By adjusting the spin coat-

ing speed the resist layer was set to be $\approx$ 700 nm, a thickness comparable
to that of adherent cells, yet significantly below the theoretical depth res-
olution of the geometry, $\delta_{depth}^{theo} = 48$ µm. The structures were designed to
consist of a random distribution of dots and lines as described in detail in
Section 2.2.3. Some lines were tapered from 1.5 µm at the widest to below
the theoretical resolution limit. Figure 4.7 shows the imaging of these struc-
tures with radiation in the VUV spectral region. The hologram is shown
in the left panel, revealing well-resolved interference fringes mandatory for
satisfactory reconstruction. The right panel shows the reconstruction at a
distance of $d_{rec} = 4340$ µm, a magnified inset of which is presented in the
left image of the lower row. Artifacts on the right image rim are caused
by excess resist that has not been washed away in the developing step. The
SEM and optical microscopy pictures shown for comparison display an excel-
lent agreement with the reconstruction, proving that the photoresist with a
thickness of 700 nm provides enough material to ensure significant scattering
of VUV radiation. Furthermore, arrangements of particle mixtures showed
a resolution of around 1 µm [65, 68]. In addition, fibroblast cells could be
well resolved with remarkable contrast, suggesting potential applications in
solving biological problems. The latest experiments include images of im-
mobilized polystyrene and iron oxide particles prepared to probe possible
material specific contrast differences for organic and metal oxide materials
were distinguished based on their different X-ray absorption cross-sections
in the vicinity of the carbon absorption edge with submicrometer resolution.
For resolution characterization line cuts through different parts of the struc-
ture have been made (Figure 4.8). The first cut was made through a line
that was designed to be 1 µm but turned out to be 1.5 µm as SEM mea-
surements revealed. The FWHM of a Gaussian curve that was fitted into
the perpendicular to the line yields 1.640 µm, thus in very good agreement
with the SEM result. The same is confirmed with the line cut 6 through
two dots with a designed diameter of 1 µm. Their FWHM yields 1.665 and
1.708 µm. The lines 2 to 5 were put through a tapered line, and the FWHM
confirm a decreasing trend. Line cut 7 was taken through the thinnest line
discernible in the reconstruction image, and it yields a FWHM of 0.990 µm,
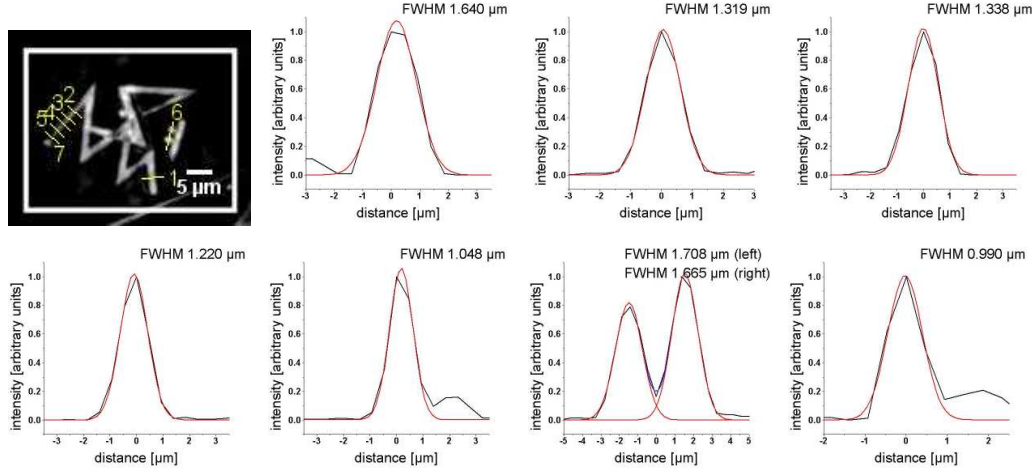
Figure 4.8: Gaussian fits through the indicated structure parts

a value slightly larger than the theoretical lateral resolution of the geometry - $\delta_{lateral}^{theo} = 725$ nm [65,68].

4.3 Conclusion

During the series of beamtimes at BESSY II it could be proven that tunable VUV illumination with picosecond pulses is applicable to digital in-line holographic microscopy. Furthermore, for the first time, submicron resolution could be achieved with this method, i.e. with digital synchrotron point source holography using pinholes. Nevertheless, as became clear in the course of the work presented here, the method is still in its infancy and requires significant developments, in particular in terms of processing and adaptation of the implemented materials. The fabrication of pinholes in opaque backings to improve the contrast between blocked and transmitted intensities, the minimization of the hologram distortion due to the beam block, and the adaptation of the sample are mandatory improvements to be made. Nevertheless, by overcoming these obstacles, further exploitation of the method with higher numerical apertures through more sophisticated geometries and smaller pinholes as well as even shorter wavelengths and higher coherent

photon flux for instance through exploitation of the XFEL seems within immediate reach.

Chapter 5

Holographic Imaging of Tracer Particles in Flow Channels

5.1   Introduction

Trajectories of particles moving through three-dimensional space have been studied extensively in various scientific branches. Especially the behavior of liquid flows in capillaries is very important for a better understanding of flow phenomena as for example in microcapillary devices, electrophoretic biochips, blood and lymph circulation, protein adsorption, calcification and dialysis. Liquid flows in micro- and nanocapillaries obey the laws of conventional continuum mechanics [83], yet the smaller characteristic length scales such as channel length and width, and the increased surface-to-volume ratio of the fluid and its surroundings result in a slightly changed behavior of the fluidic system. Flow velocities in microfluidic systems are smaller, thus interface phenomena, e.g. the stick-slip behavior of the fluid and its interaction with the walls of the capillary gain importance. The small channel dimensions additionally result in a strictly laminar fluid flow, limiting the ability to accomplish efficient and effective mixing [84]. Optimized intermixing processes of different analytes in a buffer medium have been accomplished by grooved surfaces [85], electro-osmosis in surface-modified systems [86], use of conduc-

tivity gradients [87], magnetic fields [88], bubbles [89], gaseous slugs [90] and acoustic stirring [91]. The imaging of flow profiles and mixing processes in microcapillaries is usually monitored by adding fluorescent dyes to one of the solutes and monitoring its mixing with the solvent [85–87], sometimes including an initial caging of the dye and a subsequent rapid uncaging prior to the measurement [92].

Another method of determining flow profiles is via tracer particles, as for example the examination of viscous properties of the medium in tracer microrheology [93, 94]. By individual observation of the tracer particles the flow in confined channels has been visualized [95, 96]. An optical method used to measure velocities and related properties in fluids is particle imaging velocimetry (PIV) [97, 98] where the tracer particle's path in the fluid is recorded. An extension of the method towards micron-scale spatial resolution (µ-PIV) has been used to determine velocity, shear stress, temperature, and heat flux in microfluidic systems [99, 100].

The above-mentioned imaging techniques make use of optical microscopy as this is the most common method for multiple magnification of small objects. The disadvantages of that method have been discussed in Section 6.12. DIHM offers the possibility to obtain high resolution three-dimensional images of a sample volume from a single hologram, thus circumventing the drawback of long recording times. As demonstrated by the group of H.J. Kreuzer [32,33], DIHM is a simple, since lensless and with regard to sample requirements undemanding method. Furthermore, instantaneously maximum information can be obtained with a resolution only limited by the wavelength of the laser which can be extended into the fourth dimension by tracking the particles over time.

The normal protocol to be followed prior to reconstruction as described in Chapter 1 in short includes

1. Digital recording of the hologram, i.e. its intensity matrix I_{nm}, on the camera chip.

2. Digital recording of the intensity matrix of the source without the object present.

3. Numerical construction of the contrast image $\tilde{I}_{nm}$ by subtracting the intensity matrix of the source from that of the image (see Equation 3.1) in Section 3.1.

This procedure corrects the laser source for deficiencies resulting from the imperfect shape of the pinhole or any defect introduced by the laser beam itself. In the case of a moving object whose trajectory is supposed to be recorded, this procedure needs to be modified [34]:

1. A sequence of holograms h_i is recorded.

2. Each two consecutive holograms are subtracted from each other in the form $h_i - h_{i+1}$ to remove all undesired background effects.

3. The difference holograms of (2.) are summed up into one single hologram

$$\sum_{i=1}^{n}(-1)^i \, h_i \tag{5.1}$$

of the same pixel amount and dynamic range as the original ones.

Combining the images alternating summation and subtraction prohibits exceeding the dynamic range in addition to the elimination of all static artifacts in the hologram. The resulting hologram can now be processed as usual and reconstructed with the Kirchhoff-Helmholtz formula (Equation 1.31).

5.2 Polystyrene Beads in Fluidic Environments

Experiments in this section were done using the following setup (Figure 5.1): The required coherent light is provided by a red HeNe laser with the wavelength $\lambda = 632.8$ nm. The optical path contains several lenses, pinholes and filters in order to clean the beam before it enters the inverse microscope (Zeiss
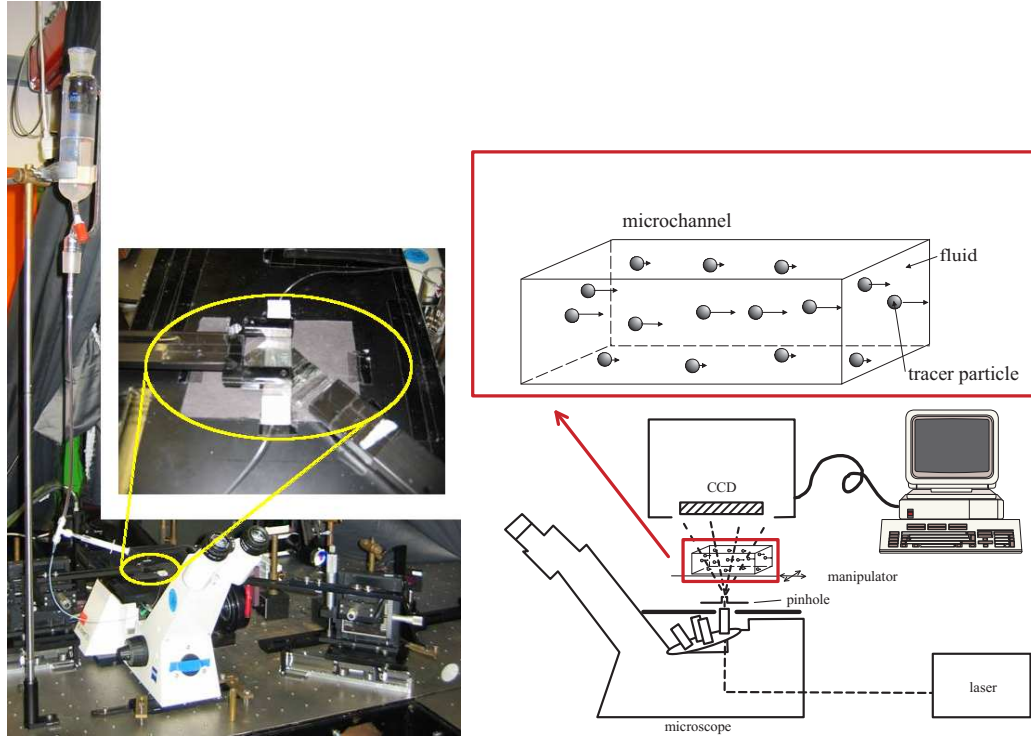
Figure 5.1: Holographic setup used to examine fluidic samples

Axiovert 25, Zeiss, Jena) that is used to locate the desired sample section prior to taking the hologram. A pinhole is positioned between the microscope's objective lens and the sample causing the emerging spherical wave to propagate through the selected sample section. A CCD camera (Photometrics, USA, 1024 x 1024 pixels with a length of 24 µm each) which is positioned above the microscope records the hologram.

5.2.1   Beads in Shrinking Water Droplet

The first experiments in a fluidic environment were done by letting a droplet of diluted 2.9 µm polystyrene beads air dry on a glass slide. Due to evaporation of the liquid the droplet shrinks and the contracting border moves the beads along. Figure 5.2 shows four subsequent holograms that were taken approximately 18 s apart from each other. The holograms were taken with a numerical aperture of 0.19, thus leading to a theoretical lateral resolution
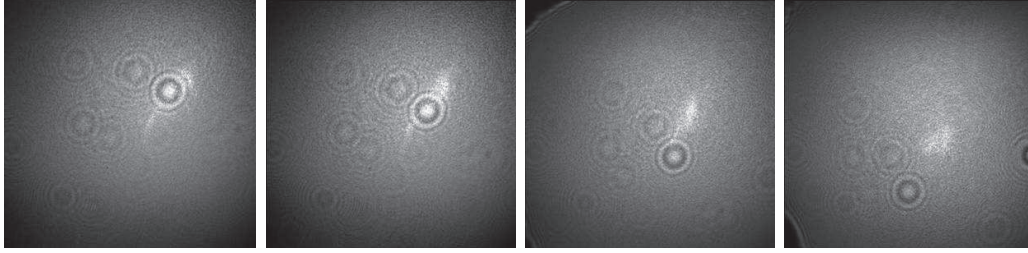
Figure 5.2: Holograms, time sequence t_1 to t_4, $\Delta t \approx 18$ s, $NA = 0.19$, $\delta_{lateral}^{theo} = 1665$ nm

of 1665 nm. The movement is clearly observable by the different positions of the interference fringes. On the left-hand side of Figure 5.3 the consecutive addition and subtraction according to Equation 5.1 of these subsequent holograms is shown. The reconstruction on the right-hand side at a distance of 221 µm depicts an obvious downward movement of the beads. In comparison with reconstruction images where the source has been subtracted rather than subsequent images, there seems to be less noise in Figure 5.3. This effect can be observed in all reconstruction pictures with consecutive subtractions. Disturbing side effects are reduced by this method due to the fact that everything stationary is depleted in the subtraction process. Thus, everything except for the moving particles is canceled out.
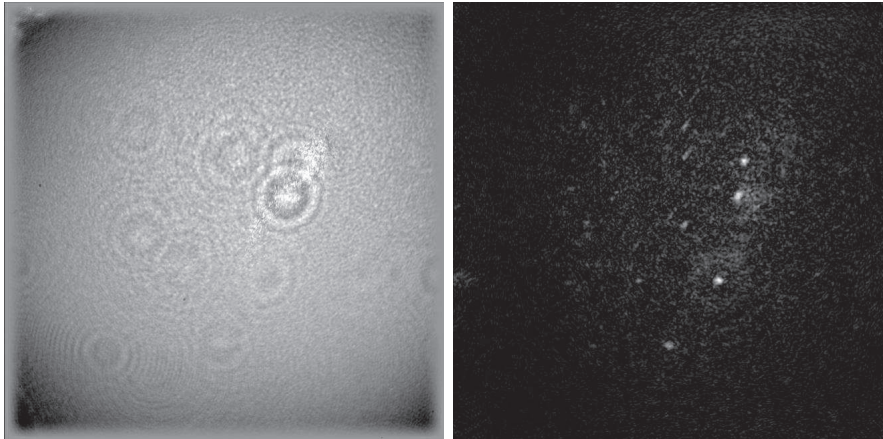
Consecutive subtraction of the four holograms in Figure 5.2

Reconstruction, $d_{rec} = 221$ µm

Figure 5.3: Combined hologram and reconstruction of 2.9 µm beads in shrinking water droplet

5.2.2   Beads in Flow Cell - Short Exposure Times
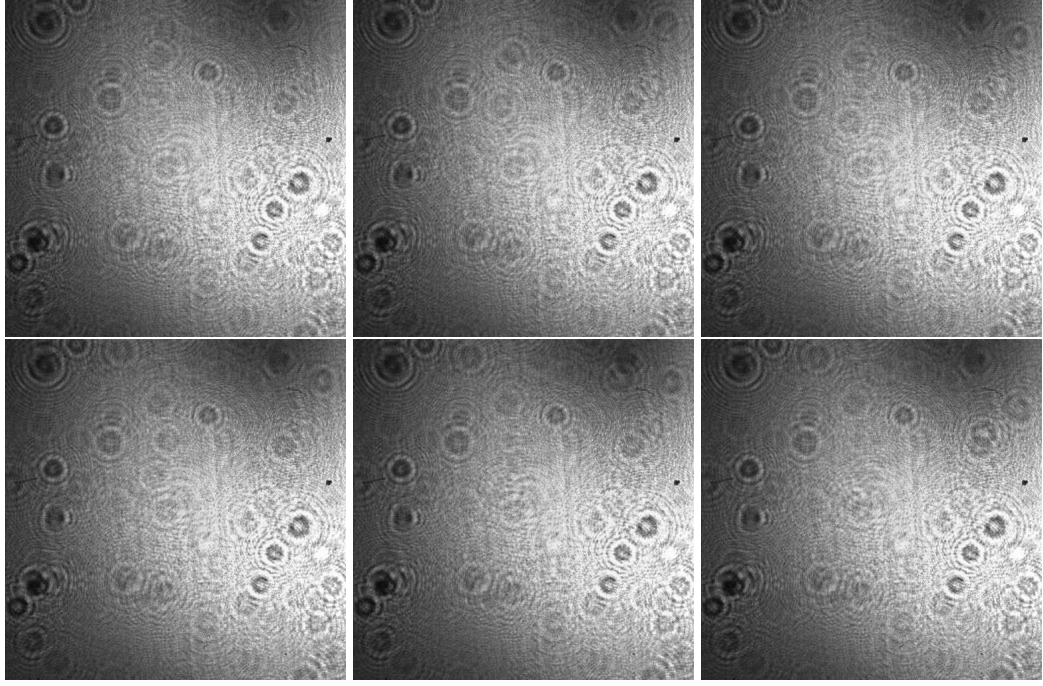
Figure 5.4: Series of consecutive holograms, time sequence t_1 to t_6, $\Delta t \approx 15$ s, $NA = 0.21$, $\delta_{lateral}^{theo} = 1507$ nm

Experiments with beads in a directed flow were carried out using commercially available flow cells (Ibidi - Integrated BioDiagnostics). The slide used (see Section 2.2.4) contains a volume of 30 µl. PVC tubes with an inner diameter of 2.0 mm were coupled to the slide by Luer-lock adapters and a simple gravity flow system was implemented. In Figure 5.4 a series of six holograms of 5.9 µm polystyrene beads in solution are shown. The numerical aperture of the geometry was 0.21, thus leading to a theoretical lateral resolution of 1507 nm. The exposure time was 100 ms for each hologram. However, due to the long read out times of the detector, the time difference between two holograms was about 15 s. The left-hand side in the top row of Figure 5.5 shows the consecutive subtraction of these holograms and on the right-hand side the reconstruction at a distance of 2700 µm is displayed. Here, similar to the reconstruction in Figure 5.3, the movement of various beads in negative y-direction is clearly observable. Different beads travel

with different velocities which becomes apparent by the different distances
between the trajectory points of the beads. As the flow in this rather large
channel is not strictly laminar, a few turbulences can also be seen.

Below, 3D-rendered bead trajectories constructed from that single difference
hologram are shown. Reconstructions at various depths ranging from 2200
to 3000 µm through the sample volume were made and the bead coordinates
along their trajectories extracted in order to construct the 3D representa-
tion. The 3D trajectory analysis program was written in Matlab by M.
Heydt (Angewandte Physikalische Chemie, Universität Heidelberg).
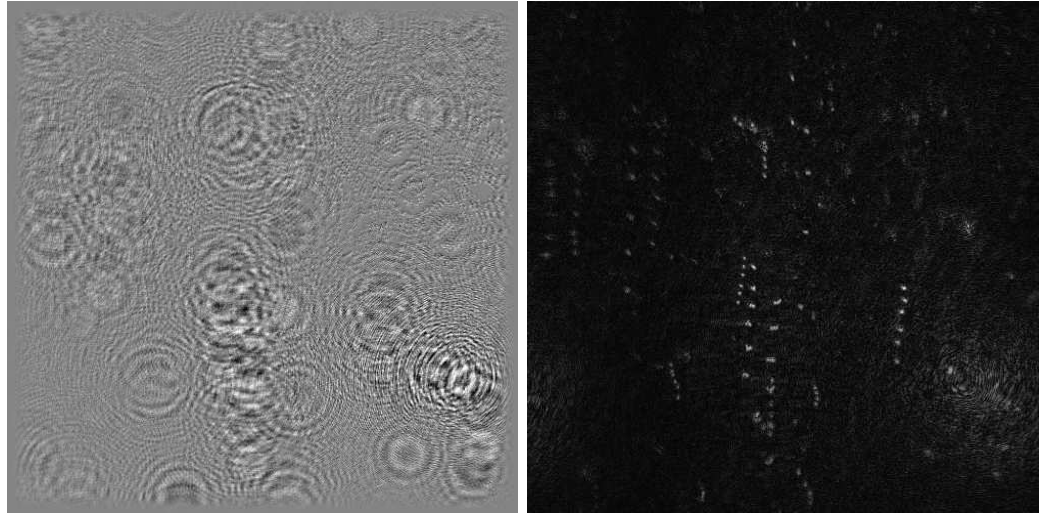
Consecutive subtraction of the six
holograms from Figure 5.4

Reconstruction,
$d_{rec} = 2700$ µm

xy-plane projection   xz-plane projection   yz-plane projection
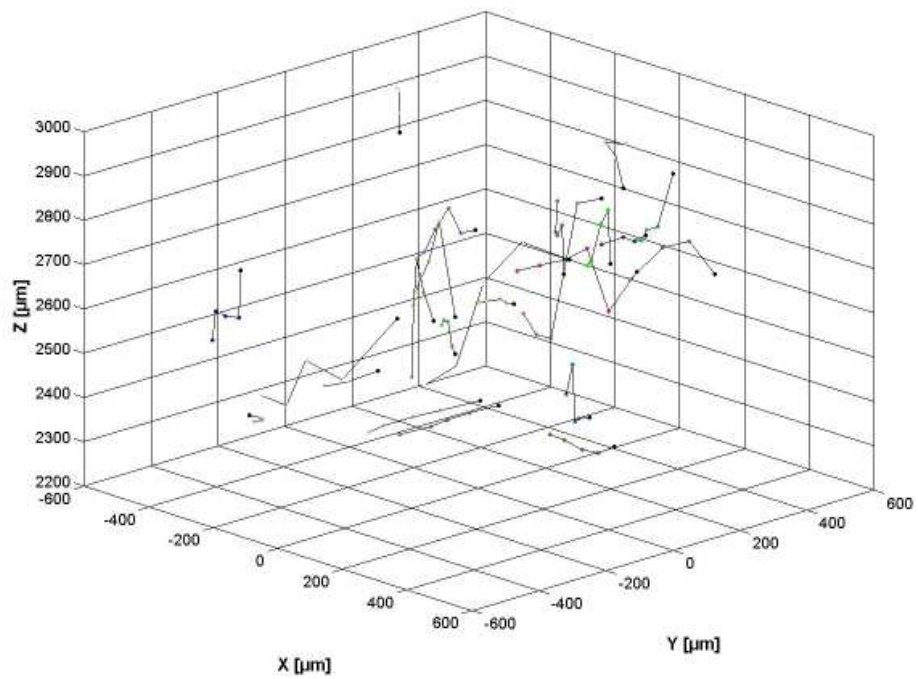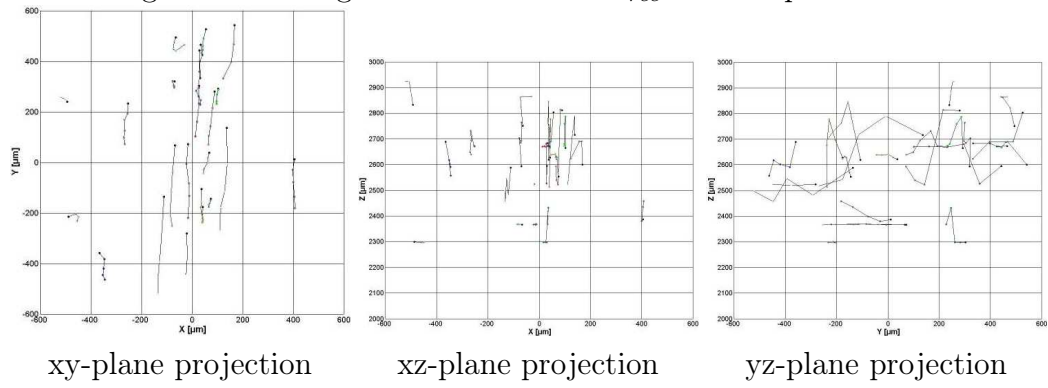
Figure 5.5: 4D analysis of 5.9 µm beads in a flow channel

5.2.3 Beads in Flow Cell - Long Exposure Times
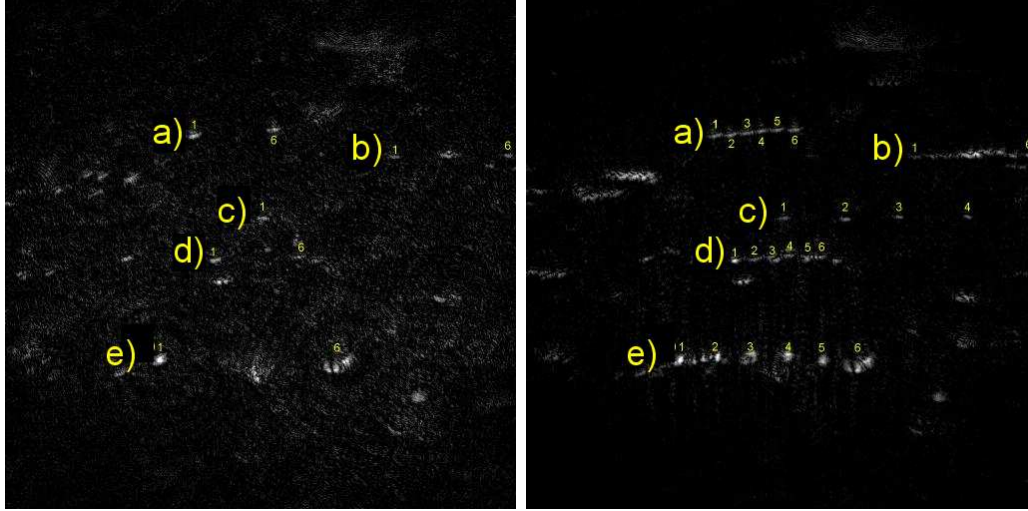
Reconstruction of two holograms,
$\Delta t \approx 20$ s,
$NA = 0.21$, $\delta_{lateral}^{theo} = 1838$ nm,
$d_{rec} = 2100$ µm

Reconstruction of six holograms,
$\Delta t \approx 4$ s,
$NA = 0.21$, $\delta_{lateral}^{theo} = 1838$ nm,
$d_{rec} = 2100$ µm

Figure 5.6: Reconstruction of composite holograms of 5.9 µm beads in large flow channel

In order to examine the channel's flow profile, a filter was introduced into the beam path which allowed for longer exposure times without the chip being saturated. The same 5.9 µm beads as in Section 5.2.2 were used in an, apart from the filter, unchanged setup. The left image in Figure 5.6 shows the reconstruction of a composite hologram of two recordings that were taken approximately 20 s apart from each other. Some lines can be seen that indicate moving beads. The right image in Figure 5.6 shows a reconstruction of a composite hologram of six subsequent recordings, including the two shown on the left-hand side which were the first and the last recording of the sequence. Five trajectories of moving beads are indicated. From the exposure time of 3 s and the recorded sample section of 937 x 937 µm^2 the different velocities can be calculated. Bead a) traveled a total distance of 168 µm within the six frames. The exposure time was 3 s per frame and the

dark time between exposures was 1 s. This yields a velocity of

$$v \; = \; 168 \; \text{µm}/(6 \cdot 3 \; \text{s} + 5 \; \cdot 1 \; \text{s}) \; = \; 7.3 \; \text{µm/s}$$

for the bead in trace a). Bead b) travels 222 µm in 23 s, thus at a speed of
9.7 µm/s. Bead c),d) and e) advance at 23.5, 7.4 and 15.2 µm/s, respectively.
As mentioned in Section 5.2.2, different beads travel with different velocities,
especially in these rather large channels. The reconstruction also shows some
brighter spots that indicate slower beads. These beads were detected by one
pixel for a longer period of time causing higher intensities in the reconstruc-
tion. These brighter sections complicate the detection of the faster particles'
lines of lower intensities. Quite interesting is the fact that bead e) covers the
largest overall distance although the bead seems to linger in the same spot
during the single exposure time of 3 s. This might be due to the fact that the
outlet capillary was hanging freely above the water surface inside the glass
beaker in this experiment, enabling droplet formation. Thus, the flow was
not continuous but somewhat jerky. The experiment confirms, however, the
feasibility of characterizing the flow in a channel via in-line holography.

5.3   Oil-in-Water Emulsion

In addition to the latex spheres, small oil droplets in an oil in water emulsion
can also function as tracer particles. Clearly detectable through their higher
refractive index $n_{oil} \; = \; 1.486$ (at $\lambda \; = \; 589.3$ nm and 20°C [101]), linseed
oil droplets were used to monitor the flow of the surrounding water in the
same channel as described in Section 5.2.2. The setup was identical to the
one displayed in Section 5.2. The combined hologram on the left-hand side
in the top row of Figure 5.7 is the alternating addition and subtraction of
a series of eight consecutive holograms taken 15 s apart. The numerical
aperture in this case was $NA \; = \; 0.22$, yielding a theoretical resolution of
1755 nm. The next panel of Figure 5.7 shows the trajectories of multiple oil
droplets at a reconstruction distance of $d_{rec} \; = \; 2660$ µm. Their movement

Consecutive subtraction of eight holograms, $\Delta t \approx 15$ s, $NA = 0.22$

Reconstruction, $d_{rec} = 2660$ µm, $\delta^{theo}_{lateral} = 1755$ nm

xy-plane projection

xz-plane projection

yz-plane projection
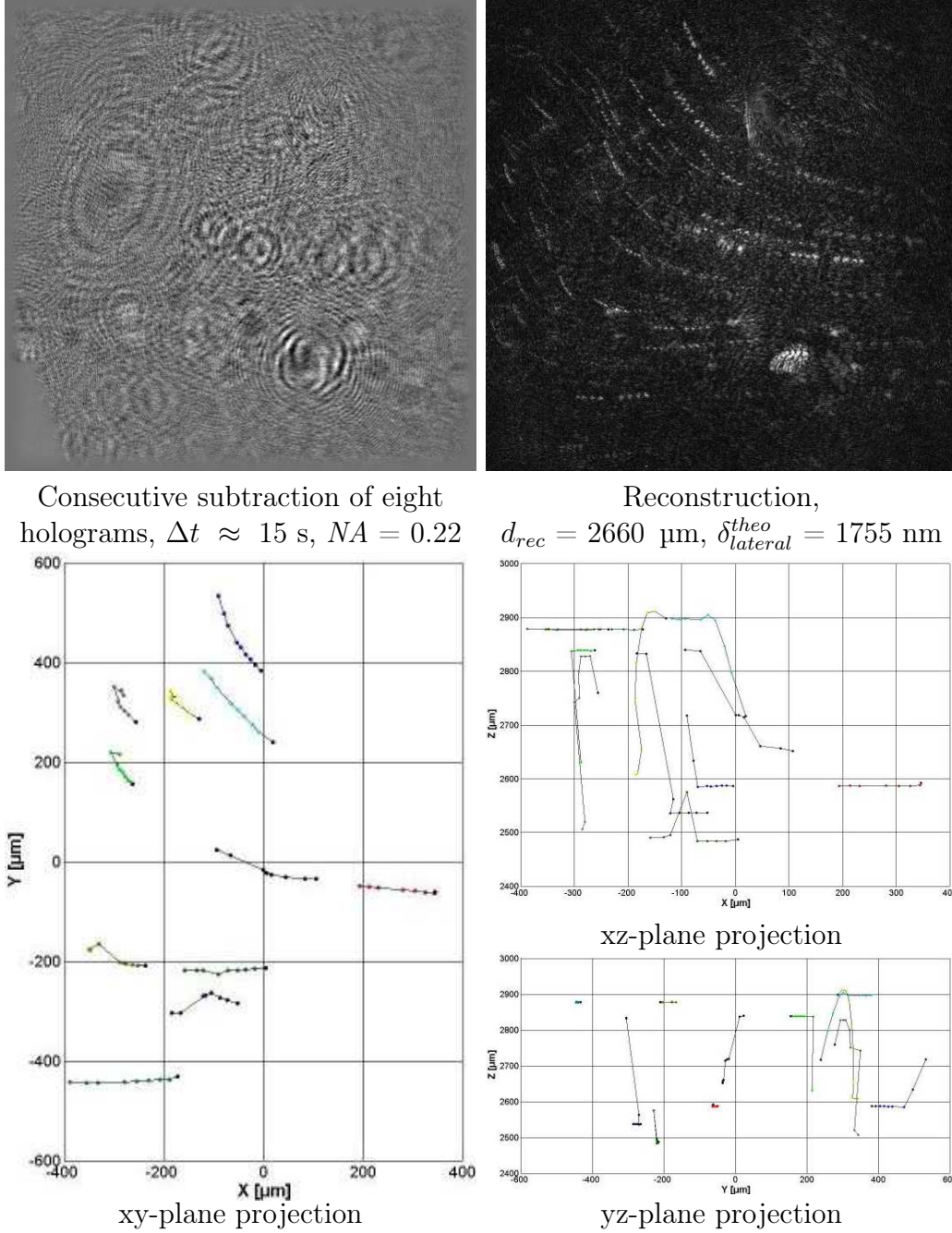
Figure 5.7: 4D analysis of oil-in-water emulsion in a flow channel
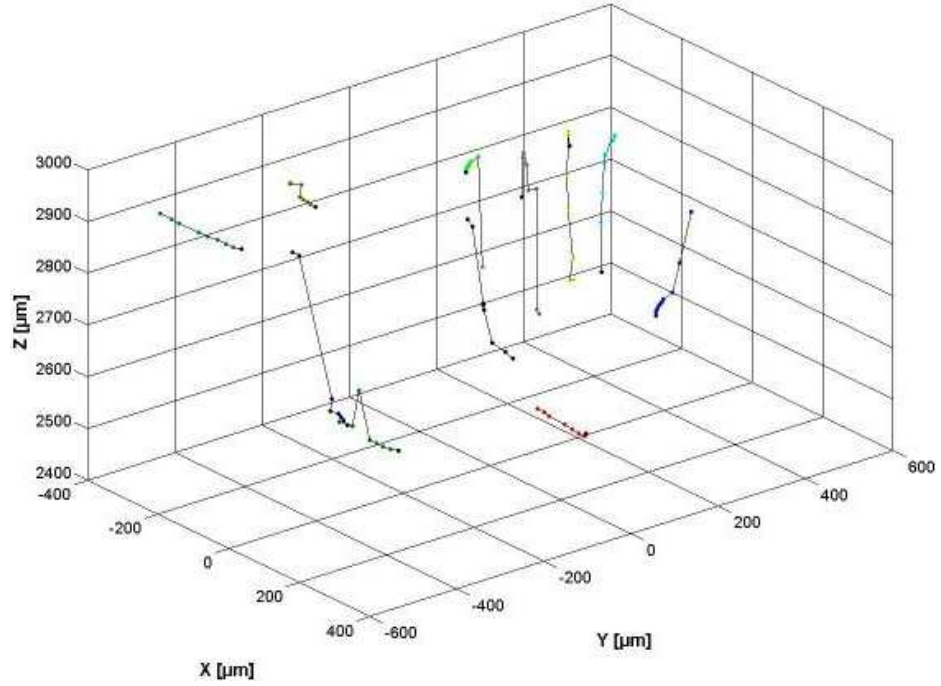
Figure 5.8: 4D display of oil-in-water emulsion in flow channel

is slightly curved, indicating convection that most likely is created through heating with the illuminating laser. A 3D-rendering for a few trajectories was also done, showing clearly that the movement of the oil droplets was not confined to one plane but detectable over the whole depth of the sample volume from 2400 to 3000 µm.

5.4   Cyclohexane-in-Water Emulsion

Another interesting subject to study is the local mixing of liquids with different refractive indices. Figure 5.9 shows the reconstructions of combined holograms that were created by subtracting two holograms approximately 200 ms apart. Two perfusion pumps model Pump11PicoPlus (Harvard Apparatus, USA) injected water and a cyclohexane-in-water emulsion at a pump rate of 500 µl/hr into two openings of an intersection channel. The channel (width: 100 µm, depth: 3.7 µm) was fabricated at the IMT (Forschungszentrum Karlsruhe) out of a 500 µm thick PMMA plate (HESAGlas HESAlite)
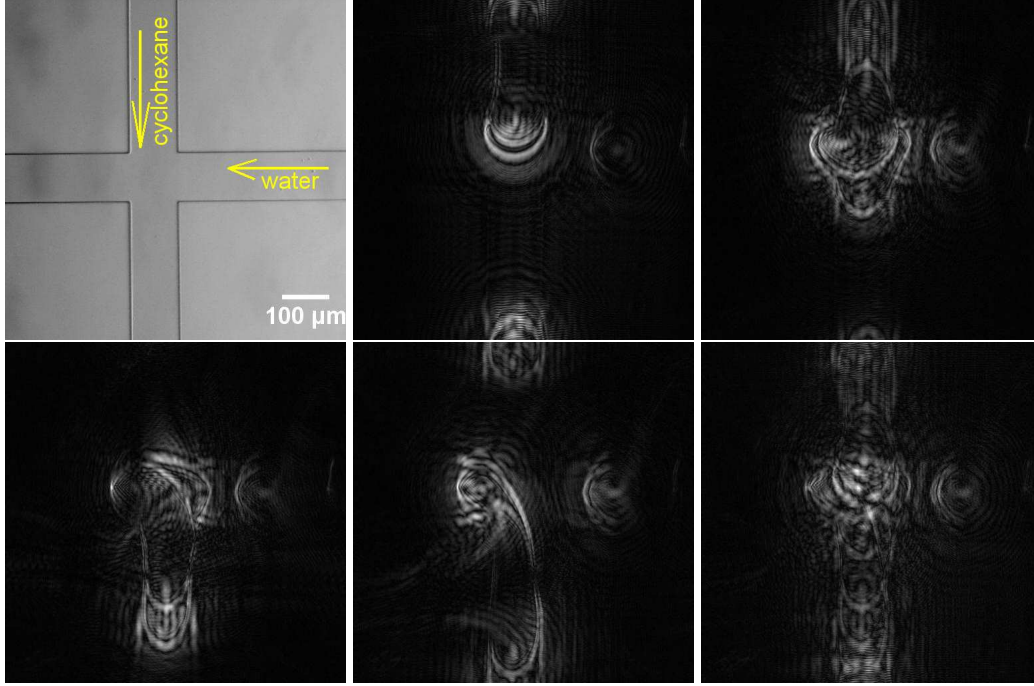
Figure 5.9: C_6H_{12}/H_2O-emulsion in a flow channel, time interval I, $NA = 0.21$, $\delta_{lateral}^{theo} = 1293$ nm
Top left: Microscopy image, Zeiss A-Plan objective 40x, $NA = 0.5$,
Top middle, right and bottom left, middle: reconstructions of subtraction holograms of each two consecutive holograms
Bottom right: reconstruction of the combination hologram of all eight consecutive holograms

covered with a 500 µm thick PMMA lid. Due to its higher refractive index of 1.4235 [102], the disperse cyclohexane phase is easily distinguishable from the continuous water phase. In the first sequence, the emulsion reaches the intersection from above, gets minimally carried along by the water stream coming from the right, and then continues its way downwards through the channel. The last panel in the figure shows the reconstruction of all eight holograms combined. The setup of this experiment is equal to the one described in Section 5.2, with the difference that the illumination was provided by a green HeNe laser ($\lambda = 543$ nm) and the images were recorded with a CCD camera model Lu160 (Lumenera, Canada; chip size 0.8256 cm x 0.6604 cm, 1280 x 1024 pixels) as this camera can reach the required recording fre-

quency of 15 fps. The numerical aperture in this setup was 0.21, leading to a theoretical lateral resolution of 1293 nm. Figure 5.10 shows the time
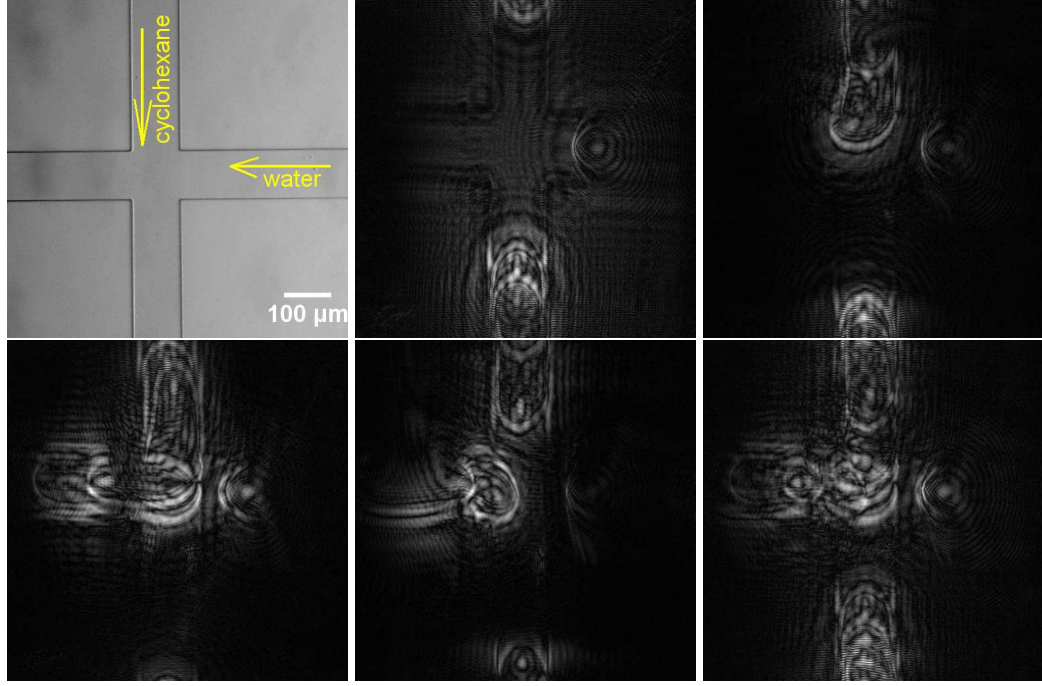
Figure 5.10: C_6H_{12}/H_2O-emulsion in a flow channel, time interval II, $NA = 0.21$, $\delta_{lateral}^{theo} = 1293$ nm
Top left: Microscopy image, Zeiss A-Plan objective 40x, $NA = 0.5$,
Top middle, right and bottom left, middle: reconstructions of subtraction holograms of each two consecutive holograms
Bottom right: reconstruction of the combination hologram of all eight consecutive holograms

interval of the following second. This time, the cyclohexane emulsion gets carried away into the left channel arm by the water stream coming from the right. This alternating behavior could in fact be monitored over the complete length of the experiment.

5.5   Conclusion and Outlook

Micro- and nanofluidic processes are getting more and more important in various domains, for example in electrophoretic biochips, microcapillary de-

vices, to study the mixing behavior of two phases or for microreactors. Flow on small scales differs greatly from conventional continuum flow as physical phenomena that can be neglected on the large scale become of importance with decreasing size. Furthermore, external means such as channel geometry and texture can influence liquid flow. The goal of this research was to show that by digital in-line holography microflows of liquids can be monitored and principally characterized. These first experiments show that the developed method holographic µPIV is generally applicable for these purposes. Further investigations could include the characterization of liquids in systems whose walls have been chemically modified, e.g. by coating with ultrathin organic films. Thus, for example the hydrophilicity of the walls can be controlled or the grafting of polymer brushes with various densities. A well-established technique to modify chemical properties on surfaces is by use of ordered molecular assemblies formed by the adsorption of an active surfactant on a solid surface, so-called self-assembled monolayers (SAMs). Spontaneous chemical synthesis at the interface leads to the order phenomenon. SAMs have the advantage of an easy preparation and are highly reproducible [103]. Additionally, they allow the investigation of specific interactions at interfaces. The chemical properties of the system can be varied by changing the end groups of the SAMs. The degree of hydrophobicity, for example, can be monitored and adjusted by varying from apolar to polar end groups. Alternatively used can be polymers which express an interesting effect called coil-to-brush transition which occurs with increasing grafting density. Intermolecular interaction can be neglected if the polymers are sparsely populated and thus form a coil-like structure. With increasing coverage, however, intermolecular interaction becomes of importance and results in a lateral confinement evoking a stretching of the polymers which then form a brush-like arrangement [104]. As the coil-to-brush transition is simply a function of the immersion time in solution, preparation of amorphous coils, polymer brushes or quasi-cristalline monolayers is easily done by adjusting the immersion time. The morphology of the polymers subsequently influences quite a few properties, for example solvation behavior, water and ion uptake, stiffness, dichroism, refractive index and chemical reactivity [104] which in turn are likely to influence the

liquid flow inside the channel. Whitesides et al. [105] for example showed that in the region where the monolayer is maximally disordered in its outer structure the contact angle undergoes a significant change from hydrophilic toward hydrophobic.

Chapter 6

Holography with a Fiber Source

6.1 Introduction

An additional method to generate a divergent wavefront is by use of an optical fiber whose egression interface serves as a point source. One great advantage is their immense flexibility which would be an enormous experimental improvement compared to the conventionally used pinholes. The possible positioning of the source inside a solution allows for example the study of cells in their culture media at minimal reconstruction distances.

An example of the successful implementation of this type of point sources is the Scanning Near Field Optical Microscopy (SNOM). In this technique, the distance between source and sample is chosen smaller than the used aperture whose diameter in turn is significantly smaller than the illuminating wavelength. Thus, it is possible to go below Abbe's resolution limit (see Equation 1.19). Apertures down to 50 nm in diameter can be obtained for example through aluminium evaporation of optical fiber tips [106].

In the production of optical waveguides a glass fiber is formed that consists of two concentric glass cylinders with different refractive indices (Figure 6.1). The signal is transported in the inner cylinder, the core, through total reflectance at the interface between the two glass cylinders. The outer cylinder is called cladding. Both core and cladding are made of fused silica.

Commercially available are single- and multimode fibers whose main differ-
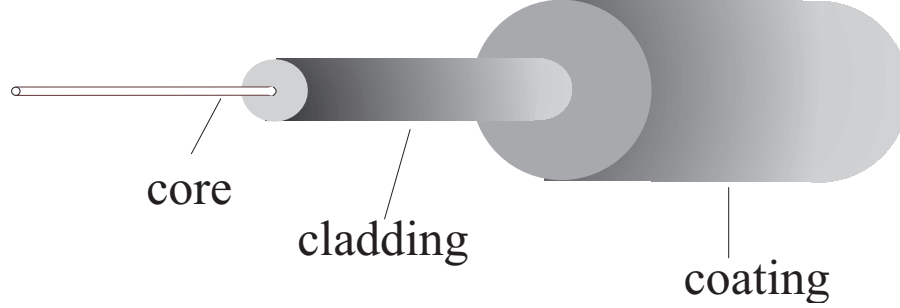
Figure 6.1:   Schematic drawing of the structure of an optical
waveguide

ence is the core diameter. Multimode fibers have a light guiding core with
a diameter a lot larger than the wavelength of the transported light, mostly
around 50 µm [107]. The outer diameter of the fiber is typically 125 µm.
Single-mode fibers have a core diameter of about 7 to 10 µm, yet their outer
diameter is usually still 125 µm [107]. Modes are discrete light waves that
travel through the core of a waveguide if the light has been coupled into the
fiber under an angle smaller than or equal to α_{max}:

$$\alpha_{max} \quad = \quad \arcsin \sqrt{n_c^2 - n_{cl}^2} \tag{6.1}$$

$$= \quad \arcsin NA_{in}, \tag{6.2}$$

where n_c and n_{cl} are the refractive indices of the core and the cladding,
respectively, and NA_{in} is the intrinsic numerical aperture of the fiber. De-
pending on the amount of modes that are able to disperse in the fiber, the
waveguides are called mono- or multi-mode fibers: while a mono-mode fiber
can only carry a single mode, multi-mode fibers guide hundreds of modes
with different path lengths [107].

6.2   Experimental Setup

In order to be able to directly compare the implementation of fiber ends as
point sources to conventional pinholes, a special combined setup was designed

that allows the exchange of the point source in the course of an experiment. Visible green laser light with a wavelength of 543 nm is produced by a cylindrical HeNe laser model 25LGR393 (Melles Griot) operating in cw mode with an output power of 2 mW and a coherence length of about 30 cm. After the laser beam passes the external shutter, its path is chosen according to the experiment's requirements. It either proceeds straightforward (Figure 6.2, top) through a series of lenses and pinholes for cleansing and shaping before being focused by an objective (Zeiss A-Plan 20x, $NA = 0.75$) onto the previously stripped and cut end of the 460HP single-mode fiber (Thorlabs, USA), sustained by a fiber chuck (Newport, USA). The waveguide then directs the light to a second fiber chuck in front of the detector. The whole system is mounted on a cage system (Thorlabs), allowing the clamp retaining the second fiber chuck to be flipped aside and substituted by the mount holding the pinhole if the latter is the desired point source. In that case (Figure 6.2, bottom), a mirror is introduced into the beam path right behind the external shutter, redirecting the beam over a second mirror onto another cleansing and shaping series of lenses and pinholes before focusing it onto the final pinhole (National Apertures) by a homemade objective (lenses and frame purchased from Linos Photonics, Göttingen). Objective and pinhole are mounted on the same clamp, allowing their exchange for the fiber chuck by simple flipping. The sample is mounted in the now again identical beam path on an xyz-stage between the respective point source and the detector, a CCD camera AT200 (Photometrics) with a SI003 chip (1024x1024 pixels on an area of 24x24 mm^2).
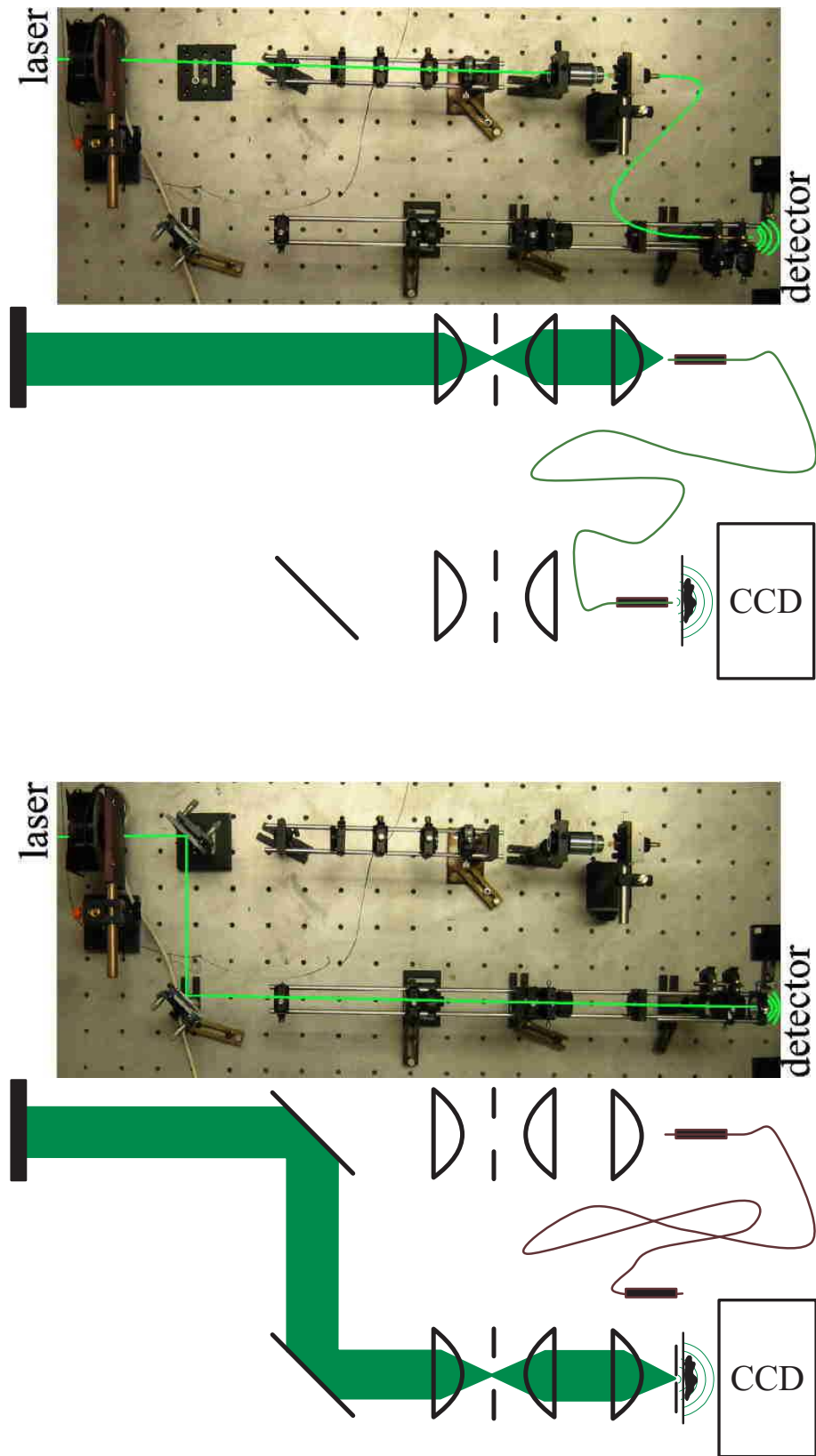
Figure 6.2: Combination setup for holography with fiber (top) and pinhole (bottom) point sources

6.3 Optical Fibers as Alternative Point Sources

The objects imaged in these experiments were test structures on borosilicate glass, polystyrene beads and REF52 wt fibroblast cells. The test structures were fabricated by hot embossing by K. Mandisloh (IMT, Forschungszentrum Karlsruhe). A polystyrene bead suspension (Polysciences, USA) was diluted and applied onto glass substrates and subsequently air-dried. The cultivation of fibroblast cells was done by immersion in DMEM medium and incubation in CO_2 for 36 hrs. After fixation with glutaraldehyde the intracellular water was exchanged with ethanol and the cells subsequently critical-point-dried (see Section 2.2.2).

6.3.1 Polystyrene Beads

Figure 6.3 shows the results for the imaging of individual, monodisperse 5.9 µm polystyrene beads. The hologram was recorded with the 543 nm laser setup described above. Special care was taken to chose a source-detector distance that yields full illumination of the chip in order to be able to extract maximum information from the interference fringes. The theoretical lateral resolution was 2088 nm. The reconstruction at a distance of 1960 µm away from the point source is shown in the top right panel, showing an arbitrary distribution of beads. A region of special interest indicated by the yellow rectangle is magnified in the bottom left panel. The intensity profile through the bead dimer as indicated by the arrow is shown on the bottom right. The peak-to-peak distance is 6.03 µm, in excellent agreement with the nominal particle size thus confirming the fact that the object in question really is a bead dimer. No additional broadening is observed which is not surprising as the size of the particles is about twice the size of the theoretical resolution. These results are confirmed by the measurement displayed in Figure 6.4 where identical conditions applied. The reconstruction plane here is 2000 µm from the point source and the peak-to-peak distance of the line profile (bottom right panel) through the bead dimer shown in the bottom left and indicated by an arrow yields again the nominal particle size.

Hologram,
$\lambda = 543$ nm, $NA_{in} = 0.13$,
$\delta_{lateral}^{theo} = 2088$ nm

Reconstruction,
$d_{rec} = 1960$ µm

Magnified cutout of the area
indicated by the rectangle

Line profile through the bead dimer
indicated by an arrow
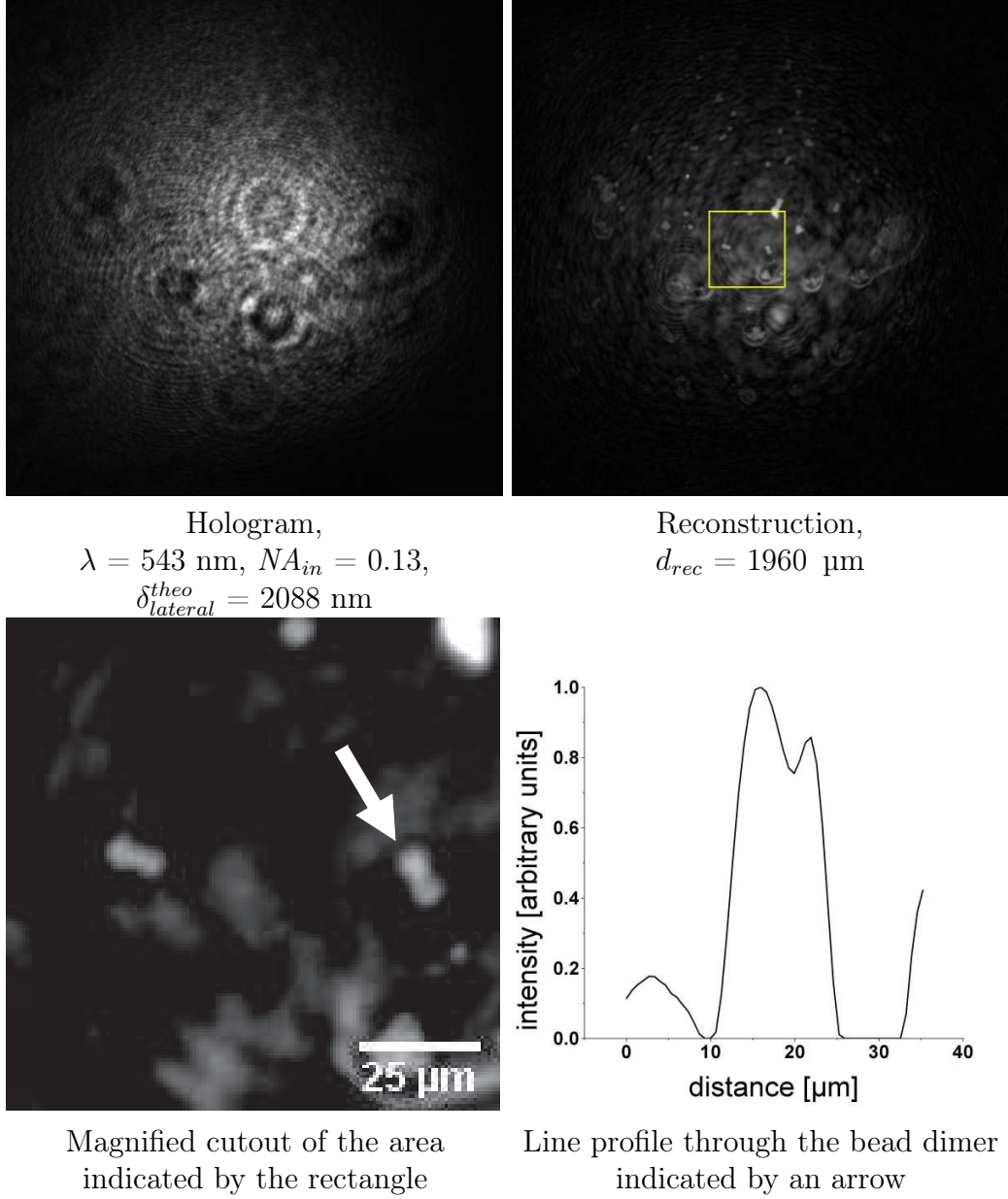
Figure 6.3: 5.9 µm polystyrene beads deposited on a glass slide

6.3.2   Test Structures

Test structures hot embossed into PMMA on borosilicate glass are displayed
in Figures 6.5 and 6.6. 543 nm laser light was used in the above-described
setup with a point source provided by an optical fiber. The intrinsic numer-

Hologram,
$\lambda = 543$ nm, $NA_{in} = 0.13$,
$\delta_{lateral}^{theo} = 2088$ nm

Reconstruction,
$d_{rec} = 2000$ µm

Magnified cutout of the area
indicated by the rectangle

Line profile through the bead dimer
indicated by an arrow
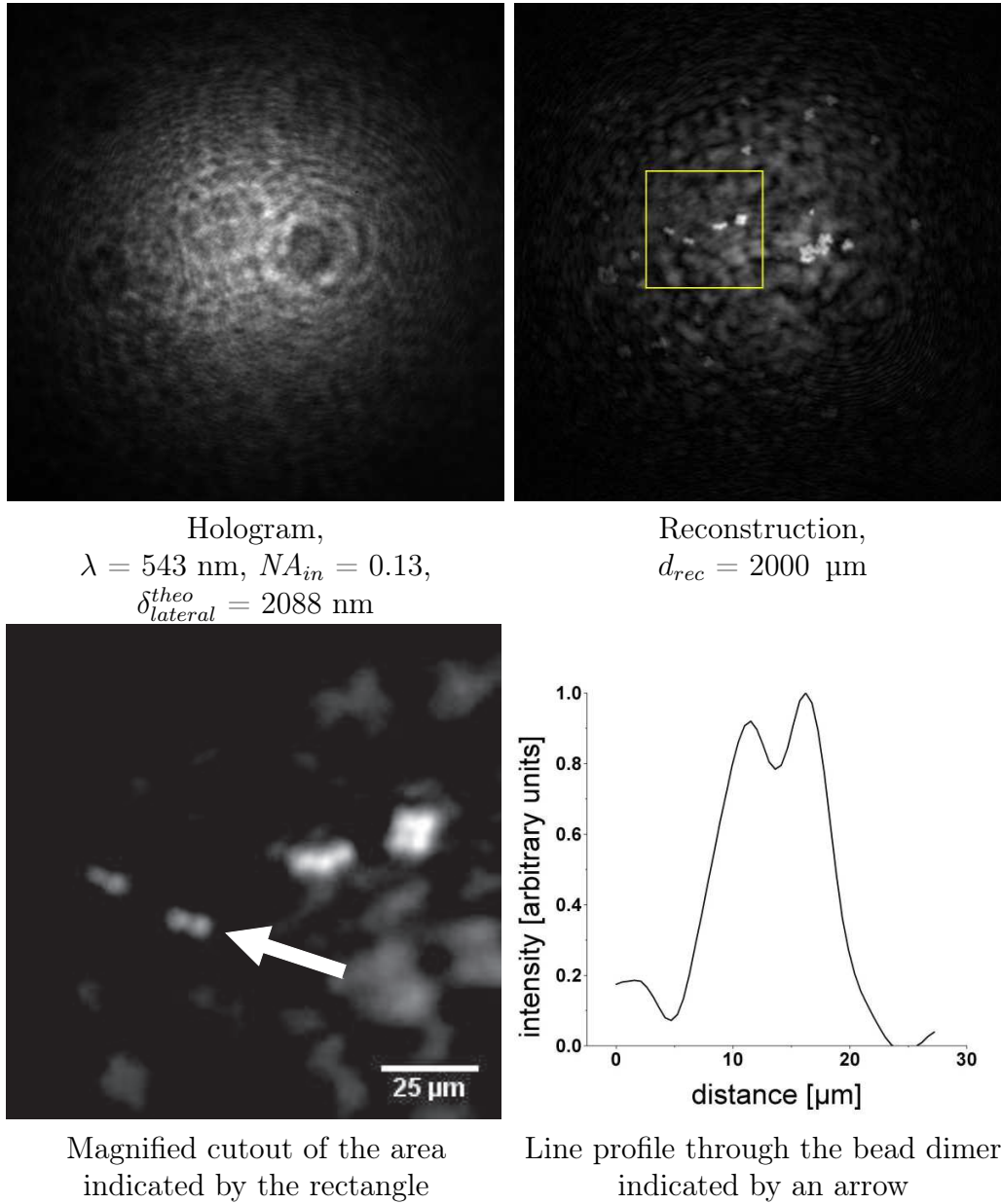
Figure 6.4: 5.9 µm polystyrene beads deposited on a glass slide

ical aperture of the fiber was 0.13, thus determining the overall numerical aperture of the system which yields a theoretical lateral resolution of 2088 nm. The microscopy image on the right in Figure 6.5 shows intersecting structures of 40 µm width which are precisely to scale in the reconstructed image in the center panel. The smaller bulge of 15 µm width is also resolved, although

Hologram,	Reconstruction,	Transmission light
$\lambda = 543$ nm,	$d_{rec} = 1110$ µm	microscopy image, Zeiss
$NA_{in} = 0.13$		A-Plan 10x, $NA = 0.25$
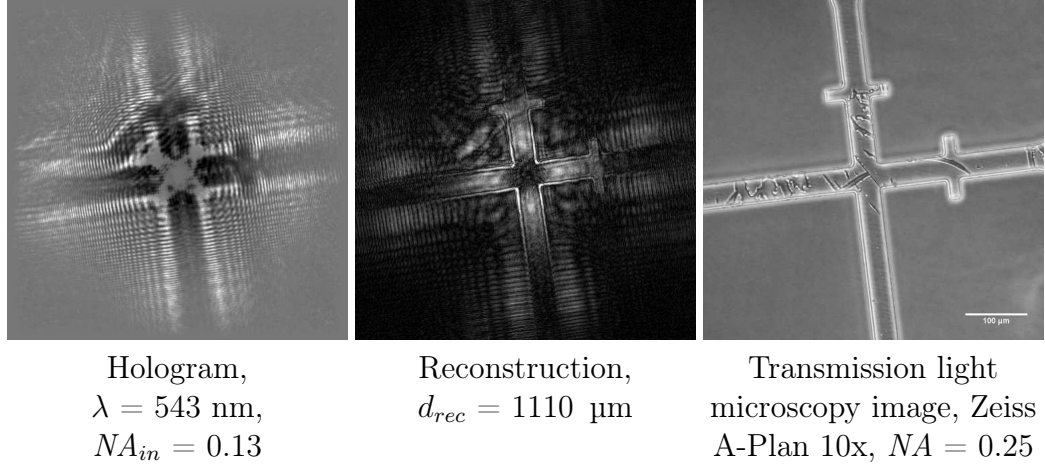
Figure 6.5: Intersecting test structures on borosilicate glass

slightly distorted due to its position further away from the center of the image. The triangular test structure in Figure 6.6 has a base width of 50 µm and the converging sides can be seen down to a distance of approximately 10 µm. However, this does not mean that the resolution limit is reached. The triangle apex is not resolved because in this experiment the detector chip was not fully illuminated as the fiber end was only 4.65 cm away. This results in a loss of information towards the detector borders. It also means that the numerical aperture can not be derived from the geometry of the setup $NA = D/(2\sqrt{(L/2)^2 + D^2}) = 0.39$ (see Equation 1.24) but is given by the effective numerical aperture NA_{eff}, determined by the percentage of the illumination on the detector. In the case of an optical fiber with a divergent emerging wavefront, NA_{eff} equals NA_{in} (see Equation 6.2). With the numerical aperture of $NA_{in} = 0.13$ a full illumination would require a distance $L = 9.46$ cm. In Figure 6.7 this is confirmed as the triangle apex is now clearly resolved. In this case it had been moved into the center of the illumination, i.e. the center of the detector's field of view. The left-hand side shows a reconstructed image at a distance of $d_{rec} = 1800$ µm. Line profiles through the images confirm a resolution below 3 µm which is slightly above the theoretical lateral resolution of $\delta_{lateral}^{theo} = 2088$ nm. A marginal broadening of the structure can be observed compared to the microscopy image.

Hologram,
$\lambda = 543$ nm,
$NA_{in} = 0.13$

Reconstruction,
$d_{rec} = 840$ µm

Transmission light
microscopy image, Zeiss
A-Plan 10x, $NA = 0.25$
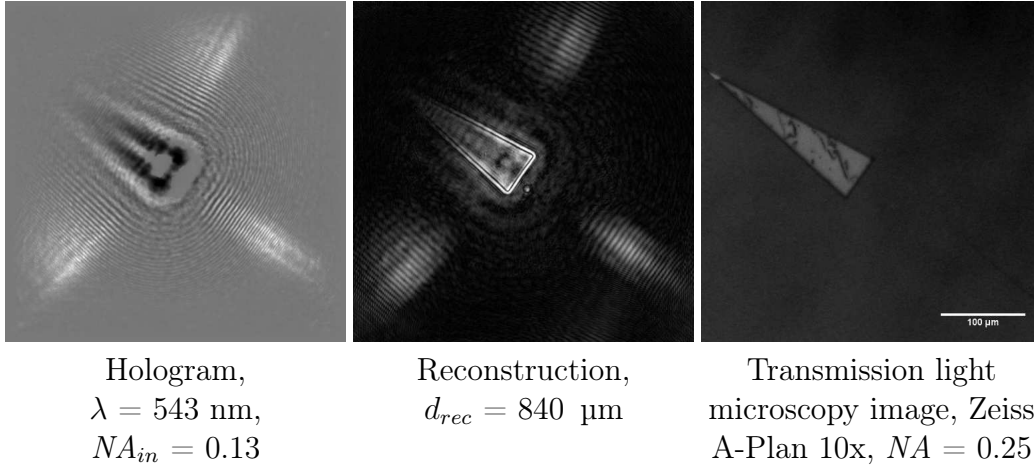
Figure 6.6: Triangular test structure on borosilicate glass

Reconstruction
$d_{rec} = 1800$ µm

Transmission light
microscopy image, Zeiss
A-Plan 10x, $NA = 0.25$
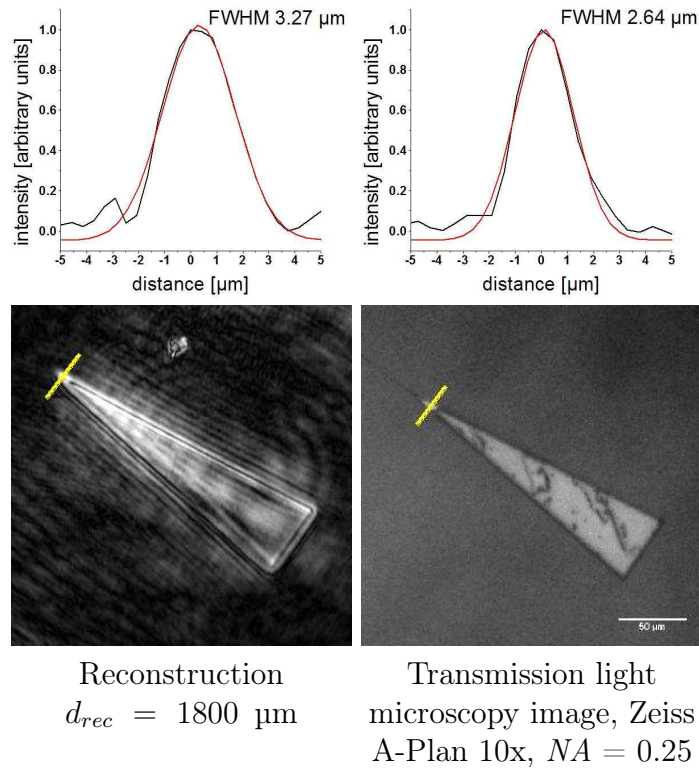
Figure 6.7: Triangular test structure on borosilicate glass

6.3.3 Fibroblast Cells

With regard to the possible implementation of optical fibers as point sources
immersed in solutions, e.g. the culture medium of living cells, the imaging

Hologram,	Reconstruction,	Transmission light
$\lambda = 543$ nm,	$d_{rec} = 3750$ µm,	microscopy image, Zeiss
$NA_{in} = 0.13$	$\delta_{lateral}^{theo} = 2088$ nm	A-Plan objective 10x,
		$NA = 0.25$
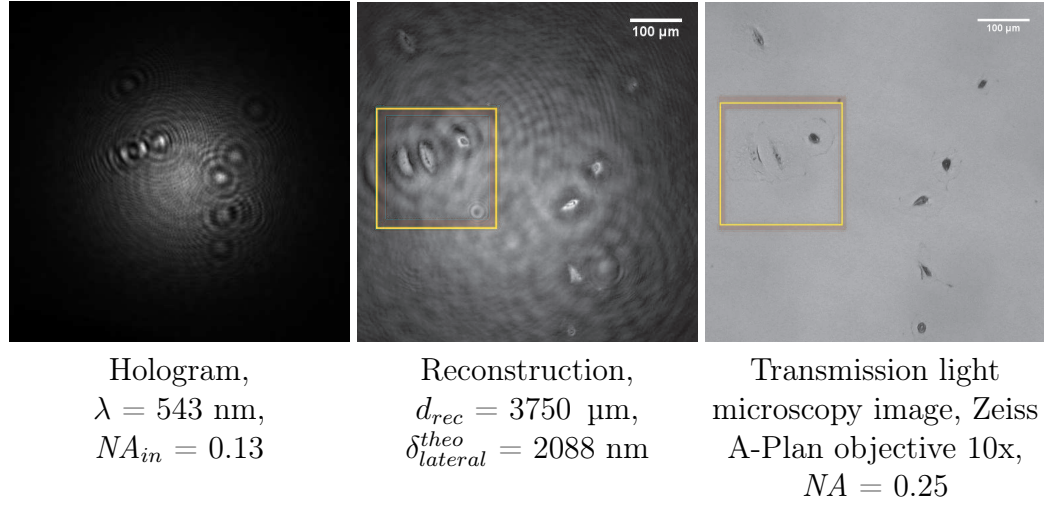
Figure 6.8: Fixed and critical-point-dried REF52 wt cells on a glass substrate

properties of biological samples with optical fiber illumination have been investigated. Figure 6.8 shows critical-point-dried fibroblast cells on a glass substrate. The hologram on the left-hand side was recorded with the green laser setup at 543 nm wavelength. It shows well-resolved interference fringes. The reconstruction in the center panel is $d_{rec} = 3750$ µm away from the source. The borders and filaments of these rather large objects appear sharp and distinct, an impression confirmed by the magnified inset shown in Figure 6.9. The delicate features are clearly visible. Additionally, even internal features within the cells are resolved. The slightly larger amount of material in the nucleus provides a phase contrast and appears as darker area with clearly defined borders in the reconstruction.

6.4   Comparison of Optical Fibers and Pinholes

Light diffracted by a pinhole's circular aperture has the form of an Airy pattern whereas the divergent beam emerging from the end of an optical fiber tip can be approximated by a Gaussian distribution. The practical consequence of this can be seen in Figure 6.10 where the images of the two sources at the detector at identical distances are shown. The intensity line profile

Reconstruction cutout   Microscopy image cutout
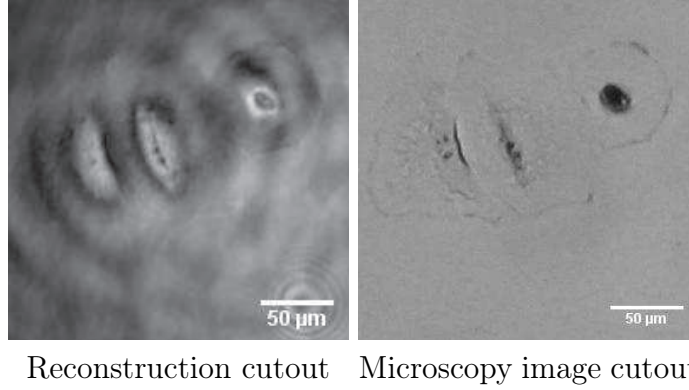
Figure 6.9: Magnified cutouts of the area in Figure 6.8 indicated by the rectangle

| 1.0 µm pinhole source, $NA = 0.39$ | Fiber source, $NA_{in} = 0.13$ | Line profile through the sources |
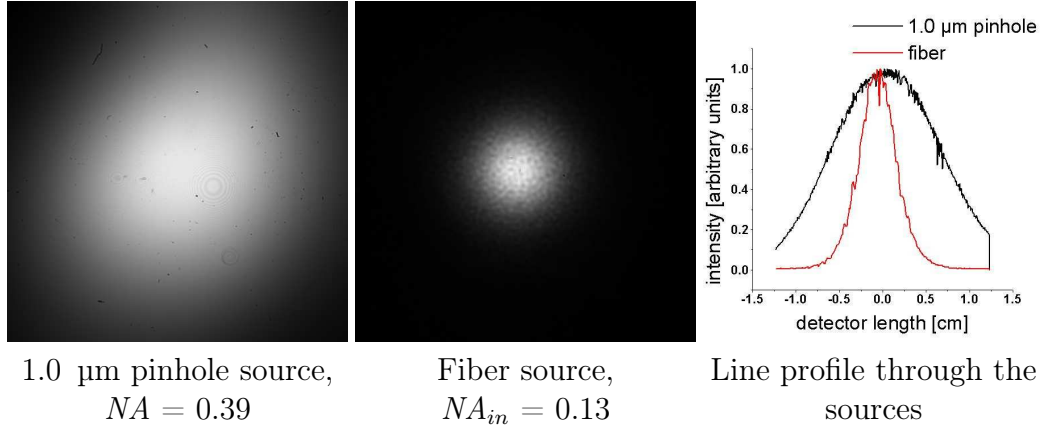
Figure 6.10: Comparison of 1.0 µm pinhole and optical fiber sources at a detector distance of $L = 4.03$ cm

in the right panel confirm that the light coming from the pinhole illuminates the whole detector area, leading to a numerical aperture given by the geometry of $NA = D/(2\sqrt{(L/2)^2 + D^2}) = 0.39$. The numerical aperture achieved by the fiber is not dependent on its distance to the detector as long as the illuminating conic section is smaller than the detector surface. It stays $NA_{in} = 0.13$. Figure 6.12 shows holograms and reconstructions of a fibroblast cell type REF52 wt (Figure 6.11) at approximately the same magnification for both sources. The effect of the decreased numerical aperture in the case of the fiber source is apparent as all fiber source images seem blurred compared to their pinhole counterparts at the same magnification.
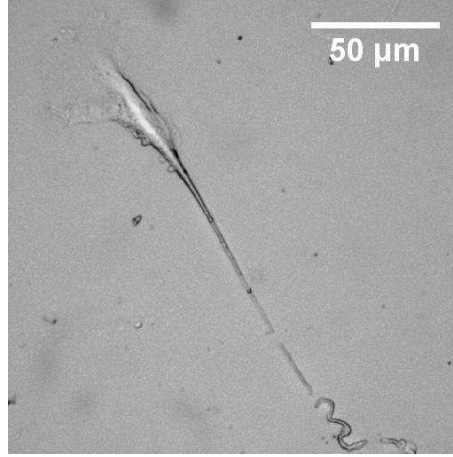
Figure 6.11: Transmission light microscopy image of REF52 wt fibroblast cell, Zeiss A-Plan objective 40x, $NA = 0.5$
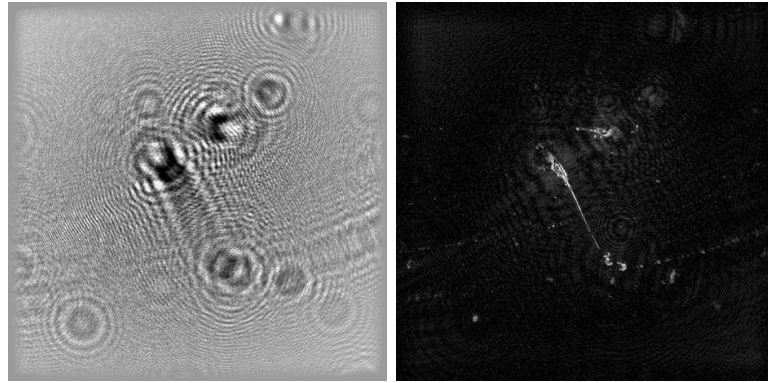
Pinhole source, $\lambda = 543$ nm, $NA = 0.39$, $d_{rec} = 790$ µm
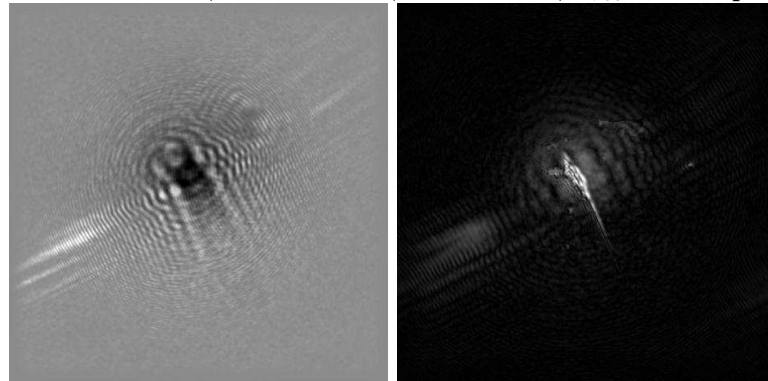
Fiber source, $\lambda = 543$ nm, $NA_{in} = 0.13$, $d_{rec} = 580$ µm

Figure 6.12: Comparison of the imaging properties of a REF52 wt cell recorded with a 1.0 µm pinhole and an optical fiber at a detector distance of $L = 4.03$ cm
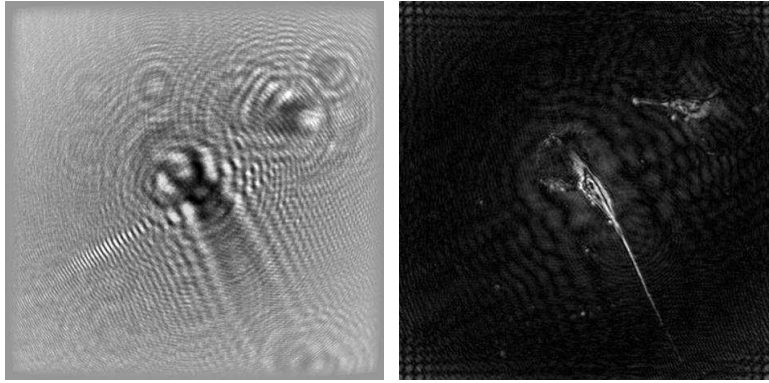
Pinhole source, $\lambda = 543$ nm, $NA = 0.39$, $d_{rec} = 433$ µm
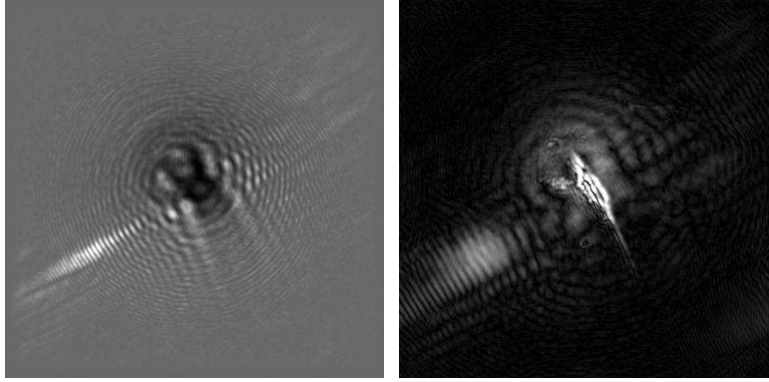
Fiber source, $\lambda = 543$ nm, $NA_{in} = 0.13$, $d_{rec} = 420$ µm
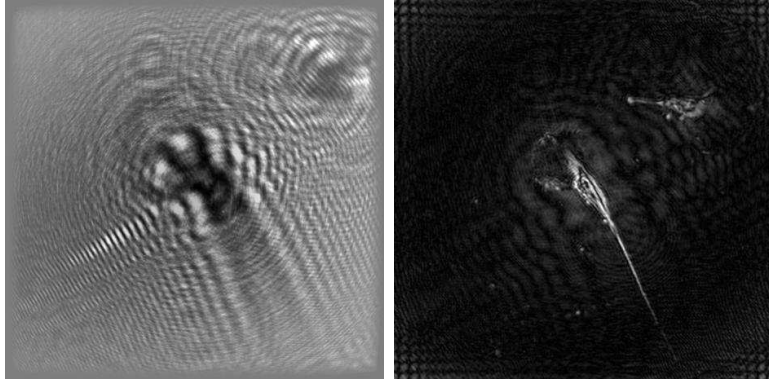
Pinhole source, $\lambda = 543$ nm, $NA = 0.39$, $d_{rec} = 308$ µm
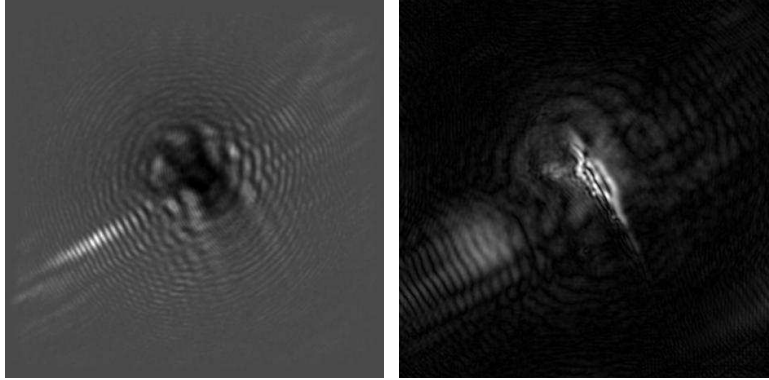
Fiber source, $\lambda = 543$ nm, $NA_{in} = 0.13$, $d_{rec} = 320$ µm

The theoretical resolution for the pinhole is $\delta_{lateral}^{theo} = 696$ nm whereas for the fiber it is $\delta_{lateral}^{theo} = 2088$ nm. The extended filament of the fibroblast cell has a width between 1 and 2 µm and it cannot be resolved by the images recorded with the fiber source. On the contrary, the filament is clearly visible in all the images taken with the pinhole source. The fact that the detector in case of the fiber source was not fully illuminated results in a loss of information towards the borders of the images which is clearly visible as the interference fringes do not reach the edges. Figure 6.13 shows the detector images produced by

| 3 µm pinhole source, $NA_{eff} = 0.25$ | Fiber source, $NA_{in} = 0.13$ | Line profile through the sources |
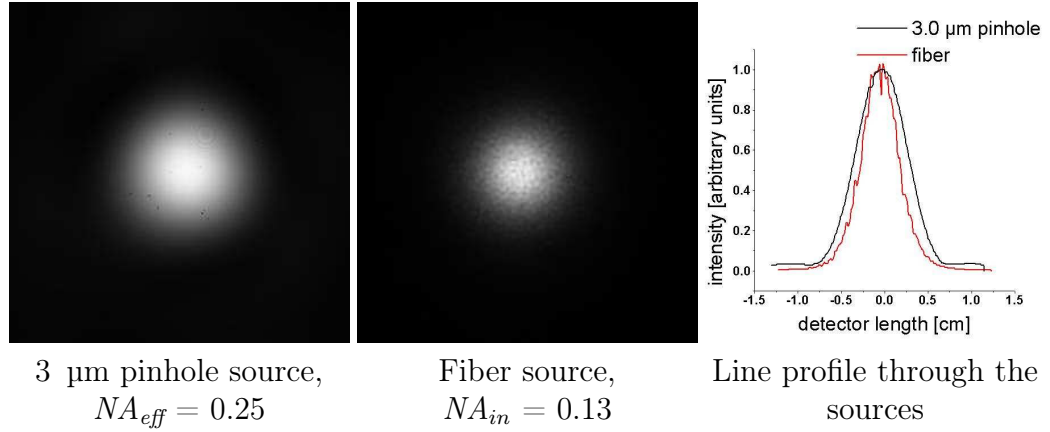
Figure 6.13: Comparison of 3.0 µm pinhole and optical fiber sources at a detector distance of $L = 4.03$ cm

light emerging at a source-detector distance of $L = 4.03$ cm from a 3.0 µm pinhole and a fiber end. The intensity distributions are a lot similar than the ones presented in Figure 6.10. At this distance, the pinhole illuminates approximately 65% of the total detector area, yielding an effective numerical aperture of $NA_{eff} = 0.65$ $NA = 0.25$. Figure 6.14 shows the reconstruction of an image that was recorded with the 3.0 µm pinhole. The magnification adjustment is approximately the same as in the last panel of Figure 6.12. In fact, the images are quite similar, although the resolution in the case of the pinhole source is still better which can be seen by the enhanced detail in the center of the image. Nevertheless, the quality of the reconstructions obtained with an optical fiber source are quite comparable to those obtained by classical pinhole illumination. In fact, the background noise seems to be noticeably lower in the fiber reconstruction. Most probably this is due to the

Hologram, $L = 4.03$ cm,   Reconstruction,
$NA_{eff} = 0.25$ $\delta_{lateral}^{theo} = 1086$ nm,
$d_{rec} = 301$ µm
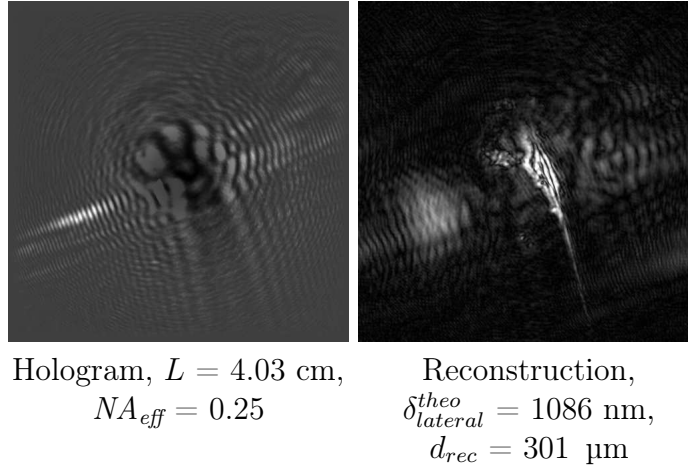
Figure 6.14: REF52 wt cell imaged with a 3.0 µm pinhole source

Gaussian in contrast to the Airy shape of the illumination. The evaluation
of these circumstances might be a task for theoretical work in the future.

6.5   Increasing the Fiber's Numerical Aperture

The drawback of using optical fibers as alternative point sources is their
rather small numerical aperture, thus limiting the achievable lateral resolu-
tion. In SNOM this problem is solved by producing a fiber with a tapered end
through chemical etching with hydrofluoric acid [106] or mechanical draw-
ing [108]. The taper is successively provided with an aperture at its apex
whose diameter is significantly smaller than the illuminating wavelength. The
resolution is then no longer limited by Abbe's refraction law [109]. Both tip
production techniques, etching and drawing, have been applied in our group
and the resulting tips compared in terms of smoothness, light transmission,
opening angle and apex diameter [74]. Mechanically drawn fiber tips proved
to be the most useful for our purposes.   Figure 6.15 shows the recon-
struction of test structures on borosilicate glass. The point source in this
case was an optical fiber whose end was tapered by mechanical drawing. For
comparison, the same sample section recorded under the illumination of a
plain fiber end is shown in Figure 6.16. Both fibers were implemented at a

| Source, | Hologram, | Reconstruction, |
| $\lambda = 543$ nm | $NA_{eff} = 0.17$ | $d_{rec} = 2900$ µm |
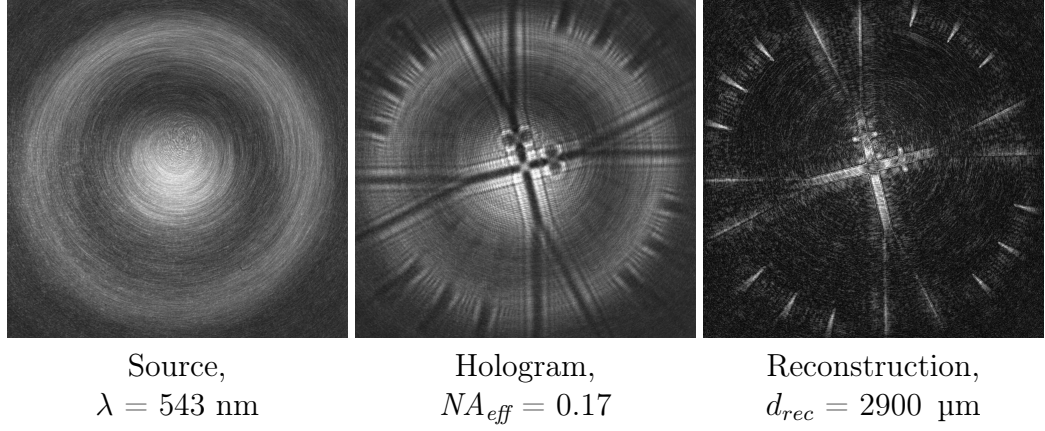
Figure 6.15: Test structures on borosilicate glass imaged with a tapered fiber point source

| Source, | Hologram, | Reconstruction, |
| $\lambda = 543$ nm | $NA_{in} = 0.13$ | $d_{rec} = 5100$ µm |
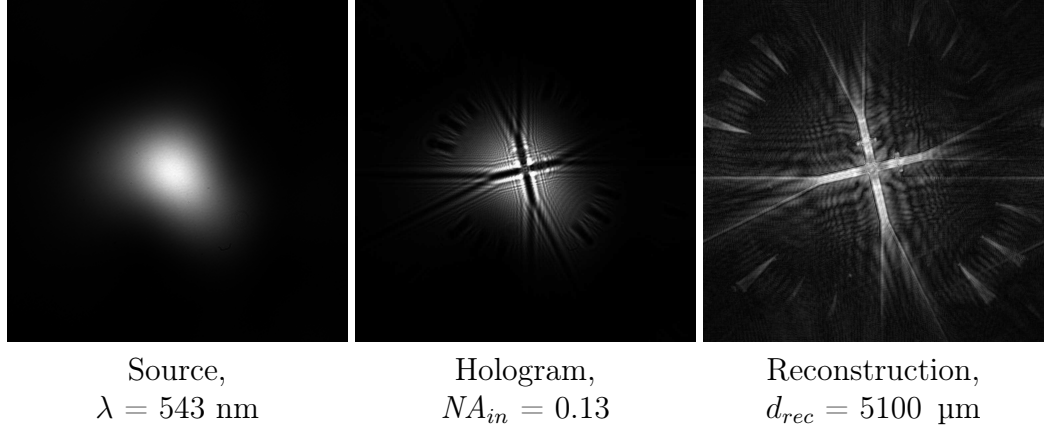
Figure 6.16: Test structures on borosilicate glass imaged with a plain fiber point source

distance of 4.65 cm from the detector. In the case of the plain fiber only a small portion of the detector is illuminated (for full exploitation of the 2.46 cm wide detector the distance would have to be $L = 9.46$ cm), and the numerical aperture of the system thus is still given by the fiber's, in our case $NA_{in} = 0.13$. The source image in Figure 6.15 on the other hand shows a pattern that is dominated by a bright disk in the center surrounded by a ring, similar to the intensity distribution of the linear polarized mode LP_{02} [107]. This is due to the light emitted by the taper which has a different path length than the light coming from the apex. Although the halo is an undesirable

side effect, the center disk is much wider than the illumination provided by the plain fiber in Figure 6.16. An intensity profile through the two sources
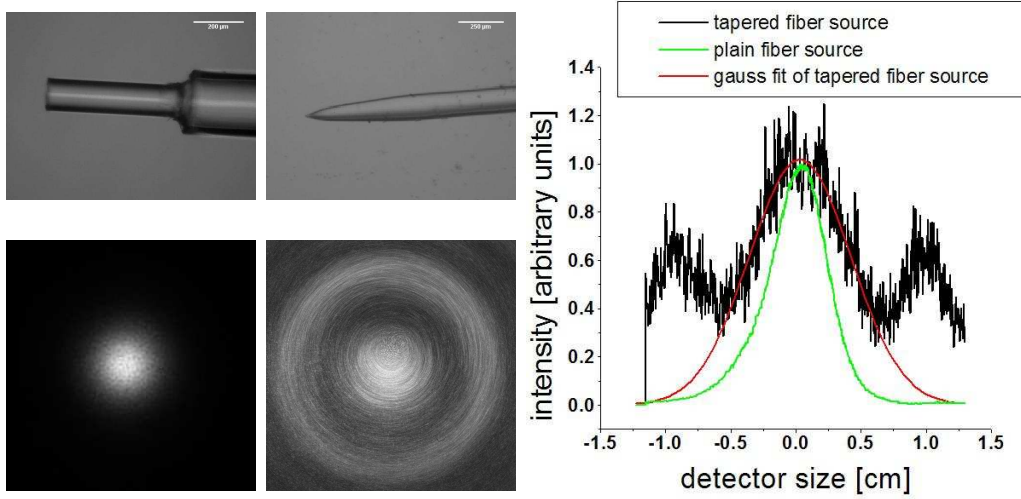
Figure 6.17: Comparison of plain and drawn fiber ends. Microscopy image and hologram from a plain fiber (left) and a tapered fiber (middle) and intensity profiles (right) through the source images provided by the plain fiber (green) and the tapered fiber (black)

displayed in Figure 6.17 confirms the visual impression. The FWHM of the intensity profile of the plain fiber (displayed in green) measures 0.72 cm, whereas the fitted Gaussian (red) of the tapered fiber's intensity profile yields a FWHM of 0.93 cm. This increase of almost 30% leads to an increase in numerical aperture of 30% as well, resulting in $NA_{eff} = 0.17$ for the tapered optical fiber. The theoretical lateral resolution improves accordingly from $\delta_{lateral}^{theo} = 2548$ nm to $\delta_{lateral}^{theo} = 1560$ nm. The reconstruction, however, of the hologram taken with the tapered fiber seems a little blurred compared to the one with the plain fiber. Most probably, light emitted by the taper walls is not coherent any more due to multiple scattering, thus reducing the image quality. This effect, though, could be easily eliminated by coating the taper walls and permitting only the light emitting from the apex to reach the detector as for example described by Manke et al. [110].

6.6   Conclusion and Outlook

Using illumination with a divergent beam for holography enables the recording of a magnified hologram, thus permitting spatial resolution below the detector pixel size. In addition to the commonly employed Airy profile of pinholes one can derive a coherent conical beam which is dominated by the fundamental mode of approximately Gaussian shape [16] from an optical waveguide. Complex and expensive devices to guide the laser beam across the optical table can be avoided and mirror alignment becomes superfluous as the light can be coupled directly into an optical fiber by which it is then guided to the desired destination. The great advantage of employing waveguides as coherent light sources is their almost unlimited flexibility, thus allowing the imaging even in otherwise difficult to access sample regions. Close-up in situ measurements in liquid environments become possible without additional refraction at an interface. Furthermore, there is no risk of clogging the light source in contrast to micrometer-sized pinholes. The method in principle enables high-resolution three-dimensional imaging of comparably large volumes. Spatial resolution of the presented technique is limited by the numerical aperture which is given by the divergence angle of the waveguide beam. Higher resolution requires an increased numerical aperture which could be realized by introducing an aperture at the end of the fiber, e.g. by mechanical drawing of a tapered fiber tip and subsequent metal evaporation to prevent incoherent illumination from exiting through the taper walls.

Chapter 7

Conclusion

The thesis at hand describes the extension, improvement and further development of the method of holographic microscopy in an in-line geometry following a concept developed by D. Gabor. The intrinsic three-dimensionality of holography allows the complete recording (i.e. amplitude and phase) of objects. Employing spherical waves in addition enables the magnified imaging of specimens with achievable resolution practically independent of detector resolution. Approximately spherical wavefronts during this work were mostly created by pinholes with a submicron diameter. Images were recorded with a CCD or CMOS chip with a width of $D = 2.46$ or 1.23 cm, respectively. The highest numerical aperture $NA = D/(2\sqrt{(D/2)^2 + L^2})$ of 0.564 was obtained with a source-detector distance of $L = 9$ mm. The wavelength used was $\lambda = 405$ nm. This yields a theoretical lateral resolution of $\delta_{lateral}^{theo} = \lambda/(2NA) = 359$ nm. Reconstruction of the recorded holograms was done with the help of the program packages LEEPS and DIHM which are based on an algorithm that employs the Kirchhoff-Helmholtz reconstruction formula.

In the first part of the thesis, resolution enhancement was pursued as main goal. Therefore, polystyrene beads with diameters of 2.9, 0.752, 0.500, and 0.356 µm were recorded by DIHM in various conformations including single beads, bead dimers and large clusters. Resolution below half a micrometer in an in-line holographic setup with visible light was thus made possible for

the first time. Beads of 752 nm in size even in the middle of a larger ag-
glomerate of self-assembled beads could also be resolved with this technique
for the first time. By introduction of an oil column with a higher refractive
index into the setup it became possible to increase the numerical aperture
and thus the achievable resolution. An increase of resolution of 28% could
be shown by image comparison of 752 nm polystyrene beads in a cluster
with and without an oil chamber. Additional samples were fibroblast cells
whose manifold structures could be imaged with excellent quality, suggesting
further application of DIHM in biophysics. Furthermore, the feasibility of
DIHM with pulsed nanosecond UV radiation was demonstrated which served
as important pre-experiment for DIHM with picosecond VUV radiation at
the synchrotron facility BESSY II and also for the future implementation
of femtosecond XFEL illumination. There, specially designed lithographic
structures written by electron beam served as resolution test objects. Dur-
ing the first beamtime the general applicability of VUV illumination with
picosecond pulses was proven which represented an important preliminary
experiment for following beamtimes during which submicron resolution with
digital point source holography with pinholes could be shown. Higher numer-
ical apertures through more sophisticated geometries and smaller pinholes as
well as even shorter wavelengths in order to further increase resolution should
now be accessible.

In order to extend the method into the fourth dimension, in the second part
of the thesis, moving particles in flow channels were tracked and their trajec-
tories displayed in 4D plots. Microspheres as well as small oil droplets in an
oil-in-water emulsion served as tracer particles. Through these experiments
it was possible to show the general applicability of DIHM to monitor and
characterize the flow in microchannels in four dimensions. In addition to the
conventional setup with pinholes, optical fibers were employed as waveguides
and their ends used as sources of divergent wavefronts. Test structures on
borosilicate glass, polystyrene beads of a few micrometers in diameter and fi-
broblast cells were imaged with good resolution and image quality. The com-
parison between reconstructions obtained with conventional pinhole point
sources and fiber ends proved the suitability of optical waveguides as truly

alternative sources of coherent divergent illumination with which DIHM can be applied in its accustomed quality. One drawback of the technique so far is its limited resolution due to the fiber's intrinsic numerical aperture which could however be easily improved by introducing an additional aperture at the end of the fiber. The great advantage of the method is its enormous flexibility: The source could for instance be positioned inside a solution, thus resulting in the feasibility of in situ measurements at close reconstruction distances.

By elucidating the feasibility as well as the challenges of the various applications given above, the presented work further substantiates the potential of digital in-line holography as a microscopic method particularly in the fields of biology, soft matter, and life sciences. Numerical apertures and resolutions obtained are now comparable to those of expensive commercial microscopes with the additional advantage of obtaining a fully three-dimensional image of a wide variety of specimens from a single hologram. Further improvement of the technique through more sophisticated geometries, smaller pinholes and shorter wavelengths seems feasible in the near future. Three-dimensional imaging in combination with short wavelength sources with high coherent photon flux such as XFELs currently under construction is a compelling project to be pursued, and the work described here provides a first basis for its further development.

List of Figures

Bibliography

[1] D. GABOR, A New Microscopic Principle, *Nature* **161**, 777 (1948).

[2] P. HARIHARAN, *Basics of Holography*, Cambridge University Press, 2002.

[3] E. HECHT, *Optik*, Oldenbourg Verlag München Wien, 2001.

[4] U. SCHNARS and W. JÜPTNER, *Digital Holography*, Springer Berlin Heidelberg New York, 2005.

[5] K. K.SHARMA, *Optics: Principles and Applications*, Academic Press, 2006.

[6] UNKNOWN AUTHOR, Airy Disc Calculated, URL `http://de.wikipedia.org/wiki/Bild:Diffraction_disc_calculated.png`, Accessed July, 31st 2007.

[7] M. BORN and E. WOLF, *Principles of Optics - Electromagnetic Theory of Propagation, Interference and Diffraction of Light*, Pergamon Press, 6th edition, 1993.

[8] W. XU, M. JERICHO, I. MEINERTZHAGEN, and H. KREUZER, Digital In-Line Holography of Microspheres, *Applied Optics* **41**, 5367 (2002).

[9] MULTIPLE AUTHORS, *Bergmann - Schäfer: Lehrbuch der Experimentalphysik: Optik*, volume 3, Walter de Gruyter, 10th edition, 2004.

[10] J. Garcia-Sucerquia, W. Xu, S. K. Jericho, P. Klages, M. H. Jericho, and J. H. Kreuzer, Digital In-Line Holographic Microscopy, *Applied Optics* **45**, 836 (2006).

[11] H. Kreuzer, Holographic Microscope and Method of Hologram Reconstruction, US Patent 6/411/406 B1, 2002.

[12] E. Leith and J. Upatnieks, Reconstructed Wavefronts and Communication Theory, *Journal of the Optical Society of America* **53**, 1377 (1962).

[13] T. Tanji, Q. Ru, and A. Tonomura, Differential Microscopy by Conventional Electron Off-Axis Holography, *Applied Physics Letters* **69**, 2623 (1996).

[14] B. M. Mertens, M. H. F. Overwijk, and P. Kruit, Off-Axis Holography with a Crystal Beam Splitter, *Ultramicroscopy* **77**, 1 (1999).

[15] J. A. Herrera Ramirez and J. Garcia-Sucerquia, Digital Off-Axis Holography without Zero-Order Diffraction via Phase Manipulation, *Optics Communications* **277**, 259 (2007).

[16] C. Fuhse, C. Ollinger, and T. Salditt, Waveguide-Based Off-Axis Holography with Hard X-Rays, *Physical Review Letters* **97**, 254801/1 (2006).

[17] P. Marquet, E. Cuche, C. Depeursinge, and P. Magistretti, Apparatus and Method for Digital Holographic Imaging, US Patent 6/943/924, 2005.

[18] Lyncée Tec, 3D Real Time Optical Topography, URL `http://www.lynceetec.com`, accessed August, 28th 2007.

[19] A. van der Lugt, Signal Detection by Complex Spatial Filtering, *IEEE Transactions on Information Theory* **IT-10**, 139 (1964).

[20] S. Eisebitt, J. Luening, W. F. Schlotter, M. Loergen, O. Hellwig, W. Eberhardt, and J. Stoehr, Lensless Imaging of

Magnetic Nanostructures by X-Ray Spectro-Holography, *Nature* **432**, 885 (2004).

[21] S. Eisebitt, M. Loergen, W. Eberhardt, J. Luening, and J. Stoehr, Lensless X-Ray Imaging of Magnetic Materials: Basic Considerations, *Applied Physics A* **80**, 921 (2005).

[22] O. Hellwig, S. Eisebitt, W. Eberhardt, W. F. Schlotter, J. Luning, and J. Stohr, Magnetic Imaging with Soft X-Ray Spectroholography, *Journal of Applied Physics* **99**, 08H307/1 (2006).

[23] W. F. Schlotter, R. Rick, K. Chen, A. Scherz, J. Stohr, J. Luning, S. Eisebitt, C. Gunther, W. Eberhardt, O. Hellwig, and I. McNulty, Multiple Reference Fourier Transform Holography with Soft X-Rays, *Applied Physics Letters* **89**, 163112/1 (2006).

[24] D. Litwiller, CCD vs CMOS: Facts and Fiction, Technical report, Photonics Spectra, 2001.

[25] U. Schnars and W. Jüptner, Direct Recording of Holograms by a CCD-Target and Numerical Reconstruction, *Applied Optics* **33**, 179 (1994).

[26] J. Garcia-Sucerquia, W. Xu, M. Jericho, and J. Kreuzer, Immersion Digital In-Line Holographic Microscopy, *Optics Letters* **31**, 1211 (2006).

[27] H. Kreuzer, M. J. Jericho, I. Meinertzhagen, and W. Xu, Digital In-Line Holography with Photons and Electrons, *Journal of Physics: Condensed Matter* **13**, 10729 (2001).

[28] A. Eisele, *Holographische Abbildung von Nanostrukturen durch Projektions-Elektronenmikroskopie*, PhD thesis, Ruprecht-Karls-Universität Heidelberg, 2003.

[29] H. J. Kreuzer, N. Pomerleau, K. Blagrave, and M. H. Jericho, Digital In-Line Holography with Numerical Reconstruction, *Proceedings of SPIE* **3744**, 65 (1999).

[30] W. Xu, M. Jericho, I. Meinertzhagen, and H. Kreuzer, Digital In-Line Holography for Biological Applications, *Proceedings of the National Academy of Sciences (USA)* **98**, 11301 (2001).

[31] J. Garcia-Sucerquia, W. Xu, S. K. Jericho, M. H. Jericho, and H. J. Kreuzer, Digital In-Line Holographic Microscopy Applied to Microfluidic Studies, *Proceedings of SPIE* **6112**, 61120M (2006).

[32] W. Xu, M. Jericho, I. Meinertzhagen, and H. Kreuzer, Tracking Particles in Four Dimensions with In-line Holographic Microscopy, *Optics Letters* **28**, 164 (2003).

[33] H. J. Kreuzer, M. H. Jericho, I. A. Meinertzhagen, and W. Xu, Digital In-Line Holography with Numerical Reconstruction: 4D Tracking of Microstructures and Organisms, *Proceedings of SPIE* **5005**, 299 (2003).

[34] H. Kreuzer, Method for Tracking Particles and Life Forms in Three Dimensions and in Time, US Patent 2004/0169903A1, 2004.

[35] N. I. Lewis, A. D. Cembella, W. Xu, M. H. Jericho, and H. J. Kreuzer, Swimming Speed of Three Species of Alexandrium (Dinophyceae) as Determined by Digital In-line Holography, *Phycologia* **45**, 61 (2006).

[36] S. K. Jericho, J. Garcia-Sucerquia, W. Xu, M. H. Jericho, and H. J. Kreuzer, Submersible Digital In-Line Holographic Microscope, *Review of Scientific Instruments* **77**, 043706/1 (2006).

[37] J. Garcia-Sucerquia, W. Xu, S. K. Jericho, M. H. Jericho, I. Tamblyn, and H. J. Kreuzer, Digital In-Line Holography: 4-D Imaging and Tracking of Microstructures and Organisms in Microfluidics and Biology, *Proceedings of SPIE* **6026**, 602613/1 (2006).

[38] E. Malkiel, O. Alquaddoomi, and J. Katz, Measurements of Plankton Distribution in the Ocean Using Submersible Holography, *Measurement Science and Technology* **10**, 1142 (1999).

[39] E. MALKIEL, J. N. ABRAS, and J. KATZ, Automated Scanning and Measurements of Particle Distributions within a Holographic Reconstructed Volume, *Measurement Science and Technology* **15**, 601 (2004).

[40] J. WATSON, S. ALEXANDER, G. CRAIG, D. HENDRY, P. HOBSON, R. LAMPITT, J. MARTEAU, H. NAREID, M. PLAYER, K. SAW, and K. TIPPING, Simultaneous In-Line and Off-Axis Subsea Holographic Recording of Plankton and Other Marine Particles, *Measurement Science and Technology* **12**, L9 (2001).

[41] R. B. OWEN and A. A. ZOZULYA, In-Line Digital Holographic Sensor for Monitoring and Characterizing Marine Particulates, *Optical Engineering* **39**, 2187 (2000).

[42] K. HINSCH, Holographic Particle Image Velocimetry, *Measurement Science and Technology* **13**, R61 (2002).

[43] H. SUN, H. DONG, M. PLAYER, J. WATSON, D. PATERSON, and R. PERKINS, In-Line Digital Video Holography for the Study of Erosion Processes in Sediments, *Measurement Science and Technology* **13**, L7 (2002).

[44] J. KIRZ, C. JACOBSEN, and M. HOWELLS, Soft X-ray Microscopes and Their Biological Applications, *Quarterly Review of Biophysics* **28**, 33 (1995).

[45] J. E. TREBES, S. B. BROWN, E. M. CAMPBELL, D. L. MATTHEWS, D. G. NILSON, G. F. STONE, and D. A. WHELAN, Demonstration of X-Ray Holography with an X-Ray Laser, *Science* **238**, 517 (1987).

[46] S. LINDAAS, *X-ray Gabor Holography Using a Scanning Force Microscope*, PhD thesis, State University of New York at Stony Brook, 1994.

[47] A. GÖLZHÄUSER, B. VÖLKEL, M. GRUNZE, and H. KREUZER, Optimization of the Low Energy Electron Point Source Microscope: Imaging of Macromolecules, *Micron* **33**, 241 (2002).

[48] L. Cser, G. Török, G. Krexner, I. Sharkov, and B. Faragó, Holographic Imaging of Atoms Using Thermal Neutrons, *Physical Review Letters* **89**, 1755041 (2002).

[49] P. Korecki, J. Korecki, and T. Slezak, Atomic Resolution γ-ray Holography Using the Mössbauer Effect, *Physical Review Letters* **79**, 3518 (1997).

[50] B. Alberts, A. Johnson, J. Lewis, M. Raff, K. Roberts, and P. Walter, *Molecular Biology of the Cell*, Garland Science, 4th edition, 2002.

[51] J. S. W. Denk and W. Webb, Two-Photon Laser Scanning Fluorescence Microscopy, *Science* **248**, 73 (1990).

[52] S. Hell, Double-Scanning Confocal Microscope, European Patent 0491289, 1990.

[53] C. Cremer and T. Cremer, Considerations on a Laser-Scanning-Microscope with High Resolution and Depth of Field, *Microscopica Acta* **81**, 31 (1978).

[54] S. Hell and E. H. Stelzer, Fundamental Improvement of Resolution with a 4Pi-Confocal Fluorescence Microscope Using Two-Photon Excitation, *Optics Communications* **93**, 277 (1992).

[55] T. Cremer and C. Cremer, Chromosome Territories, Nuclear Architecture and Gene Regulation in Mammalian Cells, *Nature Reviews - Genetics* **2**, 292 (2001).

[56] S. W. Hell, Far-Field Optical Nanoscopy, *Science* **316**, 1153 (2007).

[57] N. F. van Hulst, M. F. Garcia-Parajo, M.H.P. Moers, J.-A. Veermann, and A.G.T. Ruiter, Near-Field Fluorescence Imaging of Genetic Material: Toward the Molecular Limit, *Journal of Structural Biology* **119**, 222 (1997).

[58] J. Veerman, A. Otter, L. Kuipers, and N. van Hulst, High Definition Aperture Probes for Near-Field Optical Microscopy Fabricated by Focused Ion Beam Milling, *Applied Physics Letters* **72**, 3115 (1998).

[59] W. Chao, B. D. Harteneck, J. A. Liddle, E. H. Anderson, and D. T. Attwood, Soft X-Ray Microscopy at a Spatial Resolution Better than 15 nm, *Nature* **435**, 1210 (2005).

[60] P. Guttmann, B. Niemann, J. Thieme, D. Hambach, G. Schneider, U. Wiesemann, D. Rudolph, and G. Schmahl, Instrumentation Advances with the New X-ray Microscopes at BESSY II, *Nuclear Instruments and Methods in Physics Research A* **467-468**, 849 (2001).

[61] M. Chaplin, Molecular Vibration and Absorption, URL `http://www.lsbu.ac.uk/water/vibrat.html`, accessed August 3rd, 2007.

[62] Berkeley Lab, X-Ray Attenuation Length, URL `http://www.henke.lbl.gov/optical_constants/atten2.html`, accessed August 3rd, 2007.

[63] C. Martell, P. Olivero, J. Canning, N. Groothoff, B. Gibson, and S. Huntington, Micromachining Structured Optical Fibers Using Focused Ion Beam Milling, *Optics Letters* **32**, 1575 (2007).

[64] F. Lacour, A. Sabac, and M. Spajer, Nanostructuring Optical Waveguides by Focused Ion Beam Milling: Near-Field Characterization, *Journal of the Korean Physical Society* **47**, S175 (2005).

[65] R. Barth, *Digital In-Line X-ray Holographic Microscopy*, PhD thesis, Ruprecht-Karls-Universität Heidelberg, in preparation.

[66] M. Arnold, *Molecularly Defined Nanostructured Interfaces as Tools for the Regulation and Measurement of Functional Length Scales in Cell Adhesion Mediating Protein Clusters*, PhD thesis, Ruprecht-Karls-Universität Heidelberg, 2005.

[67] G. Wedler, *Lehrbuch der Physikalischen Chemie*, VCH Verlagsgesellschaft, 1987.

[68] A. Rosenhahn, R. Barth, X. Cao, M. Schürmann, M. Grunze, and S. Eisebitt, Vacuum-Ultraviolet Gabor-Holography with Synchrotron Radiation, *Ultramicroscopy, in press* (2007), doi: 10.1016/j.ultramic.2007.01.010.

[69] Linos GmbH, Product Catalogue, URL `http://www.linos.com/pages/no_cache/home/shop-optik/planoptik/richttestplatten/?sid=12661\&cHash=c46bbca62d_sid12661`, 2005/2006, accessed August 10th, 2007.

[70] Allresist GmbH, *Negative E-Beam Resists for Mix & Match: Ar-N 7500 (High Resolution) and Ar-N 7520 (Highest Resolution)*.

[71] R. Truckenmüller, P. Henzi, D. Herrmann, V. Saile, and W. Schomburg, Bonding of Polymer Microstructures by UV Irradiation and Welding at Low Temperatures, *Symp. on Design, Test, Integration and Packaging of MEMS/MOEMS, Cannes, France, IEEE* , 265 (2003).

[72] Forschungszentrum Karlsruhe, Key Technologies, Fabrication Technologies, Materials: Injection Molding.

[73] Forschungszentrum Karlsruhe, Key Technologies, Fabrication Technologies, Materials: Hot Embossing.

[74] M. Schürmann, *Abbildung von Objekten im Mikro- und Nanometerbereich durch digitale In-Line Holographie*, Master's thesis, Ruprecht-Karls-Universität Heidelberg, 2004.

[75] J. Garcia-Sucerquia, D. Alvarez-Palacio, M. Jericho, and H. Kreuzer, Comment on "Reconstruction Algorithm for High-Numerical-Aperture Holograms with Diffraction-Limited Resolution", *Optics Letters* **31**, 2845 (2006).

[76] M. Tegze and G. Faigel, Atomic-Resolution X-Ray Holography, *Europhysics Letters* **16**, 41 (1991).

[77] M. Tegze and G. Faigel, X-Ray Holography with Atomic Resolution, *Nature* **380**, 49 (1996).

[78] M. Tegze, G. Faigel, S. Marchesini, M. Belakhovsky, and O. Ulrich, Imaging Light Atoms by X-ray Holography, *Nature* **407**, 38 (2000).

[79] W. Meyer-Ilse, D. Hamamoto, A. Nair, S. A. Lelievre, G. Denbeaux, L. Johnson, A. L. Pearson, D. Yager, M. A. Legros, and C. A. Larabell, High Resolution Protein Localization Using Soft X-Ray Microscopy, *Journal of Microscopy* **201**, 395 (2001).

[80] S. Vogt, G. Schneider, A. Steuernagel, J. Lucchesi, E. Schulze, D. Rudolph, and G. Schmahl, X-Ray Microscopic Studies of the Drosophila Dosage Compensation Complex, *Journal of Structural Biology* **132**, 123 (2000).

[81] BESSY GmbH, ABOUT BESSY - an Ultimate Space and Time Microscope, URL `http://www.bessy.de`, accessed August, 8th 2007.

[82] Center for X-ray Optics and Advanced Light Source, Lawrence Berkeley National Laboratory, X-ray Data Booklet.

[83] P. A. Thompson and S. M. Troian, A General Boundary Condition for Liquid Flow at Solid Surfaces, *Nature* **389**, 360 (1997).

[84] L. E. Locascio, Microfluidic Mixing, *Analytical and Bioanalytical Chemistry* **379**, 325 (2004).

[85] A. D. Stroock, S. K. W. Dertinger, A. Ajdari, I. Mezic, H. A. Stone, and G. M. Whitesides, Chaotic Mixer for Microchannels, *Science* **295**, 647 (2002).

[86] T. J. Johnson, D. Ross, and L. E. Locascio, Rapid Microfluidic Mixing, *Analytical Chemistry* **74**, 45 (2002).

[87] M. H. ODDY, J. G. SANTIAGO, and J. C. MIKKELSEN, Electrokinetic Instability Micromixing, *Analytical Chemistry* **73**, 5822 (2001).

[88] A. RIDA and M. A. M. GIJS, Manipulation of Self-Assembled Structures of Magnetic Beads for Microfluidic Mixing and Assaying, *Analytical Chemistry* **76**, 6239 (2004).

[89] B. STOEBER, D. LIEPMANN, and S. J. MULLER, Strategy for Active Mixing in Microdevices, *Physical Review E* **75**, 066314/1 (2007).

[90] P. GARSTECKI, M. A. FISCHBACH, and G. M. WHITESIDES, Design for Mixing Using Bubbles in Branched Microfluidic Channels, *Applied Physics Letters* **86**, 244108/1 (2005).

[91] G. G. YARALIOGLU, I. O. WYGANT, T. C. MARENTIS, and B. T. KHURI-YAKUB, Ultrasonic Mixing in Microfluidic Channels Using Integrated Transducers, *Analytical Chemistry* **76**, 3694 (2004).

[92] D. ROSS, T. J. JOHNSON, and L. E. LOCASCIO, Imaging of Electroosmotic Flow in Plastic Microchannels, *Analytical Chemistry* **73**, 2509 (2001).

[93] T. G. MASON, K. GANESAN, J. H. VAN ZANTEN, D. WIRTZ, and S. C. KUO, Particle Tracking Microrheology of Complex Fluids, *Physical Review Letters* **79**, 3282 (1997).

[94] J. SATO and V. BREEDVELD, Transient Rheology of Solvent-Responsive Complex Fluids by Integrating Microrheology and Microfluidics, *Journal of Rheology* **50**, 1 (2006).

[95] M. S. HALE and J. G. MITCHELL, Motion of Submicrometer Particles Dominated by Brownian Motian near Cell and Microfabricated Surfaces, *Nano Letters* **1**, 617 (2001).

[96] J. WU and L. L. DAI, Apparent Microrheology of Oil-Water Interfaces by Single-Particle Tracking, *Langmuir* **23**, 4324 (2007).

[97] S. DEVASENATHIPATHY and J. G. SANTIAGO, Particle Tracking Techniques for Electrokinetic Microchannel Flows, *Analytical Chemistry* **74**, 3704 (2002).

[98] R. J. E. WALPOT, C. W. M. VAN DER GELD, and J. G. M. KUERTEN, Determination of the Coefficients of Langevin Models for Inhomogeneous Turbulent Flows by Three-Dimensional Particle Tracking Velocimetry and Direct Numerical Simulation, *Physics of Fluids* **19**, 045102/1 (2007).

[99] J. G. SANTIAGO, S. T. WERELEY, C. D. MEINHART, D. J. BEEBE, and R. J. ADRIAN, A Particle Image Velocimetry System for Microfluidics, *Experiments in Fluids* **25**, 316 (1998).

[100] D. LIU, S. V. GARIMELLA, and S. T. WERELEY, Infrared Micro-Particle Image Velocimetry in Silicon-Based Microdevices, *Experiments in Fluids* **38**, 385 (2005).

[101] C. BEST, K. GRIEPENKERL, C. HOFMANN, C. HARTNACK, and A. ANDREEFF, *Taschenbuch der Physik*, Verlag Harri Deutsch, 1998.

[102] D. R. LIDE, editor, *Handbook of Chemistry and Physics*, CRC Press, 87th edition, 2006.

[103] A. ULMAN, Formation and Structure of Self-Assembled Monolayers, *Chemical Review* **96**, 1533 (1996).

[104] S. TOKUMITSU, A. LIEBICH, S. HERRWERTH, W. ECK, M. HIMMELHAUS, and M. GRUNZE, Grafting of Alkanethiol-Terminated Poly(ethylene glycol) on Gold,
Langmuir **18**, 8862 (2002).

[105] G. M. WHITESIDES and P. E. LAIBINIS, Wet Chemical Approaches to the Characterization of Organic Surfaces: Self-Assembled Monolayers, Wetting, and the Physical-Organic Chemistry of the Solid-Liquid Interface, *Langmuir* **6**, 87 (1990).

[106] A. LAZAREV, N. FANG, Q. LUO, and X. ZHANG, Formation of Fine Near-Field Scanning Optical Microscopy Tips. Part II. By Laser-heated Pulling and Bending, *Review of Scientific Instruments* **74**, 3684 (2003).

[107] F. MITSCHKE, *Glasfasern*, Elsevier GmbH, München, 1st edition, 2005.

[108] P. HOFFMANN, B. DUTOIT, and R.-P. SALATHÉ, Comparison of Mechanically Drawn and Protection Layer Chemically Etched Optical Fiber Tips, *Ultramicroscopy* **61**, 165 (1995).

[109] E. SYNGE, A Suggested Method for Extending Microscopic Resolution into the Ultra-Microscopic Region, *Philosophical Magazine* , 356 (1928).

[110] I. MANKE, J. LORBACHER, J. SPITHOVEN, F. HEINRICHSDORFF, and M. DÄHNE-PRIETSCH, SNOM-Induced Photoluminescence of Individual InGaAs Quantum Dots Using Etched Metal-coated Fiber Tips, *Surface and Interface Analysis* **27**, 491 (1999).

Acknowledgement

work with them. I also thank Steffen Albrecht for his efforts at the FIB.

Alexander Küller was always there to help me with the SEM. Thanks for that! Furthermore, I thank Sebastian Weiße and especially Matthias Heydt for Matlab Programming. I also thank Dominique Verreault for being such a tidiness freak and always finding whatever device I needed for my current setup and especially for patiently proof-reading this thesis recurringly.

A listing of the numerous things Ruth Barth did for me during the last three years would most probably go beyond the scopes of this acknowledgement by far, so I follow in her footsteps once again by saying simply thank you and hope she knows how much her help meant to me.

Büro 1 in present and past occupancy i.e. Eli, Ruth, Säbb, Svetlana and Toffi, including next-door and next-building neighbors Andrea, Brian, Dominique, Matthias and Sören helped me survive and drained my sanity which does not necessarily pose a contradiction. Thanks for being such great colleagues!

For technical support I very much thank Peter Jeschka, Günter Meinusch and Reinhold Jehle, and for administrative help my acknowledgement goes to Robert Läufer, Edeltraud Boczek and Benjamin Scherke.

Thanks to all the rest of the Grunze-group for any other support in biological, chemical, physical and technical questions!

Nicht zuletzt möchte ich meinem Onkel Eckart, meinen Großmüttern Omi Gabi und Oma Irmgard und ganz besonders meiner Mami für die moralische und finanzielle Unterstützung während der gesamten Promotion danken.